INSTYTUT FIZYKI JĄDROWEJ
im. HENRYKA NIEWODNICZAŃSKIEGO
POLSKIEJ AKADEMII NAUK

Doctoral thesis

Marta Babicz

Simulation studies and tests of the light detection and trigger systems of the ICARUS detector in the Short Baseline Neutrino program at Fermilab

Supervisors:
prof. dr hab. Agnieszka Zalewska
dr Francesco Pietropaolo

Kraków, 2021

Abstract

The Short Baseline Neutrino (SBN) program at the Fermi National Laboratory (Fermilab or FNAL) in the US inscribes in an extensive experimental programme of searches for sterile neutrino(s), whose existence is one of the fundamental open questions of neutrino physics. The main objectives of the SBN program are searches for the LSND-like sterile neutrino oscillations using accelerator neutrino beams with full coverage of relevant values of the $\Delta \mathrm{m}^2 \sim \mathrm{eV}^2$ oscillation parameter, inconsistent with oscillations of only the three active neutrino of the Standard Model, and making precision measurements of neutrino interactions with Argon.

The measurements of the beam before oscillations will be done in the SBND detector at a distance of 110 m from the neutrino source while the measurements of the ν_{e} ($\bar{\nu_{\mathrm{e}}}$) appearance and ν_μ ($\bar{\nu_\mu}$) disappearance will be studied in the MicroBooNE and ICARUS detectors at distances of 470 m and 600 m, respectively. All the three detectors are liquid Argon Time Projection Chambers (LAr TPCs). The studies of neutrino interactions with the MicroBooNE detector have started in 2015. The first physics data taking with the ICARUS detector was in June 2021, while for SBND it is planned for the year 2023.

The SBN detectors, working near the Earth surface, are exposed to a substantial cosmic background, which can mimic the genuine neutrino interactions. Thus, it is fundamental to distinguish the signals related to the neutrino beams from those induced by the cosmic rays.

The subject of this thesis is related to the ICARUS detector with a focus on its light detection and trigger systems. Before the detector was transported to Fermilab in April 2017, the light detection system was significantly upgraded at CERN. The detector was equipped with 360 8" R5912 Hamamatsu Photomultiplier Tubes (PMTs). The proposed trigger system, based on the coincidence of the prompt scintillation light signals, measured by PMTs, with the arrival time of beam neutrinos in the detector, is based on the light detection system.

This thesis presents the tests and evaluation of the PMTs performance and the development of the trigger system, which were carried out at CERN. The PMT tests proved that the ICARUS light detection system fulfils the requirements of the SBN program, and the detector will manage to operate at the Earth surface. The first tests of the trigger elements showed the proper performance of the trigger electronics and helped to develop and check the initial trigger logic based on cosmic muons registered in the liquid Argon test facility and on simulated events. Some simulation results are presented in this thesis. Moreover, the group velocity of scintillation photons in liquid Argon has been measured for the first time.

The light detection system calibration and further development of the trigger logic, aiming at increasing their efficiencies for physics data taking, had been performed for the final detector configuration during the detector commissioning at Fermilab. The trigger system logic is still under test and tuning.

This thesis also presents a way of using the PMT information for filtering neutrino interactions and cosmic muons by applying a Convolutional Neural Network (CNN) to the simulated data. The results show that with this method, the cosmic background can be reduced by up to 76% with a neutrino selection efficiency of 99%. However, this work aims at filtering the real data cases, which are usually not identical to the simulated ones. Thus, a way to mitigate biases from imperfect simulations by applying Domain Adversarial Neural Networks (DANNs) is also presented. The results demonstrate that adversarial training through a DANN can alleviate the loss of efficiency at a relatively low cost of reduced background rejection. This is the first application of DANN for CNN as an event classifier for a LAr TPC. The results of applying DANN to the real data collected with the ICARUS detector in June 2021 are presented for the first time.

Streszczenie

Program neutrinowy z krótką bazą pomiarową (Short Baseline Neutrino - SBN) w Narodowym Laboratorium Przyspieszania Cząstek Elementarnych im. E. Fermiego (FNAL lub Fermilab) w USA wpisuje się w szeroki zakres eksperymentalnych poszukiwań neutrin sterylnych, których istnienie jest jednym z fundamentalnych otwartych pytań fizyki neutrin. Głównym celem programu SBN jest poszukiwanie, przy użyciu wiązek neutrin akceleratorowych, tzw. efektu LSND, czyli oscylacji neutrin dla różnicy kwadratu mas neutrin $\Delta\mathrm{m}^2$ rzędu 1 eV^2, niezgodnej z oscylacjami tylko trzech aktywnych neutrin z Modelu Standardowego. Celem SBN jest też wykonanie precyzyjnych pomiarów oddziaływań neutrin z Argonem.

Pomiary wiązki przed oscylacjami będą wykonywane w detektorze SBND w odległości 110 m od źródła neutrin, natomiast pomiary pojawiania się ν_{e} ($\bar{\nu_{\mathrm{e}}}$) oraz zanikania ν_μ ($\bar{\nu_\mu}$) będą badane w detektorach MicroBooNE i ICARUS w odległościach odpowiednio 470 m i 600 m. Wszystkie trzy detektory to ciekło-Argonowe komory projekcji czasowej (LAr TPC). Badania oddziaływań neutrin za pomocą detektora MicroBooNE rozpoczęły się w 2015 roku. Pierwsze zbieranie danych na potrzeby badań z fizyki za pomocą detektora ICARUS nastąpiło w czerwcu 2021 roku, a dla detektora SBND przewidywane jest w 2023 roku.

Detektory SBN, pracujące blisko powierzchni Ziemi, są narażone na znaczne tło kosmiczne, które może naśladować prawdziwe oddziaływania neutrin. Fundamentalne znaczenie ma więc odróżnienie sygnałów związanych z oddziaływaniami neutrin od tych indukowanych przez promienie kosmiczne.

Temat tej rozprawy doktorskiej jest związany z detektorem ICARUS, ze szczególnym uwzględnieniem jego systemów detekcji światła i wyzwalania. Zanim detektor został przetransportowany do laboratorium Fermilab w kwietniu 2017 roku, system detekcji światła został znacząco zmodernizowany w laboratorium CERN. Detektor został wyposażony w 360 8" fotopowielaczy typu R5912 wyprodukowanych przez Hamamatsu. Na systemie detekcji światła oparto proponowany system wyzwalania, bazujący na zbieżności szybkich sygnałów światła scyntylacji, mierzonych przez fotopowielacze, z czasem przybycia neutrin wiązki do detektora.

Niniejsza rozprawa przedstawia testy i ocenę działania fotopowielaczy oraz prace dla systemu wyzwalania, które zostały przeprowadzone w laboratorium CERN. Testy fotopowielaczy dowiodły, że system detekcji światła detektora ICARUS spełnia wyma-

gania programu SBN, a sam detektor zdoła pracować na powierzchni Ziemi. Pierwsze testy elementów systemu wyzwalania wykazały prawidłowe działanie elektroniki wyzwalającej. Pozwoliły też na opracowanie i sprawdzenie wstępnej logiki systemu wyzwalania na podstawie pomiarów mionów kosmicznych zarejestrowanych przez stanowisko testowe wyposażone w ciekły Argon oraz na podstawie przeprowadzonych symulacji. Niektóre wyniki tych symulacji zostały przedstawione w niniejszej pracy. Ponadto, po raz pierwszy zmierzono prędkość grupową fotonów scyntylacyjnych w ciekłym Argonie.

Kalibracja systemu detekcji światła oraz dalszy rozwój logiki systemu wyzwalania, mający na celu zwiększenie ich efektywności w pozyskiwaniu danych fizycznych, zostały przeprowadzone dla ostatecznej konfiguracji detektora podczas jego uruchomienia w Fermilabie. Logika systemu wyzwalania jest nadal testowana i dostrajana.

W niniejszej pracy przedstawiono również sposób wykorzystania informacji z fotopowielaczy do filtrowania oddziaływań neutrin i mionów kosmicznych poprzez zastosowanie sieci neuronowej (Convolutional Neural Network - CNN) do symulowanych danych. Wyniki pokazują, że dzięki tej metodzie tło kosmiczne może być zredukowane nawet o 76% przy efektywności selekcji neutrin na poziomie 99%. Ponieważ praca ta ma na celu filtrowanie rzeczywistych danych, które nie są identyczne z symulowanymi, przedstawiono również sposób łagodzenia błędów wynikających z niedoskonałych symulacji poprzez zastosowanie domenowych sieci neuronowych (Domain Adversarial Neural Network - DANN). Wyniki pokazują, że trening przeciwstawny poprzez DANN może złagodzić utratę wydajności przy stosunkowo niskim koszcie zmniejszonego odrzucania tła. Jest to pierwsze zastosowanie DANN dla CNN jako klasyfikatora zdarzeń dla LAr TPC. Po raz pierwszy prezentowane są też wyniki zastosowania DANN do danych rzeczywistych zebranych za pomocą detektora ICARUS w czerwcu 2021 roku.

Contents

Introduction

The last twenty-five years brought several breakthroughs in neutrino physics, like the discovery of neutrino oscillations and the beginning of neutrino astronomy. Nowadays, neutrino physics represents one of the most active fields of research in the domain of particle physics. However, some fundamental questions about neutrinos are still open, one of which is related to the existence or non-existence of sterile neutrino(s).

The discovery of sterile neutrinos would point to physics beyond the Standard Model and open up a rich field of experimental and theoretical studies of their properties and their role in particle physics, astrophysics and cosmology. Many experiments are dedicated to answering this question, but the leading one is the Short Baseline Neutrino program at Fermilab (Fermi National Accelerator Laboratory) in the US.

The SBN program, primarily using the neutrino beam produced with protons from the Fermilab's Booster, will use three detectors, called SBND, MicroBooNE and ICARUS, placed at 110 m, 470 m and 600 m from the neutrino source. All of them are Liquid Argon Time Projection Chambers (LAr TPCs). The aim is to look for oscillations beyond the standard 3-flavour neutrino mixing.

The liquid Argon detection technique, pioneered by the ICARUS (Imaging Cosmic And Rare Underground Signals) experiment whilst the detector was in Gran Sasso (before being moved to Fermilab), is rapidly gaining ground in neutrino interactions and oscillations studies. It offers precise spatial and energy measurements based on the electron signal from the Argon ionisation and accurate time measurements based on the scintillation signal from the Argon de-excitation.

The main subject of this PhD thesis is related to the ICARUS detector and its operation within the SBN neutrino oscillation program. The ICARUS detector is the largest LAr TPC detector yet used in neutrino research. This detector performed well in the neutrino experiment on the CNGS (CERN Neutrinos to Gran Sasso) beam at the Gran Sasso underground laboratory, where, among other things, it was used to measure the neutrino velocity. In the SBN program, ICARUS as a far detector aims to search for oscillations involving sterile neutrinos.

At Fermilab, the detector operates almost at the Earth surface under very challenging experimental conditions because of being exposed to the substantial cosmic-ray background, which can mimic genuine neutrino interactions. Therefore, it is fundamental to distinguish the signals related to the neutrino beams from those induced by cosmic rays. For this reason, a trigger system based on the prompt signals from the LAr scintillation light, as detected by the system of photomultiplier tubes (PMTs), coincident with the neutrino beam gate is essential.

The main goal of the trigger system is to save all neutrino interactions while minimising the background events that occur in the detector. The trigger system efficiently detects the beam neutrino events and eliminates the cosmic background outside the beam window. However, it also accepts some background events that enter the detector during the beam gate duration. These events can mimic neutrino interactions and consequently be analysed and reconstructed, consuming time and resources only to turn out to be the background. Traditional cut-based selections can deal with this issue, but they require full information about both the scintillation light and electron ionisation signals and consequently computationally expensive reconstruction algorithms.

A powerful solution to this problem is applying machine learning techniques using only the readily available information from PMTs of the ICARUS light detection system. The PMT signal contains relatively coarse but also easily accessible information based on which the machine learning algorithm can distinguish cosmic rays from neutrino interactions before running any reconstruction algorithms. Thus, it is a further factor in the cosmic background rejection. Additional effort has been made to ensure that the neutrino selection efficiency is readily adaptable from simulation to real data.

The contents of this PhD thesis are organised into ten chapters. Chapter 1 briefly presents a theoretical description and main experimental results related to neutrino oscillations and interactions. In Chapter 2 experimental indications and phenomenology of sterile neutrinos are discussed. Chapter 3 provides an overview of the LAr TPC detection technique illustrated by the ICARUS detector operation at the Gran Sasso laboratory. In Chapter 4 the SBN program at Fermilab is described, starting with the SBN physics goals, followed by the neutrino beams production and operation at the Fermilab accelerator complex and design and operation of the three detectors. Chapter 5 gives an overview of the preparatory work and commissioning of the ICARUS detector for the SBN program. Chapter 6 is dedicated to the ICARUS light detection system overview with the description of the PMT test campaign at CERN and its results. In Chapter 7, dedicated to the ICARUS trigger system, the expected event rates, the trigger system architecture, and its possible improvements are described. The realisation of the trigger system required extensive tests. To facilitate these tests, the small-scale test facility with the full trigger chain and the Data Acquisition (DAQ) system has been built at CERN. The test facility and tests performed with the facility are the subjects of Chapter 8. Chapter 9 describes the simulation and analysis tools used to study the trigger efficiency and the concrete overburden impact on the event rates. Finally, Chapter 10 presents the event filtering method based on the PMT information using machine learning algorithms. A short summary and an outlook are given at the end. A list of abbreviations has been added to facilitate reading.

The material presented in this thesis is original, except where specific reference is made to the work of others. Given the nature of today's particle physics experiments, most work is collaborative or relies on work performed previously. This has been indicated where appropriate, with all tables and figures produced by others being labelled with a reference.

My first task has been related to the ICARUS light detection system. The work started with my diploma thesis and was continued later. I actively participated in the tests and installation of the newly selected PMTs. My main contribution was the evaluation of the PMT response to a single photoelectron for all the PMTs at room temperature and for 60 of them at LAr temperature. I also evaluated the PMT noise and calculated the PMT gains for several power supply values and thus was able to equalise the gain of the PMTs by adjusting their supply voltages. The results of this work were published in Ref. [1] and Ref. [2]. I also contributed to the PMT timing properties evaluation by performing tests and helping with the analysis of the PMT signals. The results of this work were published in Ref. [3]. Moreover, I participated in the PMT linearity and saturation tests at CERN, with results published in Ref. [4].

I also worked on the ICARUS trigger system preparation. The basic trigger working principles are described in the internal trigger working group technical notes [5, 6] that I co-authored. The proposed trigger design was also presented by me at the 14th Pisa Meeting on Advanced Detectors [7]. I was responsible for the work performed for the trigger system at the LAr test facility at CERN. I contributed to the assembly and installation of the electronic components, leading the test campaigns and the analysis. The tests and their results were also presented by me at the 15th Vienna Conference on Instrumentation in 2019 [8].

I was also working on the application of the LAr test facility for the LAr scintillation light properties evaluation using the ^{241}Am alpha source. I participated in the data taking, system monitoring and data analysis. This work was published in Ref. [9]. I also contributed to the installation and test of the modified test facility for the LAr scintillation photons propagation in LAr. My tasks were related to data taking, system monitoring and analysis of the PMT signals. I performed fits to the fast and slow components of the PMT response to the scintillation photons to evaluate the LAr purity based on the slow component value. The results of this work are published in Ref. [10].

Due to the COVID-19 pandemic, access to Fermilab was limited, and official travels were suspended. Thus, my work on the trigger tests and commissioning at Fermilab was not possible. Therefore, I started working on another project related to cosmic background removal using machine learning. This work was my own initiative, and it appeared to be a very successful method in reducing cosmic background events. The first results of this work were presented at the 37th International Cosmic Ray Conference [11]. This method was further improved to be robust to simulation bias and allow arbitrary use to filter the real data. The paper dedicated to this methodology is under preparation, with the expected due date by the end of this year.

Chapter 1

Neutrino physics

The theoretical hypothesis positing the neutrino existence was formulated by W. Pauli in 1930 as an explanation of the observed continuous energy spectra in β-decays [12]. In the process of β-decay, a nucleus of atomic number Z transformed to one with a smaller mass and atomic number Z + 1, and an emitted electron was observed:

$$ {}^{\mathrm{A}}_{\mathrm{Z}}\mathrm{X} \rightarrow^{\mathrm{A}}_{\mathrm{Z+1}} \mathrm{X}^{'} + \mathrm{e}^{-}. \tag{1.1}$$

In such a two-body decay, the electron would carry off the difference of masses of nuclei in the form of kinetic energy at a well-defined constant value. However, observations showed that in various β-decays, there were continuous distributions of electron energy as it is shown in Figure 1.1.

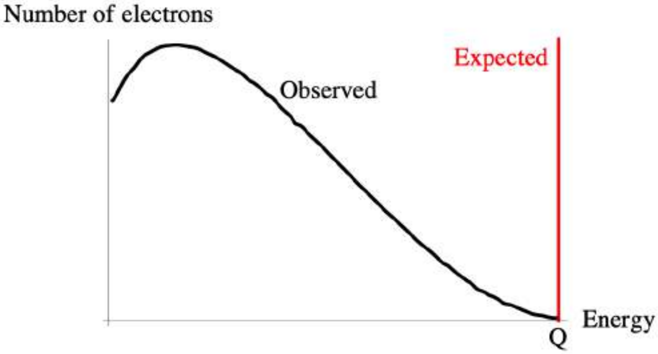

Figure 1.1: The observed continuous energy spectrum of electrons released in β-decay (black line) and expected energy spectrum (red line) according to the contemporary understanding of β-decay as a two-body problem, which could only be explained by violating the law of conservation of energy. Figure from [13].

In addition, both the parent nucleus and the daughter nucleus had either integer or half-integer spins which was not consistent with the emission of only an electron, which has spin $\frac{1}{2}$. That would mean that the law of conservation of energy and angular momentum did not hold at the atomic level.

Pauli hypothesis of the existence of a very light neutral particle of spin $\frac{1}{2}$ very weakly interacting with matter and emitted alongside the electron in β-decay explained the continuous spectrum and helped with solving both non-conservation problems. The name of *neutrino* was given to this new hypothetical particle by E. Fermi, who developed the theory of β-decay [14].

It had taken 25 years until the experimental confirmation of the existence of the neutrino was announced. In 1956 Reines and Cowan observed the interactions of electron antineutrinos in the so-called inverse β-decay $\bar{\nu}_{\mathrm{e}} + \mathrm{p} \rightarrow \mathrm{n} + \mathrm{e}^{+}$ [15]. The experiment was performed near the Savannah River nuclear reactor, using the detector consisting of two water tanks with dissolved $\mathrm{CdCl_2}$ and sandwiched between three tanks of liquid scintillator readout by photomultipliers. The setup was optimised to register the signal of $\bar{\nu}_{\mathrm{e}}$ interactions corresponding to the coincidence of the fast gamma rays from the e^{+} annihilation and the slower light signal due to neutron capture on Cadmium.

The Reines and Cowan experiment started a long history of neutrino experiments, very demanding due to very low cross-sections of neutrino interactions, but also rich in very interesting results, as will be shown in this thesis.

Neutrinos are now known to be the second most abundant particles in the Universe after photons. The estimate is that each cubic centimetre of the Universe contains more than 300 relic neutrinos created shortly after the Big Bang. There are several other natural neutrino sources, including the interactions of cosmic rays with atomic nuclei in the Earth's atmosphere (atmospheric neutrinos and antineutrinos), the nuclear reactions in the cores of stars, and Supernova explosions. The bulk of neutrinos in the vicinity of the Earth are from nuclear reactions in the Sun's core (solar neutrinos). About 65 billion solar neutrinos per second pass through every square centimetre perpendicular to the direction of the Sun [16]. Neutrinos can also be created artificially with nuclear reactors (reactor antineutrinos) and particle accelerators (accelerator neutrinos and antineutrinos). One notable advantage of artificially produced neutrinos is that the systematic effects are much better controlled than those of neutrinos from natural sources. Therefore, most current and future oscillation experiments are based on neutrinos from accelerators and reactors.

1.1 Neutrinos in the Standard Model

The Standard Model (SM) of particle physics [17] describes neutrinos as neutral leptons. The SM is the prevailing theory of particle physics where the most elementary particles and three fundamental interactions: electromagnetic, weak, and strong, are defined.

The elementary particles are divided into generations or families, between which particles differ by their flavour quantum number and mass, but their interactions are identical. The existence of three generations of elementary particles of matter with half-integer spin, called *fermions*, was proved by the experiments at the Large Electron-Positron (LEP) collider at CERN through the measurement of the number of light active neutrino species $N_\nu = 2.9840 \pm 0.0082$ [18]. However, there is yet no theoretical explanation why there appear to be three generations of particles.

Each generation contains one pair of quarks (with electrical charges $+\frac{2}{3}$ and $-\frac{1}{3}$) and one pair of leptons (charged and neutral), which totals to six quarks and six leptons. Moreover, each of these particles has a corresponding antiparticle. In Figure 1.2, the first three columns show the Standard Model of elementary particles of matter with their principal properties.

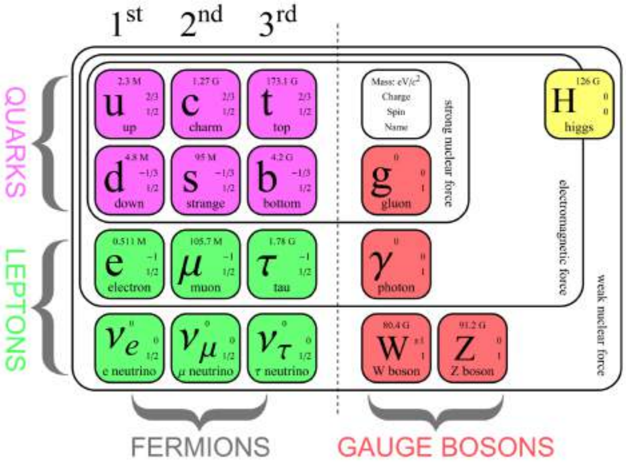

Figure 1.2: An illustration of the elementary particles within the Standard Model, with the three generations of matter particles in the first three columns, gauge bosons in the fourth and fifth, and the Higgs boson in the last column. Figure from [19].

All the particles described by the SM interact with the force mediating particles, which, unlike fermions, have integer spin. According to the Standard Model, these gauge bosons, namely eight gluons, the photon, Z^0 and $W^{\pm}$, are force carriers that mediate the strong, electromagnetic and weak fundamental interactions, respectively. In Figure 1.2, the gauge bosons with spin 1 are listed in the fourth and fifth columns. There is also a Higgs boson with spin 0, discovered at CERN in 2012 [20, 21]. In the SM, it provides a mechanism for most fundamental particles to acquire mass.

In the SM, neutrinos exist in three flavours (ν_e, ν_μ, ν_τ). They have no electric charge, are massless and left-handed. Their corresponding antiparticles are right-handed. The *handedness* or helicity represents the sign of the projection of a particle's spin at its direction of motion. It is positive (right-handed) if the direction of its spin is the same as its motion and negative (left-handed) if the directions of spin and motion are contrary. Unlike neutrinos, other fermions have both left-handed and right-handed versions of the matter particle and their antimatter partner. The weak interaction differentiates right-handed particles from left-handed ones, which is reflected in how neutrinos interact. A brief description of neutrino interactions can be found in Section 1.2.

The zero-mass neutrino hypothesis proposed by the SM has turned out to disagree with the observations of neutrino oscillations in the Super-Kamiokande (SK) detector in Japan [22], and in the Canadian experiment called Sudbury Neutrino Observatory (SNO) [23, 24], and subsequently confirmed by series of other experiments. The phenomenology of neutrino oscillations and the most important experimental results are briefly presented in Sections 1.3 - 1.5.

1.2 Neutrino interactions

The most typical materials used for detectors in experiments to study neutrinos produced at accelerator centres, like the SBN program being a subject of this thesis, are water, scintillators, Ar, or heavier elements like Fe or Pb. This means that at the relevant energy range from tens of MeVs to few GeVs, one should consider neutrino interactions with atomic electrons and with nucleons inside nuclei. However, due to a difference of mass between the nucleons and the electron, the total cross-section for the neutrino-nucleon interaction is roughly 2000 times larger than for the neutrino-electron interactions. Thus I will limit this brief introduction to discussing the neutrino-nucleon interactions.

Since neutrinos are neutral leptons, they interact with matter only via the weak force. Mediating bosons exchanged during these interactions are $W^{\pm}$ and Z^0. Depending on which one of these particles mediates in the interaction, there are two kinds of weak interactions. The first one is called the charged-current (CC) interaction because it is mediated by W^- or W^+ bosons, which carry an electric charge. The second one is called the neutral-current (NC) interaction because it is mediated by the Z^0 boson, which is a neutral particle.

Examples of Feynman diagrams for these two types of neutrino interactions with nucleons are shown in Figure 1.3. One can see that the type of charged lepton produced in the neutrino CC interaction can be used to identify the interacting neutrino flavour. The neutrino and antineutrino interactions are distinguished by the lepton charge: negative for neutrinos and positive for antineutrinos.

There is another way to classify the neutrino interactions based on the final state of the nucleon. If the final state of the nucleon does not change after neutrino scattering (except for momentum transfer), we call the scattering *elastic*. If the final state changes, we call the scattering *inelastic*. In the case of charged-current, there

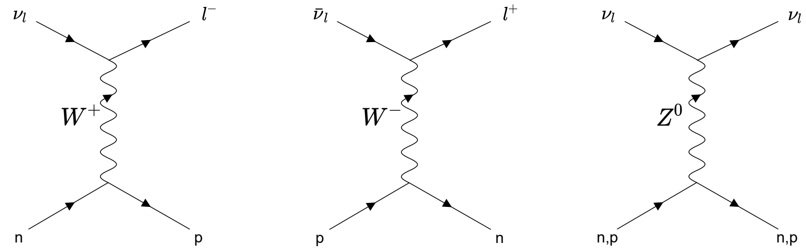

(a) ν CC interaction. (b) $\bar{\nu}$ CC interaction. (c) ν NC interaction.

Figure 1.3: Examples of Feynman diagrams for charged- and neutral- current scattering of a neutrino and antineutrino of flavour l from a nucleon.

is also a *quasi-elastic* (CCQE) interaction when the nucleon changes but does not break up and is not promoted to a resonant state.

Feynman diagrams showing the charged-current quasi-elastic (CCQE) interaction channels for neutrinos and antineutrinos are presented in Figures 1.3a and 1.3b, respectively. The CCQE interactions are essential in the neutrino oscillation analyses because for them it is possible to reconstruct the neutrino energy from only the energy and direction measurements of the final lepton, with an accuracy limited by how well the initial nucleon energy and momentum inside the nucleus can be known.

There are also two other interaction modes worth mentioning: resonance production (RES) and deep inelastic scattering (DIS).

In the NC and CC resonance production channels, neutrinos can excite the struck nucleon to a baryonic resonance, usually Δ (1232). The resonance decays back to a nucleon, which is usually accompanied by a single pion. In scattering off of free nucleons, there are seven possible resonant pion reaction channels (and seven for antineutrino scattering), three charged-current:

$$\nu_l + p \rightarrow l^- + p + \pi^+,$$
$$\nu_l + n \rightarrow l^- + n + \pi^0,$$
$$\nu_l + n \rightarrow l^- + n + \pi^+,$$

and four neutral-current:

$$\nu + p \rightarrow \nu + p + \pi^0,$$
$$\nu + p \rightarrow \nu + n + \pi^+,$$
$$\nu + n \rightarrow \nu + n + \pi^0,$$
$$\nu + n \rightarrow \nu + p + \pi^-.$$

The most common model of a single pion production through baryon resonances description is based on the calculations from Rein and Sehgal [25].

At higher neutrino energies, the neutrino can start to resolve the internal structure of the target in a process known as deep inelastic scattering. In DIS interaction mode, the neutrino can scatter off a quark inside the nucleon via the exchange of a $W^{\pm}$ or Z^0 boson producing a lepton and a jet of hadrons, which are mostly pions as shown in Figure 1.4.

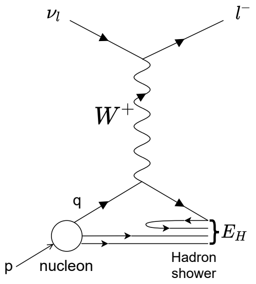

Figure 1.4: Feynman diagram for a CC DIS neutrino interaction. For the NC DIS interaction, the outgoing lepton is instead a neutrino and the exchange particle is a Z^0 boson. Figure reproduced from [26].

CCQE and RES are the most common neutrino interaction types at the GeV energy scale, which is the relevant region for the work described in this thesis while DIS dominates for energies above ∼10 GeV.

Finally, between the CCQE-dominant and RES-dominant neutrino energy regions, neutrino interactions can also arise from two-particle two-hole (2p2h) processes [27]. This happens when neutrino scatters on a pair of nucleons interacting with each other through meson exchange currents (MEC), resulting in a multi-nucleon final state. The MEC interaction mode is still an active area of research, which should improve the understanding of nuclear effects for neutrino-nuclear models.

The hadronic products of neutrino interactions can re-interact inside the target nucleus. These re-interactions are known as Final State Interactions (FSI). At low neutrino energies, for the most frequently produced mesons in the primary interactions - π mesons - the most common FSI are the elastic scattering (π + N $\rightarrow$ π + N), pion absorption (π + N $\rightarrow$ N') and charge exchange reactions (π^+ + n $\leftrightarrow$ π^0 + p, π^- + p $\leftrightarrow$ π^0 + n). Nucleons produced in neutrino interactions also undergo analogous FSI.

Due to their extremely low interaction cross sections, of the order of 10^{-38} cm^2 per nucleon for 1 GeV, neutrino interactions are very difficult to observe. However, the knowledge of neutrino interaction cross-section is essential for oscillation neutrino experiments, as it is there one of the main sources of systematic errors. Figure 1.5 illustrates the measurements of the ν_μ and $\bar{\nu}_\mu$ CC interaction cross-sections from various experiments as a function of neutrino energy. A linear dependence of the cross-section on neutrino energy is visible at the higher energies. For intermediate energy region (from tens of MeVs to few GeVs), where most accelerator-based neutrino experiments operate, multiple processes play an important role, and the available measurements are not sufficient to properly model the neutrino interactions for this energy regime.

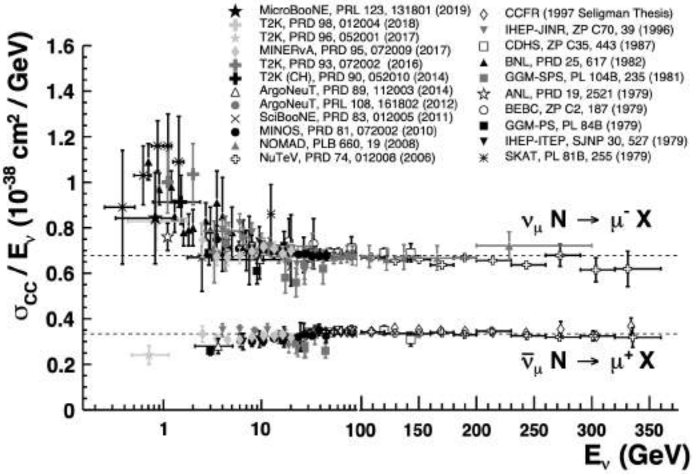

Figure 1.5: Measured ν_μ and $\bar{\nu}_\mu$ CC inclusive cross sections divided by the neutrino energy plotted as a function of neutrino energy, where N denotes a nucleon within the target. The dotted lines indicate the world-averaged cross sections, $\sigma^\nu/\mathrm{E}_\nu = (0.677 \pm 0.014) \times 10^{-38}$ cm^2/GeV and $\sigma^{\bar{\nu}}/\mathrm{E}_\nu = (0.334 \pm 0.008) \times 10^{-38}$ cm^2/GeV for neutrinos and antineutrinos, respectively [28]. Figure from [17].

This problem is further complicated by the fact that the nucleons subject to neutrino interactions are usually parts of the nucleus. This means that they are not at rest and have non-zero momentum, which must be considered. A primary interaction of neutrino can happen on an entire nucleus, on a single nucleon bound in a nuclear potential or on a quark. Thus, it is critical to have nuclear models that can reliably describe the dynamics of bound nucleons. Moreover, as already mentioned, the products of neutrino primary interactions on a nucleon or quark are propagated through a nuclear medium and can undergo the FSI. All these effects impact neutrino interaction cross sections and change the types, multiplicity and momenta of the observed particles. Nuclear effects must be well-understood to avoid biases in neutrino oscillation analyses [29].

1.3 Neutrino oscillations

In 1957 B. Pontecorvo introduced the idea of neutrino oscillations [30]. This was further developed by Z. Maki, M. Nakagawa, and S. Sakata [31]. A summary of this phenomenon, which is possible only for massive neutrinos is the subject of this section.

1.3.1 Oscillation in vacuum for three neutrino flavours

Neutrino oscillation is a quantum mechanical phenomenon in which a neutrino changes its flavour as it travels. Three flavours of neutrino (ν_{e}, ν_μ, ν_τ) are created and observed through weak interactions and hence are regarded as weak eigenstate neutrinos. Oscillations require that at least two neutrinos have non-zero masses. In such a case, mass eigenstates are not necessarily identical to the weak (flavour) eigenstates, i.e., the mass-matrix of neutrinos written on a flavour basis is not diagonal. For three active neutrinos the mixing of the flavour and mass eigenstates can be described by:

$$|\nu_\alpha\rangle = \sum_{i=1}^{3} U^*_{\alpha i}|\nu_i\rangle; \begin{pmatrix} \nu_e \\ \nu_\mu \\ \nu_\tau \end{pmatrix} = \begin{pmatrix} U_{e1} & U_{e2} & U_{e3} \\ U_{\mu 1} & U_{\mu 2} & U_{\mu 3} \\ U_{\tau 1} & U_{\tau 2} & U_{\tau 3} \end{pmatrix} \begin{pmatrix} \nu_1 \\ \nu_2 \\ \nu_3 \end{pmatrix}, \tag{1.2}$$

where α denotes a flavour (e, μ, τ), i stands for a mass state (1, 2, 3) and $\mathbf{U}$ is a unitary leptonic mixing matrix also known as the Pontecorvo-Maki-Nakagawa-Sakata (PMNS) matrix. This matrix is analogous to the Cabibbo–Kobayashi–Maskawa (CKM) matrix known from the quark sector.

In principle, a 3×3 unitary matrix has nine free parameters, however, only four of them generate oscillations, while the others can be absorbed as phases. It is therefore common that the PMNS matrix $\mathbf{U}$ is defined by three rotation matrices using three mixing angles θ_{ij} between the mass eigenstates i and j, and one Dirac-type Charge-Parity (CP) phase δ_{CP} (equation (1.3), where $c_{ij} = \cos\theta_{ij}$ and $s_{ij} = \sin\theta_{ij}$). If neutrinos are Majorana particles, there are two additional Majorana phases, but even in this case, oscillations are not sensitive to them, thus in neutrino oscillations studies, they can be neglected.

$$\mathbf{U} = \begin{pmatrix} 1 & 0 & 0 \\ 0 & c_{23} & s_{23} \\ 0 & -s_{23} & c_{23} \end{pmatrix} \begin{pmatrix} c_{13} & 0 & s_{13}e^{-i\delta_{CP}} \\ 0 & 1 & 0 \\ -s_{13}e^{i\delta_{CP}} & 0 & c_{13} \end{pmatrix} \begin{pmatrix} c_{12} & s_{12} & 0 \\ -s_{12} & c_{12} & 0 \\ 0 & 0 & 1 \end{pmatrix} \tag{1.3}$$

The first matrix in this formula is linked to the solar or 12-sector, the second one to the 13-sector, and the third one to the atmospheric or 23-sector. The 13-sector describes the connection between the solar and atmospheric regimes and can be used to determine δ_{CP} related to the CP conservation or violation for neutrinos. When multiplied out, the PMNS matrix has the form given by equation (1.4).

$$\mathbf{U} = \begin{pmatrix} c_{12}c_{13} & s_{12}c_{13} & s_{13}e^{-i\delta_{CP}} \\ -s_{12}c_{23} - c_{12}s_{23}s_{13}e^{-i\delta_{CP}} & c_{12}c_{23} - s_{12}s_{13}s_{23}e^{-i\delta_{CP}} & c_{13}s_{23} \\ s_{12}s_{23} - c_{12}s_{13}c_{23}e^{-i\delta_{CP}} & -c_{12}s_{23} - s_{12}s_{13}c_{23}e^{-i\delta_{CP}} & c_{13}c_{23} \end{pmatrix} \tag{1.4}$$

The probability of a transition of the initial neutrino with α-flavour and energy E into the final β-flavour after travelling a distance L in vacuum is given by:

$$P(\nu_\alpha \to \nu_\beta) = P_{\alpha\beta} = \left| \sum_j U_{\beta j}\; e^{\frac{-i\; m_j^2 L}{2E}} U_{\alpha j}^* \right|^2 , \tag{1.5}$$

$$\begin{aligned} P_{\alpha\beta} = \delta_{\alpha\beta} - 4\sum_{i>j} \mathrm{Re}(U_{\alpha i}^* U_{\beta i} U_{\alpha j} U_{\beta j}^*) \sin^2(\Delta m_{ij}^2 \frac{L}{4E}) \\ +2\sum_{i>j} \mathrm{Im}(U_{\alpha i}^* U_{\beta i} U_{\alpha j} U_{\beta j}^*) \sin(\Delta m_{ij}^2 \frac{L}{2E}) \;. \end{aligned} \tag{1.6}$$

The $\Delta m_{ij}^2 = m_i^2 - m_j^2$ parameter is a mass splitting of two mass eigenstates i and j, and neutrino oscillations are sensitive to this mass-squared difference, but not to the absolute neutrino masses. The oscillatory nature of neutrinos is visible in the equation (1.6), where the probability of a neutrino changing flavour oscillates as a function of L/E. This equation also demonstrates that a neutrino flavour change can only occur if neutrinos have some non-zero mass. As long as all neutrino masses are zero, ($\Delta m_{ij}^2 = 0$ for all i and j), the equation (1.6) reduces to $P_{\alpha\beta} = \delta_{\alpha\beta}$, so no flavour change can occur.

The last term in equation (1.6) contains the CP-violating part. This means that the measurement of δ_{CP} can be performed only in the so called appearance experiment ($\alpha \neq \beta$), since for the disappearance experiment ($\alpha = \beta$) this term becomes zero ($\mathrm{Im}(\|U_{\alpha i}\|^2 \|U_{\alpha j}\|^2) = 0$).

To summarise, for three neutrino flavour states and three mass states, the oscillation probabilities are described by six theoretical parameters: the two mass splitting Δm_{12}^2 and $|\Delta m_{23}^2|$, the three mixing angles θ_{12}, θ_{23}, θ_{13} and the δ_{CP} phase, to be determined experimentally. In addition, there are two possible mass orderings for neutrinos, according to the positive or negative sign of Δm_{23}^2, which are called the normal ordering (NO) and the inverted ordering (IO), respectively. The distance L and the neutrino energy E are used to optimise the experiments dedicated to studies of neutrino oscillations.

The δ_{CP}, if non-zero (and not equal to π), implies that CP violation occurs in the lepton sector, which would satisfy one of the three *Sakharov conditions* [32] and may therefore be essential for understanding matter-antimatter asymmetry in the Universe.

The current status of the oscillation parameters as measured by various experiments will be presented in Section 1.5.

1.3.2 Two flavour approximation

Due to the low values of $\sin\theta_{13}$ and thus negligible U_{e3}, the two-flavour oscillation formalism served as a good approximation to represent oscillation parameters derived from the results of the initial oscillation experiments for the atmospheric, solar, accelerator and reactor neutrinos. The simplified formula of the oscillation probability in vacuum for only two flavours comes from the original one assuming no CP violation ($\delta_{CP} = 0$) and $\theta_{13} = 0$. In that case, the oscillation probability depends on the ratio $\mathrm{L}/\mathrm{E}_{\nu}$, where L is the distance from the neutrino source to the detector and E_{ν} is the neutrino energy, the difference of the squares of the masses of the two-mass states ($\Delta\mathrm{m}^2$) and their mixing angle θ. Thus, the equation (1.6) becomes:

$$\mathrm{P}_{\alpha\beta} = \sin^2 2\theta \sin^2 \frac{\Delta m^2 L}{4E_{\nu}} \tag{1.7}$$

for the appearance of the neutrinos with flavour β among the initial neutrinos of flavour α, while the probability describing the disappearance of neutrinos with flavour α is given by the formula:

$$P(\nu_{\alpha} \rightarrow \nu_{\alpha}) = P_{\alpha\alpha} = 1 - P_{\alpha\beta}. \tag{1.8}$$

1.3.3 Neutrino oscillations in matter

The probability of oscillation becomes more complex when a neutrino passes through dense matter due to the weak interaction between the neutrinos and ordinary matter (i.e., electrons, protons and neutrons). Neutrinos of all flavours interact with matter through the NC interaction mediated by the Z^0 boson. These contributions are the same for all three flavours of neutrinos, leading to an overall phase that can be subtracted. The ordinary matter contains electrons but no muons or tau leptons, giving an additional contribution to electron neutrinos due to their CC interactions with electrons, mediated by the $\mathrm{W}^{\pm}$ exchange. The extra potential associated with matter is given by:

$$A = \pm 2\sqrt{2} G_F N_e E, \tag{1.9}$$

where G_F is the Fermi constant, N_e is the electron density, and E is the neutrino energy. The positive sign is for neutrinos, and the negative sign is for antineutrinos. This has a substantial impact on the oscillation probability and gives rise to additional interesting effects, such as the Mikheev-Smirnov-Wolfenstein (MSW) resonance and neutrino-antineutrino asymmetry [33, 34], [35, and references therein], in addition to the neutrino-antineutrino asymmetry in the case of the CP non-conservation.

The use of an appearance channel where the neutrino changes flavour between production and detection is necessary to probe CP violation in the neutrino sector, with the transition probabilities P($\nu_\mu \to \nu_e$) and P($\bar{\nu}_\mu \to \bar{\nu}_e$) to explore simultaneously the neutrino mass ordering and CP violation. Matter effects are significant in long-baseline neutrino experiments, and the exact expressions of the three-flavour oscillation probabilities, including matter effects, are very complicated. The approximate analytic expression for the P$_{\mu e}$ probability with terms up to the second-order in θ_{13}, is given by the following equation:

$$\begin{aligned} P_{\mu e} \simeq & \underbrace{\sin^2\theta_{23}\sin^2 2\theta_{13}\frac{\sin^2[(1-\hat{A})\Delta]}{(1-\hat{A})^2}}_{C_0} + \underbrace{\alpha^2\cos^2\theta_{23}\sin^2 2\theta_{12}\frac{\sin^2(\hat{A}\Delta)}{\hat{A}^2}}_{C_1} \\ & \underbrace{\mp\,\alpha\sin 2\theta_{13}\cos\theta_{13}\sin 2\theta_{12}\sin(\Delta)\frac{\sin(\hat{A}\Delta)}{\hat{A}}\frac{sin[(1-\hat{A})\Delta]}{(1-\hat{A})}}_{C_-}\sin\delta_{CP} \\ & +\underbrace{\alpha\sin 2\theta_{13}\cos\theta_{13}\sin 2\theta_{12}\cos(\Delta)\frac{\sin(\hat{A}\Delta)}{\hat{A}}\frac{sin[(1-\hat{A})\Delta]}{(1-\hat{A})}}_{C_+}\cos\delta_{CP}, \end{aligned} \tag{1.10}$$

where

$$\alpha \equiv \Delta m^2_{21}/\Delta m^2_{31},\ \Delta \equiv \frac{\Delta m^2_{31}L}{4E},\ \hat{A} \equiv \frac{A}{\Delta m^2_{31}}.$$

This equation has been derived under the constant matter density approximation [36, 37], where A, E and N_e are defined like in equation 1.9. The '-' sign, which precedes the term C$_-$, refers to neutrinos, whereas the '+' refers to antineutrinos. The C$_0$ term can be used to derive the θ_{13} value. It also contains the largest Earth matter effect and can be used to measure the sign of Δm$^2_{31}$. The C$_1$ term is independent of both θ_{13} and δ_{CP} and depends mainly on the solar parameters, Δm$^2_{21}$ and θ_{12}. The C$_-$ term is the CP-violating part. The term C$_+$, although δ_{CP}-dependent, is CP-conserving.

1.4 Discovery of neutrino oscillations

In the late 1960s, R. Davis and collaborators devised the experiment to measure solar neutrinos in the Homestake Mine in South Dakota [38]. The goal was to measure solar neutrinos produced in the ^{8}B decay ($^8_5$B $\to ^8_4$Be + e$^+$ + ν_e) - using the radiochemical method of detection of the reaction ν_e + Cl $\to$ e$^-$ + Ar. The results published in 1968 were unexpected due to the upper bound on the solar ν_e flux that was about three times smaller than the prediction of the Solar Standard Model (SSM) [39]. This was later called the *solar neutrino puzzle.*

In the early 1990s, the additional evidence for ν_e disappearance came from the GALLEX [40] and SAGE [41] experiments. As in Davis' experiment, both used radiochemical detection methods, but in this case with Gallium instead of Chlorine: ν_e + ^{71}Ga → e$^-$ + ^{71}Ge. This reaction with a much lower threshold than ν_e + Cl allowed physicists to measure lower-energy solar neutrinos produced in the solar pp-cycle, which was well-known and understood at the time. Both experiments measured around half of the predicted event rate, but significantly more than the flux measured in Davis' experiment. This was additional strong evidence for ν_e disappearance.

The Kamiokande experiment using a large water Cherenkov detector, originally intended to measure proton decay, produced a measurement of the solar neutrino flux that supported Davis' result [42]. Solar ν_e were detected via the elastic scattering (ES) reaction, ν_x + e$^-$ → ν_x + e$^-$, , in which the ν_e is privileged, because of interacting via both, weak charge current and weak neutral current, while ν_μ and ν_τ have only neutral current interactions. The ratio of observed to predicted flux was found at around $\frac{1}{2}$.

The solution to the solar neutrino puzzle came from the SNO experiment. As Davis' and Kamiokande experiments, they measured mostly high energy neutrinos from solar ^{8}B decay, but SNO measured both the ν_e flux (through CC interactions ν_e + d → p + p + e$^-$, which only occur for ν_e), and the total neutrino flux (via flavour-independent NC interactions, ν_x + d → p + n + ν_x). Like Kamiokande, it also measured the ES reaction, ν_x + e$^-$ → ν_x + e$^-$. The SNO collaboration published the initial result in 2001 of CC measurement [23] and in 2002 the result of NC measurement [24] and established, at 5.3σ statistical significance, that neutrinos change flavour. The measured total neutrino flux was in agreement with the Standard Solar Model (Figure 1.6), and the measured ratio of the ν_e flux to the total neutrino flux was 0.301 ± 0.033. This gave very strong evidence that ν_e were changing flavour into ν_μ and/or ν_τ in the Sun.

In 2003 the Kamioka Liquid Scintillator AntiNeutrio Detector (KamLAND) collaboration provided solid evidence for the oscillation of $\bar{\nu}_e$ produced in nuclear reactors [44] by measuring antineutrinos produced in 55 Japanese nuclear power reactors, with a baseline of ∼180 km between production and detection. Not only did they observe fewer $\bar{\nu}_e$ than expected, but they were also able to show neutrino oscillation as a function of L/E$_\nu$, which is shown in Figure 1.7.

Combined results from all the solar experiments together with KamLAND strengthened the SNO solution to the solar neutrino puzzle. It turned out that the oscillations do not happen on the way from the Sun to the Earth, but the conversion is already done within the Sun due to matter effects, which was the MSW adiabatic flavour transitions in the solar matter. The so-called large mixing angle solution, with parameters $\Delta \mathrm{m}^2 \sim 7.5 \times 10^{-5}$ eV^2 and $\sin^2\theta \sim 0.3$ restricted the oscillation parameters to a very narrow range.

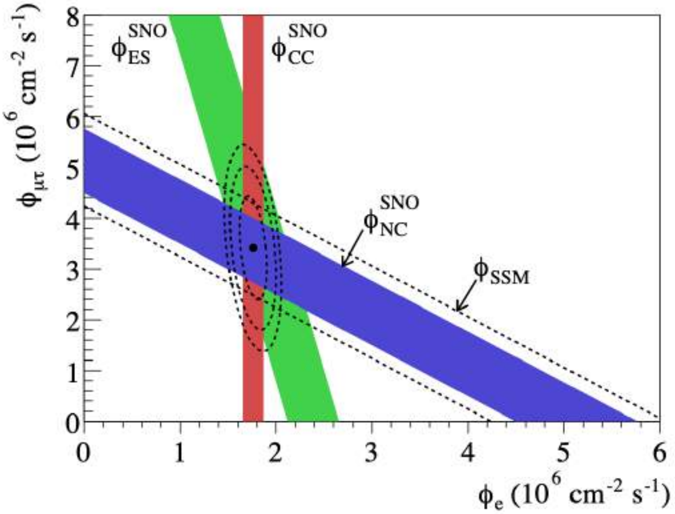

Figure 1.6: The fluxes of the solar neutrinos (ν_e and $\nu_{\mu,\tau}$) measured by SNO. The diagonal dashed lines show the total flux predicted by the SSM [43] and the diagonal blue bands represent the total flux measured with the NC reaction in SNO. The bands intercepts with the axes illustrate the $\pm 1\sigma$ errors. Figure from [24].

In 1998, the Super-Kamiokande (SK) collaboration published a measurement of atmospheric ν_μ disappearance [22] of which hints had been seen previously in the Kamiokande [42], and Irvine-Michigan-Brookhaven (IMB) [46] water Cherenkov detectors. The discrepancy between the observed and expected rate of electron and muon neutrino interactions in underground detectors is known as the *atmospheric neutrino anomaly*. The ν_μ disappearance observed by Super-Kamiokande in the atmospheric data can be well explained by the presence of $\nu_\mu \leftrightarrow \nu_\tau$ oscillation. The oscillation parameters fitted to SK data were given by $\Delta m^2 = 2.5 \times 10^{-3}$ eV^2 with $\sin^2 2\theta = 1.0$. The range of allowed values at 90% confidence level corresponds to $5 \times 10^{-4} < \Delta m^2 < 6 \times 10^{-3}$ eV^2 and $\sin^2 2\theta > 0.82$ [22]. Due to a good ability of SK to measure the neutrino direction, the flux of atmospheric ν_μ was measured as a function of incoming angle. By separating the atmospheric neutrinos into two samples, up-going and down-going, it was possible to measure neutrino oscillations over two different baselines in the same detector. Down-going neutrinos have a path length from the production point in the atmosphere of around 20 − 500 km, whereas up-going neutrinos, most of which pass through the Earth, have a path length from around 500 − 12,000 km. Assuming that cosmic rays (that produce neutrinos visible in Super-Kamiokande) are isotropic and there is no ν_μ disappearance, equal fluxes for the up-going and down-going neutrinos were predicted. However, the results from

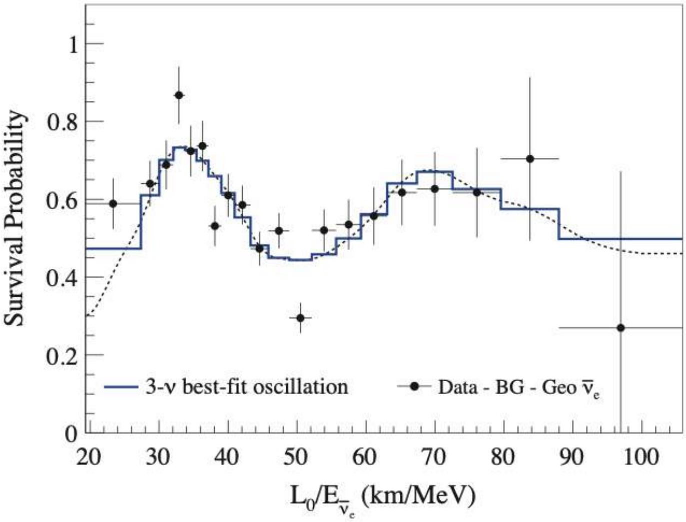

Figure 1.7: The ratio of measured $\bar{\nu}_\mathrm{e}$ spectrum to the predicted non-oscillation one with respect to the $\mathrm{L_0/E}$ ($\mathrm{L_0}$ = 180 km) for the KamLAND events. The oscillatory behaviour is clearly seen. Figure from [45].

SK gave an up-going neutrino flux of around half of the down-going flux, proving that the number of observed ν_μ depends on the distance between the neutrino production point in the atmosphere and the detector. The zenith angle distributions of atmospheric neutrino events from Super-Kamiokande are illustrated in Figure 1.8. For a broad range of neutrino energy and path length, the observed distributions are consistent with neutrino oscillation expectations. Coming four years before the SNO result, this was strong evidence for neutrino oscillation. At high $\mathrm{L/E}_\nu$, the observed ν_μ flux was around 50% of the prediction – clear evidence for ν_μ disappearance. Because within errors the ν_e was independent of the zenith angle this gave strong evidence that ν_μ were changing flavour into ν_τ.

The K2K (KEK to Kamioka) experiment was the first long-baseline neutrino experiment that ran in 1999 - 2004 with a baseline of 250 km between the accelerator neutrino source at KEK and the SK detector. The K2K near detectors, located 300 m downstream of the production target, based on a combination of a 1 kt water Cherenkov detector and a set of fine-grained detectors, measured the neutrino flux before the oscillations. Looking at the 1.3 GeV beam, the K2K experiment confirmed the ν_μ disappearance originally reported by Super-Kamiokande atmospheric neutrino observation [47].

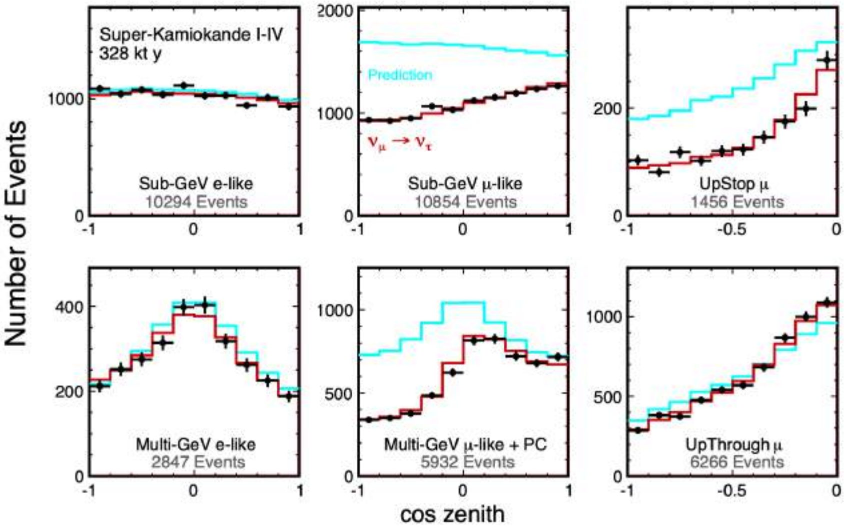

Figure 1.8: The zenith angle distributions of Super-Kamiokande atmospheric neutrino data. Figure taken from [17].

1.5 Current status of experimental studies and global fits for three neutrino flavours

Since discovering neutrino oscillations, many other experiments have provided improved measurements and more robust evidence for neutrino oscillations. The evidence is now overwhelmingly strong that neutrino oscillations do occur, and the focus in the field has moved into a precise determination of the theoretical parameters.

A summary of the current world's best results (as presented by the Particle Data Group in the 2020 update [17]) is discussed below. In table 1.1 the different experiments which dominantly contribute to the present determination of the six parameters in the framework of the three neutrino flavours are summarised.

θ_{12} and Δm^2_{21}:

The best estimation of the solar mixing angle, θ_{12}, comes from a 3-neutrino oscillation fit to global solar neutrino and KamLAND data, using constraints on θ_{13} from accelerator and short-baseline reactor neutrino experiments. The mass splitting Δm^2_{21} measurement comes again from KamLAND, and global solar neutrino fit as the measurement of θ_{12} [45]. The Jiangmen Underground Neutrino Observatory (JUNO), a future reactor experiment, is expected to measure the solar parameters

Table 1.1: Experiments contributions to the current determination of the oscillation parameters. Table reproduced from [17].

Experiment	Dominant	Important
Solar Experiments	θ_{12}	Δm^2_{21}, θ_{13}
Reactor LBL (KamLAND)	Δm^2_{21}	θ_{12}, θ_{13}
Reactor MBL (Daya-Bay, Reno, D-Chooz)	θ_{13}, $\|\Delta m^2_{31,32}\|$	
Atmospheric Experiments (Super-Kamiokande, IC-DC)		θ_{23}, $\|\Delta m^2_{31,32}\|$, θ_{13}, δ_{CP}
Accel LBL ν_μ, $\bar{\nu}_\mu$, Disapp (K2K, MINOS, T2K, NOνA)	$\|\Delta m^2_{31,32}\|$, θ_{23}	
Accel LBL ν_e, $\bar{\nu}_e$ App (MINOS, T2K, NOνA)	δ_{CP}	θ_{13}, θ_{23}

even more accurately [48].

θ_{13}:

The most precise measurement of θ_{13} comes from the reactor experiments Daya Bay in China [49], Reactor Experiment for Neutrino Oscillation (RENO) in Korea [50], and Double Chooz in France [51]. These three experiments employ a similar detector design optimised to precisely measure reactor antineutrinos using Gadolinium-doped liquid scintillator as the primary antineutrino target. The Daya Bay experiment [52], the most advanced among the three, has eight antineutrino detectors; two detectors located at 470 m, two detectors located at 576 m and four detectors at 1648 m away from the reactors. RENO [53] has two identical detectors located at 294 m and 1383 m from the centre of an array of six reactors. The Double Chooz has finished data taking in early 2018. Its far detector was located at ∼1050 m from the reactors and the near detector at 400 m [54].

θ_{23} and $|\Delta\ m^2_{31,32}|$:

The world-leading contours in $\sin^2\theta_{23} - \Delta m^2_{32}$ space are coming from long-baseline (LBL) accelerator experiments, but are also measured by atmospheric experiments.

The most important measurements based on atmospheric data come from Super-Kamiokande [55] and IceCube DeepCore (IC-DC) [56, 57]. IceCube is a telescope detector in ice located in Antarctica at the South Pole at a depth between 1.45 and 2.45 km, while DeepCore is its bottom centre with denser PMT spacing to observe the lower neutrino energy region. The mixing angle, θ_{23}, is slightly better measured by Super-Kamiokande, while DeepCore provides a better estimation of the atmospheric mass splitting.

Among the LBL accelerator experiments, the best measurements are provided by the Tokai to Kamioka (T2K) [58], K2K [47], Main Injector Neutrino Oscillation Search (MINOS) [59], and the NuMI Off-Axis ν_e Appearance (NOνA) [60] experiments[1]. The T2K experiment studies muon neutrino beam produced in the Japan Proton Accelerator Research Complex (J-PARC) in Tokai and sent over 295 km to the Super-Kamiokande detector. In 2011, the T2K collaboration published the first sign of $\nu_\mu \leftrightarrow \nu_\mathrm{e}$ oscillation with a statistical significance of 2.5σ [62], while in 2014 this transition was established by T2K with more than 7σ [63]. The pioneering K2K experiment [47] is still included in the global fits, but with a sensitivity to the oscillation parameters that has been overcome by the more recent long-baseline accelerator experiments. The MINOS experiment used a Neutrinos at Main Injector (NuMI) beam from Fermilab and a detector in Soudan mine 735 km away. The MINOS experiment measured oscillation parameters by combining the accelerator and atmospheric neutrino events in both disappearance and appearance modes [64, 59]. The NOνA experiment based on far detector located at 810 km away from the NuMI off-axis beam source confirmed the ν_e appearance from ν_μ beam and using the antineutrino beam data, it reported the observation of $\bar{\nu}_e$ appearance from $\bar{\nu}_\mu$ beam with 4.4σ significance [60].

$\boldsymbol{\delta_{CP}}$:

The best measurements of the CP-violating phase, δ, can be obtained by the long-baseline accelerator experiments like T2K and NOνA. Recently, the T2K collaboration reported a hint of CP-violating values of δ with more than 2σ [65, 66, 67]. The latest neutrino and antineutrino NOνA data prefer values of δ_{CP} close to 0.8π for normal mass ordering. Some values of the CP-violating phase δ_{CP} have been excluded by the NOνA experiment for the inverted mass ordering. In contrast, no significant limit has been set for the case of normal mass ordering [61]. T2K shows a slightly better sensitivity to δ_{CP} for inverted neutrino mass ordering, while both experiments show similar sensitivity for normal neutrino mass ordering.

Based on the experiments mentioned above, the values of the three-neutrino oscillation parameters are presented in Table 1.2. In that last respect, the main difference resides in the results from Super-Kamiokande atmospheric data [68] which, at present, can only be included in these analyses by directly adding the χ^2 provided by the experiment.

In all analyses, the best fit is for the normal mass ordering. Inverted ordering is disfavoured with a $\Delta\chi^2$ which ranges from slightly above 2σ – driven by the interplay of long-baseline accelerator and short-baseline reactor data – to 3σ when adding the atmospheric χ^2 table from [55].

---

[1] By the time of writing this thesis the updated analysis from NOνA collaboration were reported [61].

Table 1.2: Three-flavour oscillation parameters from the fit to global data performed by [69]. The numbers in the first (second) column are obtained assuming NO (IO). The results are shown with inclusion of the results of the Super-Kamiokande atmospheric neutrino data (the tabulated $\Delta\chi^2$). Table reproduced from [69].

	Normal Ordering (best fit)		Inverted Ordering ($\Delta\chi^2 = 7.1$)	
	bfp ± 1σ	3σ range	bfp ± 1σ	3σ range
$\sin^2\theta_{12}$	$0.304^{+0.012}_{-0.012}$	$0.269 \rightarrow 0.343$	$0.304^{+0.013}_{-0.012}$	$0.269 \rightarrow 0.343$
$\theta_{12}/^\circ$	$33.44^{+0.77}_{-0.74}$	$31.27 \rightarrow 35.86$	$33.45^{+0.78}_{-0.75}$	$31.27 \rightarrow 35.87$
$\sin^2\theta_{23}$	$0.573^{+0.016}_{-0.020}$	$0.415 \rightarrow 0.616$	$0.575^{+0.016}_{-0.019}$	$0.419 \rightarrow 0.617$
$\theta_{23}/^\circ$	$49.2^{+0.9}_{-1.2}$	$40.1 \rightarrow 51.7$	$49.3^{+0.9}_{-1.1}$	$40.3 \rightarrow 51.8$
$\sin^2\theta_{13}$	$0.02219^{+0.00062}_{-0.00063}$	$0.02032 \rightarrow 0.02410$	$0.02238^{+0.00063}_{-0.00062}$	$0.02052 \rightarrow 0.02428$
$\theta_{13}/^\circ$	$8.57^{+0.12}_{-0.12}$	$8.20 \rightarrow 8.93$	$8.60^{+0.12}_{-0.12}$	$8.24 \rightarrow 8.96$
$\delta_{CP}/^\circ$	197^{+27}_{-24}	$120 \rightarrow 369$	282^{+26}_{-30}	$193 \rightarrow 352$
$\frac{\Delta m^2_{21}}{10^{-5} eV^2}$	$7.42^{+0.21}_{-0.20}$	$6.82 \rightarrow 8.04$	$7.42^{+0.21}_{-0.20}$	$6.82 \rightarrow 8.04$
$\frac{\Delta m^2_{3l}}{10^{-3} eV^2}$	$+2.517^{+0.026}_{-0.028}$	$+2.435 \rightarrow +2.598$	$-2.498^{+0.028}_{-0.028}$	$-2.581 \rightarrow -2.414$

1.6 Open questions in neutrino physics

This section presents some open questions in neutrino physics that current and future neutrino experiments aim to address.

Determination of δ_{CP}

It has been known since the mid fifties that neither charge conjugation (C) nor parity (P) is a symmetry of weak interactions. For example, the mirror reflection of a left-handed neutrino is a right-handed neutrino. However, the CP transformation converts a left-handed neutrino into a right-handed antineutrino, which was considered acceptable. The first discovery of CP violation was for kaons [70]. Following the recent hint of a strong, if not maximal, violation of the CP symmetry in the neutrino sector, in various ongoing and future experiments, such as Hyper-Kamiokande and DUNE, physicists endeavour to find significant experimental evidence for CP violation in the lepton sector. This can help to explain the observed asymmetry between matter and antimatter in the Universe.

Neutrino mass ordering

The observation of neutrino oscillations means that at least two out of the three neutrino mass states (m_1, m_2, m_3) have different and non-zero masses. These masses are so small that they have not yet been directly measured. Solar neutrino oscillation experiments have determined the difference of the square of masses of m_1 and m_2 ($\Delta\mathrm{m}^2_{12} = \mathrm{m}^2_1$ - m^2_2). The atmospheric neutrino experiments have determined the difference of the square of masses m_1 and m_3 ($|\Delta\mathrm{m}^2_{13}| = |\mathrm{m}^2_1$ - $\mathrm{m}^2_3|$). However, the sign of $\Delta\mathrm{m}^2_{13}$ is unknown. This is known as the neutrino mass ordering problem. The normal ordering (NO) corresponds to the solar mass splitting below the atmospheric mass splitting (m_1 and m_2 smaller than m_3), while for the inverted ordering (IO) the m_3 mass state is the lowest one. Recent results of the NOνA experiment show weak preference for normal ordering, while the T2K results start to exclude the CP conservation for neutrinos. However, a joint analysis of NOνA and T2K results seem to favour an inverted ordering [71]. Precise future long-baseline experiments, DUNE in the US and Hyper-Kamiokande in Japan, will determine the mass ordering and δ_{CP} with sufficient precision to complete studies of the oscillation phenomenon within a three-neutrino oscillation model. The neutrino mass ordering affects the sensitivity of CP-violation measurements and sensitivity to determine if neutrinos and antineutrinos are identical particles or different.

Sterile neutrino(s)

The next open question in neutrino physics concerns the existence or non-existence of sterile neutrino(s). Sterile neutrinos are hypothetical neutrinos that interact via gravity only, unlike other neutrinos in the Standard Model, which interact also via the weak interaction. They are proposed to be right-handed. Some experiments demonstrate possible deviations from the three-neutrino oscillation model, pointing to another mass splitting value inconsistent with the solar and atmospheric splittings. If confirmed by solid experimental evidence, the third mass splitting would require at least one additional neutrino, called sterile. The most relevant results were obtained in the Liquid Argon Scintillator Detector (LSND) at Los Alamos National Laboratory in New Mexico [72], and MiniBooNE at Fermi National Accelerator Laboratory near Chicago [73] experiments. These experimental hints, described in detail in the next chapter, must be confirmed or excluded based on much better measurements. Therefore, searches for sterile neutrino (or neutrinos) are among the most important topics in neutrino physics. The SBN program at Fermilab has been designed to search for definitive evidence or exclusion the LSND-like sterile neutrinos.

Dirac or Majorana neutrino and neutrino masses

Another open problem in neutrino physics is whether a neutrino is a Majorana or a Dirac particle. If the fermion and its antiparticle are different, they are called Dirac particles, otherwise they are Majorana particles. In 1957, physicists found that neutrinos are left-handed, and antineutrinos are right-handed. This suggests that neutrinos are Dirac particles. However, since neutrinos have mass, it is possible to change the observer's reference system so that the direction of motion is opposite. For different observers, there will be uncertainty in the direction of neutrino motion, resulting in uncertainty in neutrino handedness. If neutrinos are Majorana particles, it is possible to observe a neutrinoless double β-decay. The discovery of such a decay would allow the determination of the absolute value of the neutrino masses, which cannot be determined from studies of oscillations.

Chapter 2

Sterile neutrinos

A sterile neutrino is a hypothetical neutral lepton that does not participate in the standard weak interaction. Term *sterile* was first used in this context by B. Pontecorvo in 1967 [74] when he considered oscillations of the active neutrinos into sterile neutrinos that cannot be detected. Among the four known fundamental interactions, only gravitational interactions, due to space-time geometry, are expected to affect sterile neutrinos. Thus, the occurrence of sterile neutrinos can have visible effects in cosmology and astrophysical environments. The existence of sterile neutrinos in temporal experiments can only be demonstrated through their mixing with active neutrinos. The search for these effects is crucial to our understanding of Nature since sterile neutrinos are non-standard particles that can open the way to reach new physics beyond the Standard Model.

2.1 Experimental indications

As presented in the previous chapter, experimental observations of neutrino oscillations have established a picture consistent with the mixing of three neutrino flavours (ν_e, ν_μ, ν_τ) with three mass eigenstates (ν_1, ν_2, ν_3) whose mass differences turn out to be relatively small, with $\Delta\mathrm{m}^2_{31}$=$(2.517^{+0.026}_{-0.028}) \times 10^{-3}$ eV^2 (NO) or $\Delta\mathrm{m}^2_{32}$=$(-2.498^{+0.028}_{-0.028}) \times 10^{-3}$ eV^2 (IO) and $\Delta\mathrm{m}^2_{21}$=$(7.42^{+0.21}_{-0.20}) \times 10^{-5}$ eV^2 [69]. However, several experimental *anomalies* have also been reported which, if confirmed, could be hinting at the presence of additional sterile neutrino states with larger mass-squared differences participating in the mixing [75].

The direct detection of sterile neutrinos is not possible because they do not interact even weakly. One can prove their existence through the observation of the modifications of the three active neutrino oscillations resulting from the additional mixing of sterile and active neutrinos. Experimental indications of such modifications are briefly presented in the following subsections, covering the anomaly observed in the LSND experiment for the $\bar{\nu}_\mu \to \bar{\nu}_e$ transitions and confirmed by the MiniBooNE experiment for both the $\nu_\mu \rightarrow \nu_e$ and the $\bar{\nu}_\mu \rightarrow \bar{\nu}_e$ transitions, the reactor anomaly for the $\bar{\nu}_e \rightarrow \bar{\nu}_e$ transitions and the Gallium anomaly for the $\nu_e \rightarrow \nu_e$ transitions.

2.1.1 LSND experiment

The first observation of potentially anomalous neutrino mixing was observed in $\bar{\nu}_\mu \rightarrow \bar{\nu}_e$ transitions at the Liquid Scintillator Neutrino Detector (LSND) [72].

The LSND detector at the Los Alamos National Laboratory was a short-baseline Cherenkov detector studying the $\bar{\nu}_\mu$ flux with energies up to 53 MeV. The detector filled with a liquid scintillator located roughly 30 m from the source was devised to observe ν_e events through the inverse beta decay process in Carbon, $\bar{\nu}_e + \mathrm{p} \rightarrow \mathrm{e}^+ + \mathrm{n}$ by detecting the Cherenkov and scintillation light produced by the e^+ and the delayed 2.2 MeV gamma-ray from neutron capture. The main backgrounds at LSND were standard $\bar{\nu}_e$ production in the beam stop and π^- decay in flight followed by $\bar{\nu}_\mu + \mathrm{p} \rightarrow \mu^+ + \mathrm{n}$ where the μ^+ is misidentified as an e^+. The experiment observed an excess of 87.9 ± 22.4 (stat.) ± 6.0 (syst.) $\bar{\nu}_e$ events over expected backgrounds (Figure 2.1), at 3.8σ confidence level [72]. That excess has been read as evidence for the $\bar{\nu}_\mu \rightarrow \bar{\nu}_e$ transition in the $\Delta\mathrm{m}^2$ range from 0.2 eV^2 to 2 eV^2. Such a range of $\Delta\mathrm{m}^2$ is conflicting with the widely accepted model of oscillations between three light neutrino species and would require the existence of at least one additional neutrino.

2.1.2 MiniBooNE experiment

The Mini Booster Neutrino Experiment (MiniBooNE) was designed to examine the LSND observation with higher precision. A mineral oil detector optimised to observe Cherenkov light emitted by electrons and muons was located 540 m downstream from the neutrino production target. The different energy configuration and event signature made MiniBooNE backgrounds very different from those in LSND. However, the higher energy and longer baseline made it sensitive to the same range of L/E, ensuring that MiniBooNE probes a mass squared splitting of $\mathcal{O}(1\ \mathrm{eV}^2)$, similarly to LSND.

The aim was to investigate the $\nu_\mu \rightarrow \nu_e$ and $\bar{\nu}_\mu \rightarrow \bar{\nu}_e$ transitions. After collecting 12.84 (11.27) $\times 10^{20}$ protons on target in neutrino (antineutrino) modes, the MiniBooNE collaboration has observed excesses of electron-like events in both modes (Figure 2.2), leading to a 4.7σ deviation from the expected background [76]. The extracted parameter values for the whole sample of collected data are consistent with the LSND values, strengthening the short-baseline anomaly.

2.1.3 Reactor antineutrino anomaly

Another short-baseline neutrino anomaly has been reported in the $\bar{\nu}_e$ disappearance mode in the detection of antineutrinos from nuclear reactors.

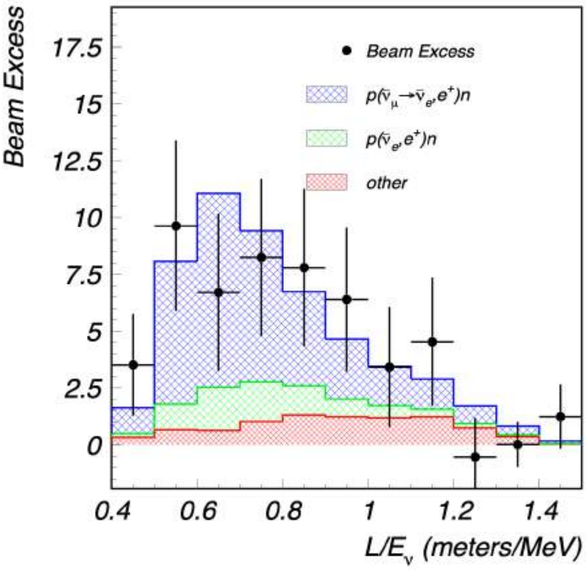

Figure 2.1: The excess of $\bar{\nu}_e$-like events observed as a function of L/E$_\nu$, where L is the distance travelled by the neutrino in meter and E$_\nu$ is the neutrino energy in MeV. The data agree well with the expectation from neutrino background and neutrino oscillations at Δm^2 of the order of 1 eV^2. Figure from [72].

A 2011 reevaluation of the flux of antineutrinos produced in reactors lifted the expected $\bar{\nu}_e$ flux by ∼3% [77, 78]. With the improved evaluation of theoretical uncertainties, this effect led to a shift in the ratio of the total observed events over the predicted number of events in many reactor experiments (Daya Bay [79, 80], RENO [81], STEREO [82]), with an average value of $R = 0.943 \pm 0.023$ [83]. This is the origin of the so-called *reactor anomaly*, which could be interpreted in terms of the additional sterile neutrino(s).

However, Ref. [84] reports a reanalysis of the reactor antineutrino energy spectra, pointing out to possible errors in predicting the $\bar{\nu}_e$ spectrum for reactor antineutrino fluxes. A new analysis of the conversion procedure based on the recent measurements of the ratio between the cumulative fission β spectra for ^{235}U and ^{239}Pu points to the new predictions that are consistent with the results of Daya Bay, RENO and STEREO experiments.

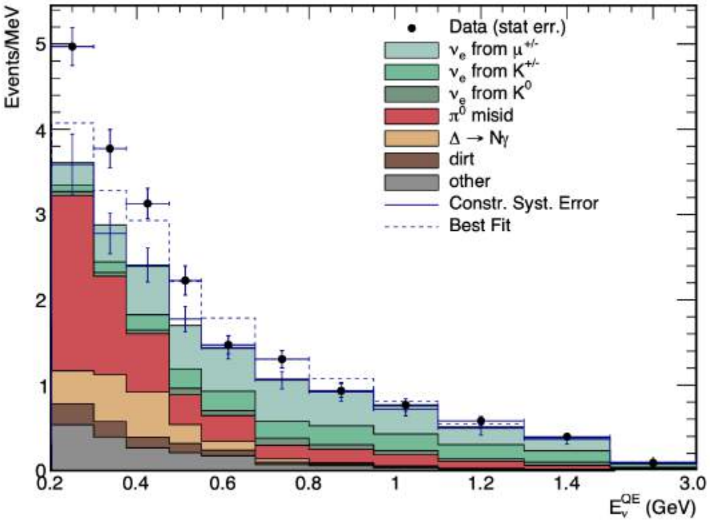

Figure 2.2: The MiniBooNE neutrino mode energy distributions for ν_e CCQE data and backgrounds. The dashed curve presents the best fit to the neutrino-mode data with the two-neutrino oscillation assumption. Neutrino event rate (black) observed by the MiniBooNE detector is significantly higher than expectations (multiple contributions stacked) from the null oscillation hypothesis. Excess is apparent in the low energy regime (below 600 MeV), where the photon background is dominant. Figure from [76].

2.1.4 Gallium anomaly

Calibration data from the Gallium solar neutrino experiments, such as GALLEX and GNO/SAGE [85, 86], using intense radioactive neutrino sources and the theoretical calculations of the cross-section for neutrino capture $\nu_e + {}^{71}\mathrm{Ga} \rightarrow {}^{71}\mathrm{Ge} + \mathrm{e}^-$ [87] lead to a 3σ deficit compared to the expected number of events [88, 89]. This is known as the *gallium anomaly*.

2.2 Phenomenology of sterile neutrinos

If sterile neutrinos exist, the number of their different species has to be determined. However, in this thesis, I will focus only on the most simplistic model. The simplest model is based on the assumption that apart from the three neutrino flavours there is only one sterile neutrino species.

A mixing matrix for this 3+1 scenario:

$$\begin{pmatrix} \nu_e \\ \nu_\mu \\ \nu_\tau \\ \nu_s \end{pmatrix} = \begin{pmatrix} U_{e1} & U_{e2} & U_{e3} & U_{e4} \\ U_{\mu1} & U_{\mu2} & U_{\mu3} & U_{\mu4} \\ U_{\tau1} & U_{\tau2} & U_{\tau3} & U_{\tau4} \\ U_{s1} & U_{s2} & U_{s3} & U_{s4} \end{pmatrix} \begin{pmatrix} \nu_1 \\ \nu_2 \\ \nu_3 \\ \nu_4 \end{pmatrix}, \tag{2.1}$$

can be parameterised as:

$$\mathrm{U} = \mathrm{R}_{34}(\theta_{34})\mathrm{R}_{24}(\theta_{24}\delta_{24})\mathrm{R}_{14}(\theta_{14})\mathrm{R}_{23}(\theta_{23})\mathrm{R}_{13}(\theta_{13}\delta_{13})\mathrm{R}_{12}(\theta_{12}\delta_{12}),$$

where R_{ij} denotes a rotation in the ij-plane by an angle θ_{ij} and a possible phase δ_{ij} (if present). One can recover the 3 active neutrino framework by setting $\theta_{i4} = 0$ for i = 1,2,3 and identifying δ_{13} with the 3 neutrino phase δ_{CP} and with δ_{12} becoming nonphysical.

In the case of $\Delta \mathrm{m}^2_{41} \gg |\Delta \mathrm{m}^2_{31}|, \Delta \mathrm{m}^2_{21}$, a two-flavour vacuum oscillation formula is a good approximation for the description of the oscillations at short-baseline experiments:

$$P_{\alpha\beta} = \delta_{\alpha\beta} - 4|U_{\alpha\beta}|^2(\delta_{\alpha\beta} - |U_{\alpha\beta}|^2) sin^2(\frac{\Delta m^2_{41} L}{4E}), \tag{2.2}$$

where L is the baseline and E is the neutrino energy.

As discussed in the previous subsections, the anomalies have been observed for the $\overset{(-)}{\nu}_\mu \rightarrow \overset{(-)}{\nu}_e$ and the $\overset{(-)}{\nu}_e \rightarrow \overset{(-)}{\nu}_e$ transitions. No deviation from the three neutrino framework has been recorded for the $\overset{(-)}{\nu}_\mu \rightarrow \overset{(-)}{\nu}_\mu$ transitions. Each oscillation channel $\nu_\alpha \rightarrow \nu_\beta$ is driven by a different effective mixing angle:

$$\overset{(-)}{\nu}_\mu \rightarrow \overset{(-)}{\nu}_e : \sin^2\theta_{\mu e} \equiv 4|U_{e4}|^2|U_{\mu4}|^2 \,(\text{LSND, MiniBooNE anomalies}); \tag{2.3}$$

$$\overset{(-)}{\nu}_e \rightarrow \overset{(-)}{\nu}_e : \sin^2\theta_{ee} \equiv 4|U_{e4}|^2(1 - |U_{e4}|^2) \,(\text{Reactor, Gallium anomalies}); \tag{2.4}$$

$$\overset{(-)}{\nu}_\mu \rightarrow \overset{(-)}{\nu}_\mu : \sin^2\theta_{\mu\mu} \equiv 4|U_{\mu4}|^2(1 - |U_{\mu4}|^2) \,(\text{no anomaly observed}). \tag{2.5}$$

Like in the case of the three neutrino oscillations, the global fits for 3+1 short-baseline neutrino oscillations are performed with additional theoretical parameters related to the mixing between active and sterile neutrinos and with the observed anomalies being part of the experimental input. Results of such fits are briefly described in the next section and in Chapter 4, dedicated to the SBN physics programme.

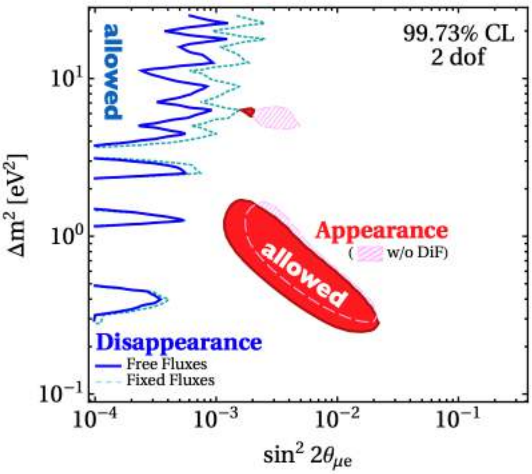

Figure 2.3: The global fit of the 3+1 model to the appearance versus disappearance datasets. The blue solid curves represent the limits from the disappearance datasets using free reactor fluxes while the blue dashed curves correspond to fixed reactor fluxes. The shaded contours are based on the appearance datasets. Figure from [92].

2.3 Global analysis

The oscillation amplitudes for the three channels shown in Equations 2.3 - 2.5 depend only on two mixing matrix elements: $|U_{e4}|$ and $|U_{\mu4}|$. Thus, the two parameters are overconstrained by experimental data spanning the three distinct channels. Several groups have performed global fits covering these channels and found similar allowed regions, with $\Delta m^2_{41} \sim 1$ eV^2. Global data from the ν_e disappearance channel favour sterile neutrino oscillations at the 3σ level with $\Delta m^2_{41} \approx 1.3$ eV^2 and $|U_{e4}| \approx 0.1$, even without any assumptions on predicted reactor fluxes. On the other hand, the anomalies in the ν_e appearance channel (dominated by LSND) are in strong tension with improved bounds on ν_μ disappearance, driven mainly by MINOS/MINOS+ [90] and IceCube [91]. As presented in Figure 2.3, no overlap between the parameter region favoured by appearance data (driven by LSND and MiniBooNE) and the strong exclusion limits from disappearance data, results in 4.7σ tension between disappearance and appearance datasets under eV sterile neutrino interpretation. This result was found to be robust to variations in the analysis and used data.

The overall global data do not appear to be consistent with the simple addition of a single sterile neutrino. Thus, the results from the next generation of experiments, like SBN, are of great importance for solving the puzzle of sterile neutrinos and clarifying the current picture of neutrino physics.

Chapter 3

Liquid Argon detection technique

Several innovative experiments dedicated to rare event physics, such as direct searches for dark matter or for neutrinoless double beta decay ($0\nu\beta\beta$), use liquefied noble gases, particularly liquid Argon (LAr) and liquid Xenon (LXe), as detection media. Among many advantages of noble liquids, from the detection point of view, the most relevant ones are high scintillation and ionisation yields, possible long drift paths of ionisation electrons and feasible large detector masses.

Due to the extremely low neutrino interaction cross sections, as pointed out in Section 1.2, huge detector masses are critical to enhance the neutrino interaction rate. LAr is sufficiently dense and much less expensive than LXe. Therefore, it is the only adequate noble liquid for huge detector volumes to study neutrino interactions and oscillations. In this chapter, the most important properties of LAr will be described in Section 3.1, followed by the two kinds of signal formation in a LAr TPC in Section 3.2. The LAr TPC construction and successful operation in neutrino studies will be then discussed in Sections 3.3 and 3.4, respectively using, as an example, the ICARUS detector operation in Gran Sasso laboratory.

3.1 Liquid Argon properties

Liquid Argon as a neutrino detection medium is a good choice for several reasons. First, LAr provides a dense target to increase the probability of neutrino interactions given the small cross-section of their interactions. Second, it renders relatively high stopping power for ionising radiation due to a relatively high energy loss per unit distance (dE/dx) within the detection medium. This improves the calorimetric capability of the detector. Additionally to its high ionisation yield, it also has a high scintillation light yield. Because the scintillation photons have energy lower than the first excited state of the Ar atom, the pure LAr is transparent to its own scintillation radiation. The main properties of Argon are summarised in Table 3.1.

Argon is the third most common gas in the Earth's atmosphere and, for that

Table 3.1: Liquid Argon chemical and physical properties [93, 94, 95, 96]. Since the light detection system is sensitive to visible light, some values are also given for the visible light due to the photo-fluorescent material absorbing LAr scintillation photons and emitting lower frequency photons. In this way, the LAr scintillation light is detected after shifting its wavelength to the visible spectrum.

LAr property	Value
Atomic number, mass	18, 40
Atomic weight	39.948 u
$\langle$ Z/A $\rangle$	0.45059
Concentration in air	0.934%
Normal boiling point	87.30 K
Density	1.396 g/cm^3
W$_{\mathrm{ion}}$ (1 MeV e$^-$)	23.6 eV
Energy loss $\langle$ dE/dx $\rangle$ (MIP)	2.105 MeV/cm
Electron mobility ($\lvert\mathbf{E}\rvert = 10^4$ V/m)	0.047 m$^2\cdot$ V$^{-1}\cdot$ s^{-1}
W$_{\mathrm{ph}}$ (1 MeV e$^-$)	19.5 eV
Scintillation light emission peak	128 nm (126 nm)
Photon yield scintillation (at 128 nm) 0-field	$\sim 4.0\times 10^4$ ph/MeV
Decay time constants	∼6 ns (23%) $\sim 1.6\mu$s (77%)
Radiation length	19.55 g/cm^2
Nuclear interaction length	117.2 g/cm^2
Dielectric constant at 128 nm (550 nm)	1.9 (1.5)
Refractive index at 128 nm (550 nm)	1.36 (1.23)
Rayleigh scattering length at 128 nm (550 nm)	0.99 m (10^3)

reason, can be easily obtained in large quantities by cryogenic fractional distillation of air. Pure LAr offers reasonably short radiation and nuclear interaction lengths; Argon atoms do not attach ionisation electrons, permitting long drift times. It also has high electron mobility, and the relative abundance and low cost of LAr make it a viable option for the construction of neutrino detectors at the few-ton scale up to the few-kiloton scale.

The exploitation of scintillation light, possibly combined with the collection of ionisation charge, makes the liquid Argon detectors a very attractive tool to identify and study charged particles, particularly in neutrino interactions.

3.2 Scintillation and ionisation signals

When a charged particle passes through the liquid Argon volume, two processes occur: ionisation and scintillation light emission. The average energy required to produce an electron-ion pair in Argon is $W_{\mathrm{ion}} = 23.6$ eV, whereas the average energy for an emitted scintillation photon is $W_{\mathrm{ph}} = 19.5$ eV. The emitted vacuum ultraviolet (VUV) scintillation light and the ionisation electrons produced by charged particles are used to detect and identify these particles.

The excited or ionised Argon atoms form excited Ar_2^* or ionised Ar_2^+ molecules (dimers) with other Argon atoms. The Ar_2^* excimer (excited dimer) decays radiatively:

$$Ar^* + Ar \rightarrow Ar_2^* \rightarrow 2Ar + \gamma, \tag{3.1}$$

while the Ar_2^+ state can recombine with an electron, falling into the Ar_2^* state, which decays radiatively:

$$Ar_2^+ + e^- \rightarrow Ar_2^* \rightarrow 2Ar + \gamma. \tag{3.2}$$

The recombination process occurs close to the particle trajectory, where free electrons and positively charged ions from the ionisation process are available in large quantities. The recombination reduces the ionisation electron signal causing a worse performance of the detector. To minimise this effect, the electrons have to be immediately driven to the readout (usually using anode wires). Therefore, a strong electric field is usually applied across the LAr volume between cathode and anode planes of the detector.

The wavelength of the scintillation light in LAr is usually cited as $\lambda = 128$ nm [95]. A more recent paper quotes instead $\lambda = 126$ nm [96]. To match better the emission spectrum to the response peak of photodetectors, a VUV-to-visible wavelength shifter is required. The most commonly used wavelength shifter for this application is tetraphenyl butadiene (TPB).

LAr scintillation light is characterised by two distinct decay times: fast (singlet eximer) and slow (triplet eximer). The mean lifetime of the singlet eximer state is 6 ns. The triplet eximer state has a significantly longer mean lifetime of 1.6 μs [97]. The decay time of the slow component rises with the increasing purity of Argon, so it can also be used to measure the purity. Highly electronegative contaminants, such as Oxygen and water within liquid Argon, can absorb emitted VUV photons, leading to a loss of light collection. In addition, impurities in LAr can also impede the drifting electrons or quench Argon excimers, leading to a loss of both light and charge collection. Thus, the efficient purification system of LAr is essential.

The scintillation light emission and the ionisation processes are complementary, and their relative yields depend on particle energy and how strong the applied electric field is. The increase of the electric field reduces the effect of recombination. Thus, the free-electron yield due to ionisation increases with a field value, while the photon yield due to scintillation decreases. However, for both processes, saturation occurs for fields higher than ~10 kV/cm.

3.3 Liquid Argon time projection chamber

LAr TPCs are based on a large volume filled with LAr with a constant electric field ($\overrightarrow{E}$) applied across this volume between the anode and the cathode. Figure 3.1 summarises the signal formations described above and how the electric field handles them in a simplified schematic of the LAr TPC.

At the typical electric field value of 500 V/cm and temperature of 87 K the electron drift velocity is 1.55 m/ms [98].

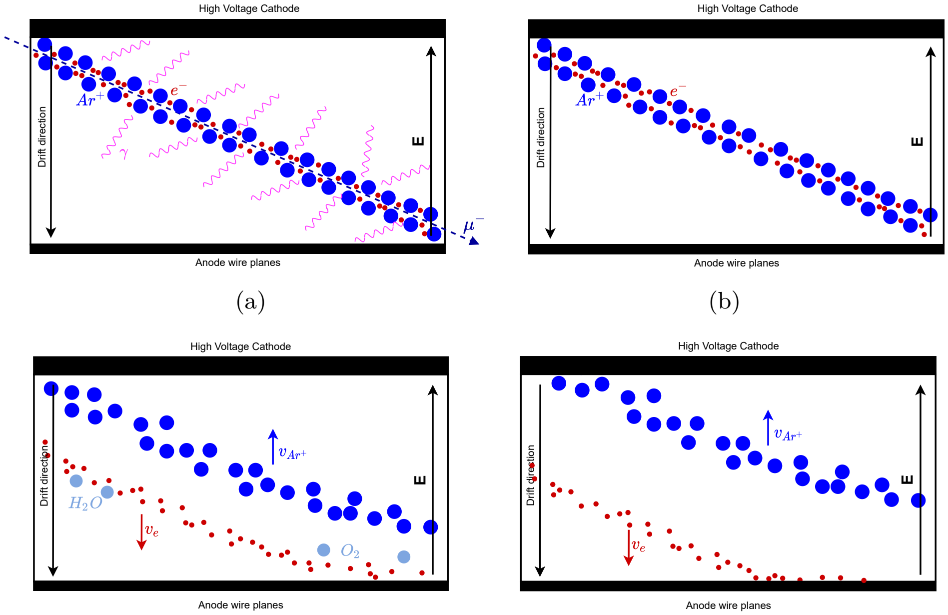

(a)

(b)

(c)

(d)

Figure 3.1: The working principle of a LAr TPC. A muon passes through the LAr detector volume and produces an ionisation track of Ar$^+$ and e$^-$ pairs, and induces the emission of VUV scintillation light (a). A fraction of the Ar$^+$ and e$^-$ pairs recombine to emit additional scintillation light; the remaining pairs are separated by the electric field (b). The Ar$^+$ ions drift towards the high voltage cathode, and the electrons drift towards the anode wire planes; drifting electrons may attach to negatively charged impurities, diminishing signal integrity (c). The drifting electrons produce signals at the anode wire planes, which are amplified and read out (d).

In LAr TPC detectors, the slow signal (typically about 1 ms) from ionisation electrons combined with the fast scintillation signal (order of ns) allows a precise 3D reconstruction of the charged particle paths.

The concept of LAr TPC for neutrino studies was developed by C. Rubbia in 1977 [99]. The ICARUS T600 detector was the first full-size LAr TPC used for studying neutrinos. Since the work for this detector in the framework of the SBN program is the subject of this thesis, it will be used to present principles of the LAr TPC construction and functionality. The detailed presentation of the ICARUS T600 detector can be found in Ref. [100]. Its schematic picture is shown in Figure 3.2.

The detector consists of two identical, adjacent T300 modules. The modules are aluminium cuboids with internal dimensions of 3.6 m × 3.9 m × 19.6 m externally surrounded by thermal insulation layers each. Each T300 module houses an inner detector composed of two TPCs with a common cathode. Each TPC is equipped with an anode, a field-shaping system, monitors, probes, and scintillation light detectors.

Each TPC anode consists of three parallel wire planes with a 3 mm spacing between neighbouring planes and a 3 mm wire pitch. The total number of wires and electronic channels in the T600 detector is 53,248.

For each TPC, the wires in three anode planes are mounted at 0°, +60° and -60° with respect to the long edge of the T300 modules. They are biased so that the first two planes work in an induction mode and the ionisation electrons pass them almost unaffected. The third plane works in a collection mode, i.e., the ionisation electrons are collected by its wires.

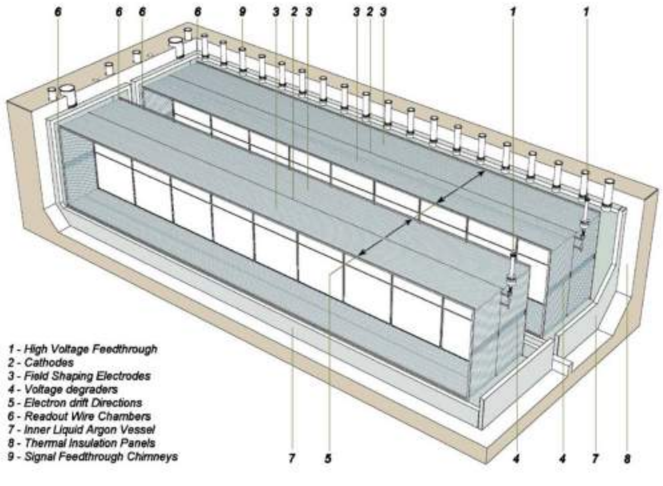

Figure 3.2: Schematic layout of the T600 detector. Figure from [100].

In the centre of each T300 module, the cathode plane is mounted at a distance of 1.5 m from the wires on each side. This distance represents the maximum drift path of ionisation electrons. At the nominal voltage of 75 kV, which corresponds to an electric field of 500 V/cm, the maximum drift time in LAr is about 1 ms. As a result, projective views of the same event for all three wire planes with one coordinate related to the wires and the second one related to the drift time are obtained, as shown in Figure 3.3. After the 3D reconstruction based on the three projective views, one obtains precise spatial imaging of events registered in the detector fiducial volume. One also obtains very good calorimetric measurements based on the charge collected by the third wire plane, for example the ICARUS detector has a 3% electromagnetic energy resolution at 1 GeV energy deposit (scaling to other energies as the inverse square root of the deposit).

The scintillation light detection system of the ICARUS detector, being of special interest to this thesis, will be presented in detail in Chapter 6.

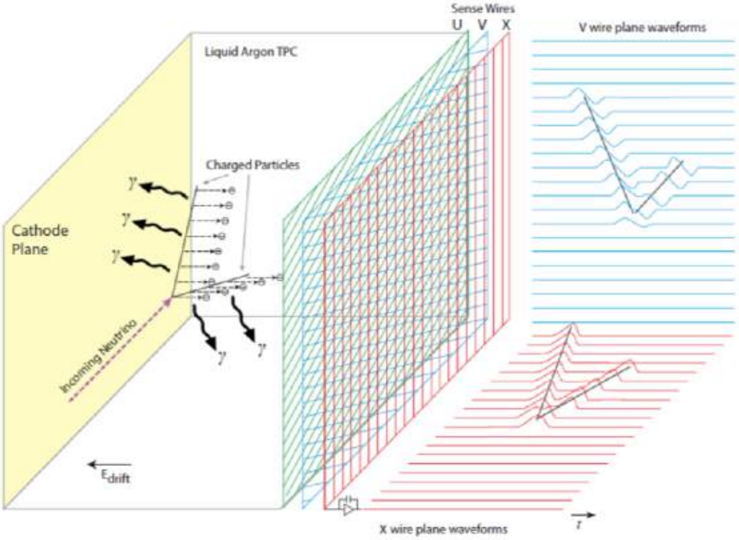

Figure 3.3: Schematic picture of charged particles emerging from a neutrino interaction vertex and producing ionisation tracks and scintillation light. The light propagates to an array of photomultiplier tubes (not shown in this figure), with the flash providing the time of the event. Waveforms of signals read out from the wires after processing are used to reconstruct the 3D trajectories of the charged particles together with their deposited energy. Figure from [101].

3.4 ICARUS experiment in the underground Gran Sasso laboratory

The first neutrino experiment using LAr TPC detector technology on a large scale was the Imaging Cosmic and Rare Underground Signals (ICARUS) experiment using the T600 detector, as presented in Section 3.3. The detector was located in the Gran Sasso laboratory under 2400 meters of rock, which offered efficient shielding from cosmic-ray induced background.

The ICARUS experiment belonged to the European programme of neutrino oscillation studies at the CNGS (CERN Neutrinos to Gran Sasso) beam, approved in 1998. The CNGS ν_μ beam was produced at CERN and directed towards the Laboratori Nazionali del Gran Sasso (LNGS), 732 km away. The CNGS neutrino facility provided an almost pure ν_μ beam with a broad maximum in the energy range $10 \leq E_\nu \leq 30$ GeV, with a contamination from muon anti-neutrino of about 2% and an electron neutrino component of less than 1% [102]. A short description of the production of accelerator neutrino beams is given in Section 4.2.

The main goal of the CNGS scientific programme was the direct observation of the ν_τ CC interactions from ν_τ appearing in the ν_μ beam on the way from CERN to Gran Sasso due to the $\nu_\mu \leftrightarrow \nu_\tau$ oscillations. Although the disappearance of the atmospheric ν_μs, discovered in the Super Kamiokande experiment, was interpreted this way, a direct proof with a sufficient statistical significance was not possible for the water Chenerknov Super Kamiokande detector. The direct observation of the ν_τ CC interactions required the identification of the charged τ lepton in the final state of the ν_τ CC interactions - experimentally a very demanding challenge.

The OPERA (Oscillation Project with Emulsion-tRacking Apparatus) experiment, equipped with almost 2 ktons of emulsion chambers, was specially designed for this purpose and discovered the ν_τ appearance in the CNGS beam [103].

The ICARUS T600 detector had operated at Gran Sasso in 2010 - 2013, taking both the CNGS neutrino beam and atmospheric data with high Argon purity and good detector stability. From 2010 to 2012, the detector had collected neutrinos corresponding to a total of 8.6×10^{19} 400 GeV protons-on-target with a recording efficiency exceeding 93%.

The ICARUS approach to the $\nu_\mu \leftrightarrow \nu_\tau$ oscillation studies was to separate the ν_τ CC events from the background through kinematical criteria and very characteristic electromagnetic showers for electrons, with some of them coming from the τ lepton decays. However, there was no conclusive result concerning the $\nu_\mu \leftrightarrow \nu_\tau$ oscillations, primarily due to the too-small detector mass and too short data taking period. Despite the failure concerning the observation of the ν_τ appearance in the CNGS beam, the ICARUS experiment obtained valuable physics results.

The most important of them was related to the 2011 announcement of the observation of *superluminal* neutrinos by the OPERA experiment [104]. The ICARUS collaboration published the article [105] in which it was indicated that the energy distribution of the neutrinos is not compatible with *superluminal* particles. In 2012 ICARUS directly measured the neutrino velocity [106, 107], which was in agreement with the speed of light and the theory of special relativity. For the final analysis, 25 neutrino events were selected, yielding an upper limit for the difference between the neutrino and the light time of flight:

$$\delta \mathrm{t} = 0.18 \pm 0.69(\mathrm{stat.}) \pm 2.17(\mathrm{sys.})\ \mathrm{ns}, \tag{3.3}$$

corresponding to:

$$\frac{v-c}{c} = (0.7 \pm 2.8(\mathrm{stat.}) \pm 8.9(\mathrm{sys.})) \times 10^{-7} \tag{3.4}$$

In 2014 the ICARUS T600 detector was moved to CERN for overhauling. In April 2017, the upgraded detector was transported from CERN to the FNAL near Chicago in the US and put again in operation at the Booster Neutrino Beam (BNB) for a definitive clarification concerning the existence of a new sterile neutrino state (ν_s) suggested by the LSND and MiniBooNE observations.

The successful operation of the ICARUS T600 detector at Gran Sasso opened the way to the construction of more advanced detectors and with larger detector masses up to tens of ktons as required to realise the next generation experiments for neutrino oscillation studies and searches for proton decays.

Chapter 4

Short Baseline Neutrino program at Fermilab

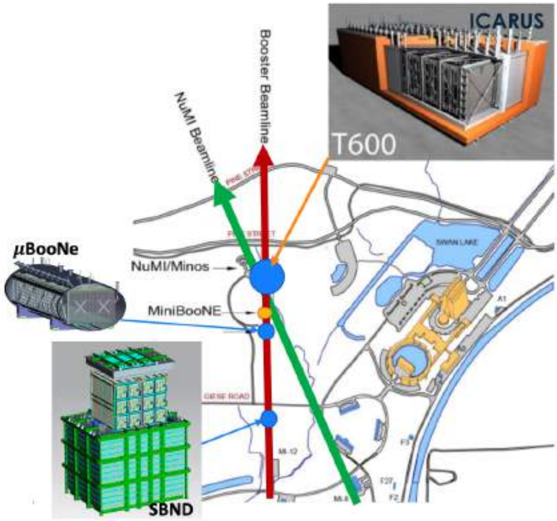

Figure 4.1: Layout of the three LAr TPCs of the SBN program and their positions at the BNB line. Figure reproduced from [108].

The Short Baseline Neutrino (SBN) program aims to study neutrino oscillations and interactions in the hundreds-of-MeV to a few GeV energy range, using the Booster Neutrino Beam (BNB) at Fermilab in the US. It will make use of three detectors, all being LAr TPCs, exposed to the muon neutrino and antineutrino beams with peak energy of ∼0.8 GeV [109]. They are located on the beam axis at different distances from the target - Short Baseline Near Detector (SBND) at 110 m, MicroBooNE at

470 m and ICARUS at 600 m, as shown in Figure 4.1.

The main purposes of the SBN program are searches for the LSND-like sterile neutrino oscillations with the full coverage of relevant values of the $\Delta m^2 \sim eV^2$ oscillation parameter, investigating the MiniBooNE additional low energy anomalies and making precision measurements of neutrino interactions with Argon.

In SBN, the measurements of the beam before oscillations will be done in the SBND detector while the measurements of any potential ν_e ($\bar{\nu}_e$) appearance and ν_μ ($\bar{\nu}_\mu$) disappearance will be studied in the MicroBooNE and ICARUS detectors.

The MicroBooNE started data taking in 2015, the ICARUS detector became operational in 2020, and the SBND detector is expected to be commissioned in 2023. Once the SBND and ICARUS detectors are fully operational, the role of the MicroBooNE detector will become marginal.

It is worth mentioning that the MicroBooNE and ICARUS detectors also register some off-axis neutrinos from the NuMI (Neutrinos at the Main Injector) beam, which is dedicated to studies of neutrino oscillations in the NOνA experiment.

In the following sections, brief descriptions of the SBN physics programme, the SBN three detectors and the initial results of the MicroBooNE physics analyses are presented. They are based on several publications, but the SBN proposal [110] and the more recent review article dedicated to the SBN [111] are the primary references.

4.1 SBN physics programme

The SBN physics programme, based on extensive simulation studies, has been presented in the SBN proposal [110]. The applied advanced simulation tools included a robust simulation of the BNB beam developed by the MiniBooNE collaboration [109], the neutrino interaction event generator (GENIE) and built-in systematic error machinery [112, 113], and the physics model simulators like the GEANT4 [114] simulation toolkit. Correlations in neutrino flux and ν-Ar interaction models were quantified using these tools and applied to sensitivity analysis.

The SBN will search for short-baseline oscillations covering the entire allowed region of the sterile neutrino oscillation phase space, including all experimental hints for sterile neutrinos, with better than 3σ significance. With the most significant contribution to the allowed phase space coming from the LSND/MiniBooNE ν_e appearance anomaly, SBN should cover the entire LSND/MiniBooNE region with 5σ significance. Furthermore, SBN should perform the search in both ν_e appearance ($\nu_\mu \to \nu_e$) and ν_μ disappearance ($\nu_\mu \to \nu_x$) channels.

The ability to establish that an oscillation signal was observed is directly impacted by the size of the systematic uncertainties. One of the strengths of the SBN program is the inclusion of three functionally similar detectors that are composed of the same target nucleus (Argon) and observe the same flux of neutrinos. Many of the systematic uncertainties which affect the oscillation analysis will be highly correlated between the three detectors.

To evaluate systematic uncertainties, a multi-universe method is utilised. This method works by creating a large number of event weights that can be used to scale the event distributions based on correlated random fluctuations of the uncertainties. The uncertainties related to the cross-section models were studied with the GENIE re-weighting package [113].

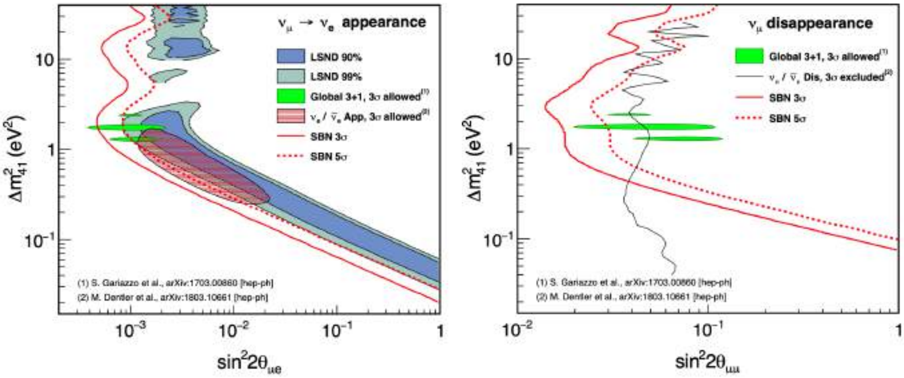

(a) The $\nu_\mu \to \nu_\mathrm{e}$ appearance channel. (b) The $\nu_\mu \to \nu_\mu$ disappearance channel.

Figure 4.2: SBN 3σ (solid red line) and 5σ (dotted red line) sensitivities to a light sterile neutrino in the $\nu_\mu \to \nu_\mathrm{e}$ appearance channel (4.2a) and $\nu_\mu \to \nu_\mu$ disappearance channel (4.2b). Figure from [111].

Figure 4.2 illustrates the projected sensitivities to ν_e appearance and ν_μ disappearance oscillation signals. The analysis presents the 3+1 sterile neutrino scenario according to Equations 2.3 and 2.5 (see Chapter 2). The event rates, systematic uncertainties with their respective correlations based on the complete simulation of the beam, and physics processes are described in detail in the SBN proposal [110]. An uncorrelated detector systematic uncertainty at the level of 3% is assumed. Statistical errors are derived considering an exposure of 6.6×10^{20} protons delivered to the BNB target, which corresponds to approximately three years of operation for both the SBND and the ICARUS detectors.

Figure 4.2 presents how SBN sensitivity compares to the two data sets independently, the preferred regions for all $\nu_\mu \to \nu_\mathrm{e}$ appearance data alone (left plot, shaded red) and the limit imposed by all ν_μ disappearance data alone (right plot, solid black line) at 3σ CL [92]. The SBN program alone may disqualify almost all the global appearance preferred region at 5σ. Moreover, the expected sensitivity on the ν_μ disappearance channel is better than the global constraint for an extensive range of Δm^2_{41}. The 5σ coverage of the parameter region relevant to the LSND/MiniBooNE anomaly can be achieved in 3 years of 6.6×10^{20} POT data collection. The 3σ

allowed parameter regions are displayed as the shaded green regions in both plots of Figure 4.2. One sees that Δm^2_{41} is tightly constrained around 1 - 2.5 eV^2 to satisfy all data. The severe tension between datasets (see Section 2.3) is demonstrated as the stretching of the allowed regions in mixing strength. Note that the preferred values of $\sin^2 2\theta_{\mu\mu}$ are necessarily accompanied by non-zero values of $\sin^2 2\theta_{ee}$ due to non-zero $\sin^2 2\theta_{\mu e}$, according to Equations 2.3, 2.4, 2.5.

Moreover, Ref. [115] is suggesting the complementarity of the reactor neutrino experiments and SBN. Figure 4.2 shows that SBN has its best sensitivity in the regions of remaining allowed parameter space in both channels. Thus, the SBN is primed to rule on the possibility of sterile neutrinos.

Not limited to the sterile neutrino puzzle, SBN has an extensive range of physics goals that include detailed, high-statistics studies of neutrino-Ar nucleus interactions, with significant importance for the DUNE experiment in the future.

Neutrino-nucleus interactions are critical to understanding neutrino oscillation experiments [116, 117]. The SBN will collect high statistics of neutrino event samples and perform the world's highest statistics cross-section measurements for many ν-Ar scattering processes using the well-characterised neutrino fluxes of the BNB [109].

In particular, the SBND detector observing the largest flux of neutrinos of the three detectors gives an ideal venue to perform precision studies of the physics of ν-Ar interactions in the GeV energy range (more than 2 million neutrino interactions per year in the full active volume with 1.5 million ν_μ CC events, assuming 2.2×10^{20} POT). Apart from the large number of ν_μ events, it will also collect about 12,000 ν_e events per year, allowing for both inclusive and exclusive measurements of electron neutrino interactions. The near detector will also make many high precision exclusive measurements of the different final states for ν_μ and ν_e interactions, including rare interaction channels. SBND will measure nuclear effects to make a comparison with different Monte Carlo simulation generators and to improve them.

Moreover, MicroBooNE and ICARUS detectors can also study ν-Ar cross sections exploiting the off-axis NuMI beam. ICARUS will observe high statistics of neutrino events in the 0 - 3 GeV energy range with an enriched electron neutrino component ($\sim$5%). Muon neutrino event rates at the ICARUS detector from the NuMI beam are comparable with those from the BNB. In contrast, the electron neutrino component is enhanced by orders of magnitude in the off-axis beam from the prevailing decay of secondary kaons ($K^\pm \rightarrow \pi^0 + e^\pm + \overset{(-)}{\nu}_e$). ICARUS will see about 350,000 ν_μ events and 16,000 ν_e events per year from the NuMI off-axis.

The total SBN data can change the current understanding of the neutrino-nucleus scattering, becoming the key input to improving the modelling of ν-Ar interactions before the start-up of the DUNE long-baseline neutrino experiment.

Finally, the SBN represents a valuable opportunity for the large international community to develop the challenging techniques necessary to extract physics information from LAr TPC data.

4.2 Neutrino beams at Fermilab

The neutrino BNB and NuMI beams are produced at the Fermilab accelerator complex, depicted in Figure 4.3. This complex consists of the beam source, the linear accelerator (Linac), the Booster, the Recycler and the Main Injector. The three accelerators produce two primary proton beams, a low energy (8 GeV) proton beam from the Booster and a high energy (120 GeV) beam from the Main Injector (MI).

4.2.1 Primary proton beams

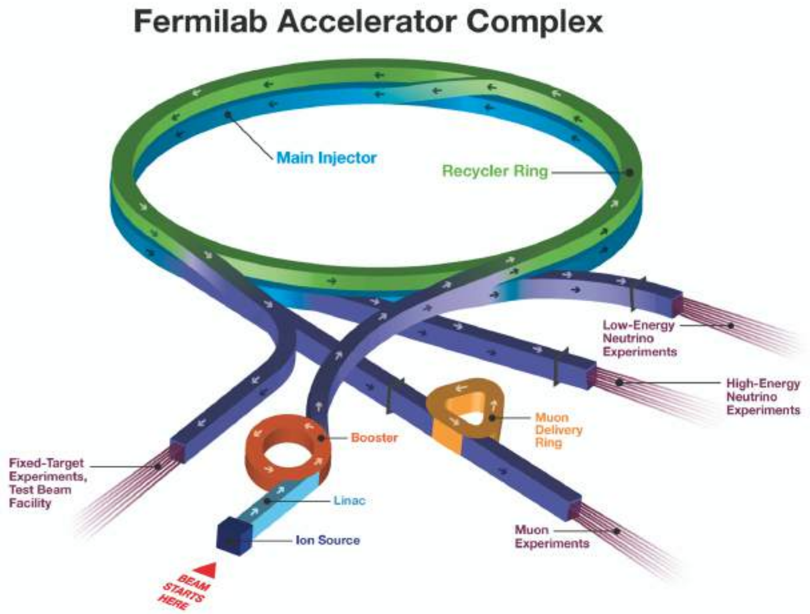

Figure 4.3: The Fermilab accelerator complex. The H^- ions from the ion source are fed to the Linac accelerator, where a carbon foil at the end of it transforms them into a H^+ (proton) beam. The particles are successively accelerated in the Linac (400 MeV), Booster (8 GeV), and the Main Injector (120 GeV). The Recycler is a staging area that combines batches of protons from the Booster before their transition to the MI. Protons from the Booster and from Main Injector are directed toward targets to form two neutrino beams, the low energy BNB beam and the high energy NuMI beam. The MI can also send particles to the test beam facilities and the muon experiments. Figure from [118].

The beam preparation starts at the Fermilab pre-accelerator which contains two H_2 beam sources. Hydrogen gas is ionised by means of a high-voltage arc. A cone-shaped electrode subsequently extracts H^- ions from the plasma, accelerating them to 35 keV. The beam is subsequently *chopped* using an Einzel lens which periodically interrupts the beam in order to transform the continuous stream into a pulsed 100 μs-wide structure at 15 Hz that can match the requirements of the radio frequency (RF) quadrupole cavities used for further acceleration to 750 keV. Then the Linac accelerator accelerates the H^- ions from 750 keV to 400 MeV via two series of RF cavities to inject them into the Booster accelerator. The 400 MeV beam is steered towards the Booster in a 2.2 μs-wide time interval, which corresponds to the revolution period of the protons inside the Booster (at 400 MeV). After arriving at the Booster, the H^- ions are filtered through a stripping foil that removes the electrons from the ions, producing a proton beam.

At this point, the proton beam can go through a *paraphasing* process, which captures the continuous beam into RF bunches. This step is necessary because, at injection, the proton beam is *unbunched* and has a continuous structure hence cannot be accelerated. During the paraphasing process, the RF cavities accelerate some protons and decelerate others to divide them into 84 bunches.

The set of aligned 84 bunches is referred to as a batch. After alignment, the resonant frequency of the cavities increase from 37.8 to 52.8 MHz to accelerate the protons. This corresponds to the increase of the energy of the beam from 400 MeV at injection to 8 GeV at extraction. As the energy increases, the revolution period decreases from 2.2 μs to 1.6 μs. Kicker magnets provide a fast-acting field that can deflect the beam for extraction. Although small, the ramp-up time of the magnet is non-zero. Extracting protons during ramp-up time would cause the extracted beam to be sprayed instead of being collimated. Thus, a segment of the batch where three contiguous bunches should be is left empty, bringing down the total number of delivered bunches from 84 to 81. The empty segment provides the kicker magnet enough time to ramp up to the full-field intensity and to send the beam off to the target.

The Booster beam line delivers a $\sim$1.6 μs-wide proton batches with a 15 Hz repetition rate to a beryllium target to produce Booster Neutrino Beam (BNB) and to the Recycler to produce Neutrinos at Main Injector (NuMI) beam. The 81 bunches that comprise the BNB batch have a $\sim$2 ns-wide Gaussian profile with a $\sim$18.8 ns spacing between them.

An important term used to describe a proton beam is *spill*. Spill refers to the timing structure of the extraction beam. In general, multiple batches can be part of a spill. Since protons for the BNB are extracted directly from the Booster, the timing structure of the spill matches the batch timing structure (spill = batch = 1.6 μs), and the two terms can be used interchangeably. Figure 4.4 shows the timing structure of a BNB spill.

The 8 GeV proton beam from the Booster also serves as an input to the Main

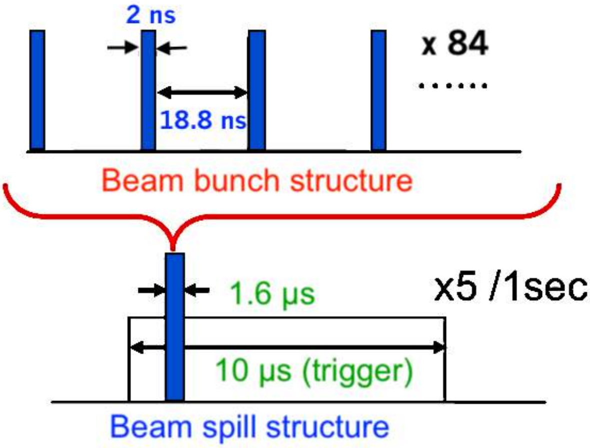

Figure 4.4: Booster Neutrino Beam spill structure.

Injector, which accelerates this beam to 120 GeV. The Recycler located on top of the Main Injector facilitates the proton injection from the Booster to the MI and performs slip-stacking [119]. In this process, pairs of batches are injected into the Recycler and then merged to form double-intensity batches. The Recycler can slip-stack up to 12 batches, which results in six double-intensity batches for extraction to MI. With this 6+6 slip-stacking, the Main Injector can deliver $\sim 6 \times 10^{13}$ protons to the NuMI target in 9.5 μs spills, at an average of 1.33 s. In Figure 4.5 the time structure of the two neutrino beams is presented. The Booster accelerator generates 20 proton spills in 1.33 s (15 Hz). 12 of these spills are stacked, further accelerated in the Main Injector and sent to the NuMI target, while the remaining 8 spills are sent to the BNB target. In summary, the protons from the Main Injector are sent to the NuMI beam every 1.33 s (1 spill/1.33 s = 0.75 Hz). After that, a total of 8 Booster spills impinges on the BNB target every 1.33 s (8 spills/1.33 s = 6 Hz), and since in total, the Booster generates 20 spills in 1.33 s, this results in one BNB spill every 66 ms.

4.2.2 Production of neutrinos

The neutrino beam intensity depends on the number of delivered protons described by the unit called POT (Protons On Target). When the protons hit the target, many charged secondary short-lived particles, mainly pions, are produced. Kaons are less frequent, but cannot be neglected in the process of neutrino beam production.

The target is located within magnetic focusing devices, consisting of a set of two

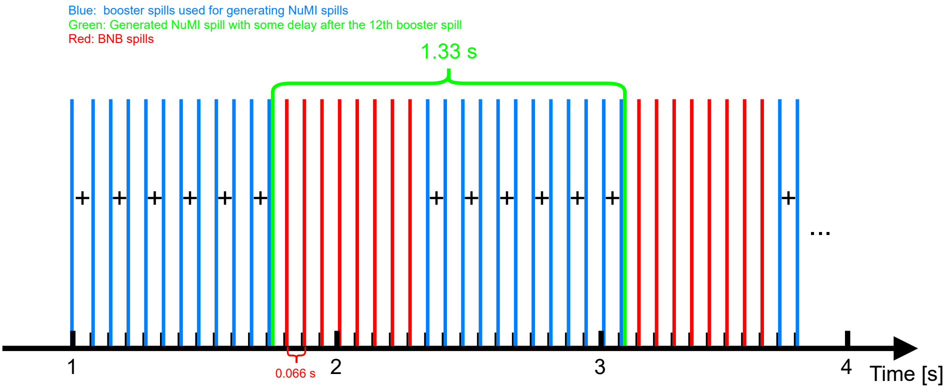

Figure 4.5: BNB and NuMI beams time structures.

cylindrically symmetric magnets, called horn and reflector, to provide a magnetic field. The magnet focusing horn selects positively or negatively charged mesons by choosing the direction of the magnetic field. The mesons of the selected charge are focused on a decay tunnel, while the opposite charge mesons are defocused, but a small fraction of them also enters the tunnel. The decay tunnel is usually a steel pipe where most of the mesons decay into muon neutrinos (for positively charged mesons) or into muon antineutrinos (for negatively charged mesons), accordingly to their lifetimes ($\tau_\pi = 2.6 \times 10^{-8}$ s, $\tau_{K^\pm} = 1.2 \times 10^{-8}$ s):

$$\pi^+ \rightarrow \mu^+ + \nu_\mu \text{ branching ratio} \approx 100\%, \tag{4.1}$$

$$\pi^- \rightarrow \mu^- + \bar{\nu}_\mu, \tag{4.2}$$

$$\mathrm{K}^+ \rightarrow \mu^+ + \nu_\mu \text{ branching ratio} \approx 63.5\%, \tag{4.3}$$

$$\mathrm{K}^- \rightarrow \mu^- + \bar{\nu}_\mu. \tag{4.4}$$

Muon neutrinos or antineutrinos are propagating in almost the same direction as mesons, forming a muon neutrino or antineutrino beam. The muons from pion decays are also unstable and decay into lighter leptons:

$$\mu^+ \rightarrow \mathrm{e}^+ \nu_\mathrm{e} \bar{\nu}_\mu, \tag{4.5}$$

$$\mu^- \rightarrow \mathrm{e}^- \bar{\nu}_\mathrm{e} \nu_\mu. \tag{4.6}$$

Thus, ν_e and $\bar{\nu}_\mu$ from μ^+ decays contaminate the muon neutrino beam from π^+ and K^+ decays, while $\bar{\nu}_\mathrm{e}$ and ν_μ from μ^- decays contaminate the muon antineutrino beam from π^- and K^- decays. It is very important to keep these contaminations as low as possible because they introduce systematic uncertainties in the neutrino oscillation measurements ($\bar{\nu}_\mu$ contamination in the measurement of disappearance of ν_μ and, what is even more important, ν_e contamination is the main background in the measurement of appearance of ν_e). Fortunately, the muon lifetime $\tau_\mu = 2.2 \times 10^{-6}$ s is by two orders of magnitude longer than the lifetimes of charged pions and kaons, so it is possible to optimise the length of decay tunnel in such a way that most of pions decay inside tunnel while most of muons survive and are then absorbed by concrete and rock behind the tunnel.

Two other sources of the muon neutrino (antineutrino) beam contamination have to be taken into account. The first one is due to the presence of opposite charge pions among the pions of a selected charge, entering the decay tunnel. Their decays increase the $\bar{\nu}_\mu$ (ν_μ) contamination of the ν_μ ($\bar{\nu}_\mu$) beam and through the subsequent muon decays introduce a small $\bar{\nu}_\mathrm{e}$ contamination (ν_e) of the ν_μ ($\bar{\nu}_\mu$) beam. The second source, this time of only the ν_e contamination of the muon neutrino beam ($\bar{\nu}_\mathrm{e}$ contamination of the muon antineutrino beam), is the relatively rare (branching ratio ~4.8%) decay of K^+ (K^-):

$$\mathrm{K}^+ \rightarrow \pi^0 \mathrm{e} + \nu_\mathrm{e}, \tag{4.7}$$

$$\mathrm{K}^- \rightarrow \pi^0 \mathrm{e} - \bar{\nu}_\mathrm{e}. \tag{4.8}$$

The produced neutrino beam is dominantly composed of ν_μ ($\bar{\nu}_\mu$) if positively (negatively) charged mesons are chosen and focused. The ν_μ beam contamination by $\bar{\nu}_\mu$ is typically 1 - 7%, by ν_e is usually $< 1\%$ and by $\bar{\nu}_\mathrm{e}$ is usually $< 0.1\%$. As was already mentioned, the ν_e intrinsic beam contamination has to be well-known for the studies o the $\nu_\mu \leftrightarrow \nu_\mathrm{e}$ oscillations. For low energy beam the ν_e contamination is mostly due to muon decays, while the kaon decays become more important at higher energies. For example, at 4.5 GeV proton energy 10% of the total ν_e contamination comes from kaon decays.

Apart from the lifetimes of pions and muons defined for these particles at rest, the dependence of the pion decay length on the pion energy has to be taken into account in the decay tunnel optimisation. This means that the higher energy pions require a longer decay tunnel while pions with lower energy require a shorter one.

At the end of the decay tunnel, muons are usually measured using dedicated muon monitors, which indirectly provide information about the directions of the neutrinos.

4.2.3 Booster Neutrino Beam

The Booster Neutrino Beam line is depicted schematically in Figure 4.6. The 8 GeV kinetic energy (8.89 GeV/c momentum) protons from the Booster accelerator are directed towards a beryllium (Be) target to produce secondary particles, mostly mesons, in p-Be interactions. The horn is a single toroid made of aluminium alloy that surrounds the target and it is supplied with 174 kA in 143 μs pulses coincident with proton delivery. Depending on the polarity of the horn, either positive charge mesons are focused, and negatively charged ones are defocused (neutrino mode) or vice versa (antineutrino mode).

Focused secondaries propagate down a 50 m long, 0.91 m radius air-filled tunnel, where the majority of them decay, following Equations 4.1 and 4.2, to produce positively charged muons and neutrinos or negatively charged muons and antineutrinos. Most of the muons are absorbed into a concrete and steel absorber at the end of the decay tunnel.

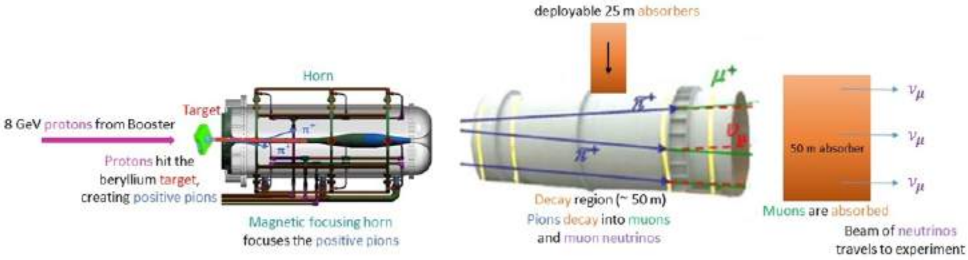

Figure 4.6: Schematic representation of neutrino production at the Booster Neutrino Beam. Figure from [109].

The timing structure of the delivered proton beam is shown in Figure 4.4 and as described in Section 4.2.1 the Booster spill length is 1.6 μs with nominally $\sim 5 \times 10^{12}$ POT. The BNB is very well understood because it has already operated for several years in neutrino and antineutrino modes. Systematic uncertainties associated with the beam have also been characterised in a straightforward way with a total error of 9% at the peak of the ν_μ flux and larger in the low and high energy regions, as reported in Ref. [109, 120]. As illustrated in Figure 4.7a, the composition of the flux in neutrino mode (focusing positive pions) is energy dependent, but is dominated by the ν_μ signal (93.6%), followed by the $\bar{\nu}_\mu$ contamination (5.9%) and the $\nu_e/\bar{\nu}_e$ contamination at the level of 0.5% at energies below 1.5 GeV. In antineutrino mode, the flux contributions are 83.7% (signal), 15.7%, 0.2%, and 0.4%, for $\bar{\nu}_\mu$, ν_μ, ν_e and $\bar{\nu}_\mathrm{e}$, respectively (Figure 4.7b).

4.2.4 Neutrinos at the Main Injector beam

The primary user of the NuMI beam is the NOνA experiment, receiving the beam at a small off-axis angle (14 mrad). The beam is well-understood for NOνA, and, since a full characterisation is still ongoing for ICARUS, the main beam characteristics presented in this section follow the settings for the NOνA experiment. Nevertheless,

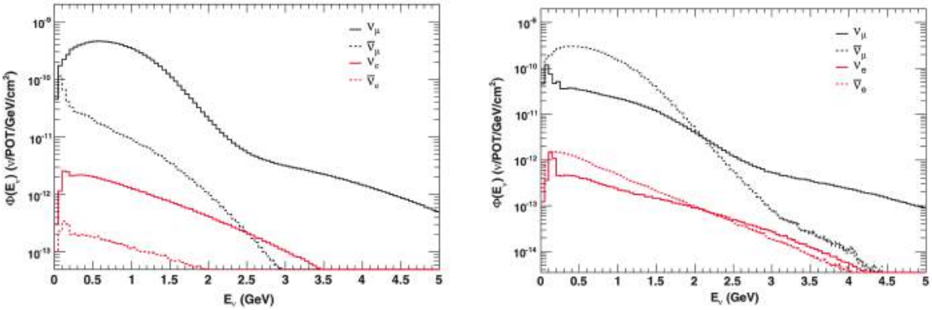

(a) The horn in neutrino mode.

(b) The horn in antineutrino mode

Figure 4.7: BNB flux contributions by neutrino species predicted at the MiniBooNE detector in the neutrino (4.7a) and antineutrino (4.7b) modes. Figure from [109].

for the case of ICARUS, additional considerations related to the exposure at a large off-axis angle are presented in Section 9.1.1.

The scheme of the NuMI beam line is illustrated in Figure 4.8. The NuMI beam is produced by a high energy (120 GeV) primary proton beam, extracted from the Main Injector. Before colliding with the target, the beam passes through a specially designed device made up of graphite, referred to as the baffle. The protons are incident on the narrow graphite target approximately 1 m in length through the collimating baffle. The produced short-lived particles, mostly mesons, are then focused in the forward direction and charge-sign-selected by two magnetic horns (Horn 1, Horn 2) and then enter a 675 m long decay pipe. When the horns are in neutrino mode (antineutrino mode), the beam of mesons is largely formed by π^+ (π^-) with energies of around 10 GeV. A tertiary beam of neutrinos is produced following Equation 4.1.

The decay pipe dimensions (2 m wide and 675 m long) were calculated to closely match the decay length of 10 GeV pions.

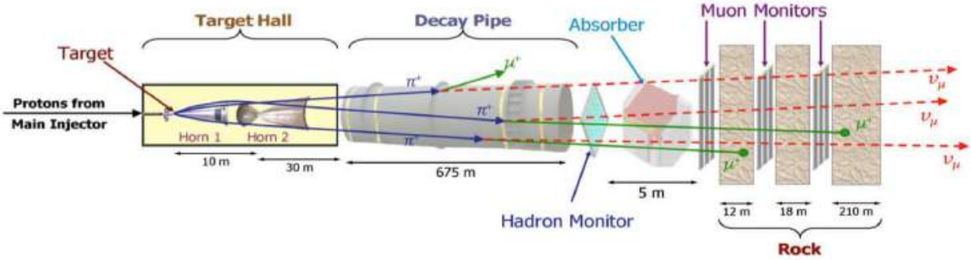

Figure 4.8: Neutrino production at the NuMI beam. Figure from [121].

The majority of the μ^+ daughters of the π^+'s survive to the end of the decay region and are then absorbed by the rock. The contamination of ν_μ beam due to opposite polarity pions and muon decays inside the decay tunnel are $\sim$5% for $\bar{\nu}_\mu$ and $\sim$1% for ν_e and $\bar{\nu}_e$ [122].

4.3 Detectors overview

4.3.1 SBN Near detector: SBND

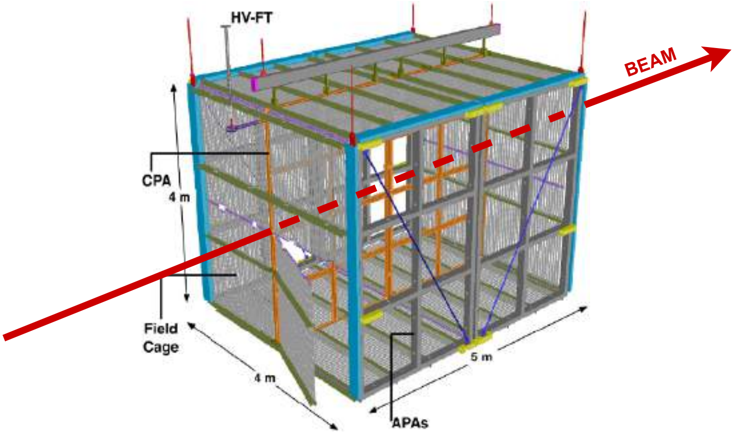

Figure 4.9: A schematic drawing of the SBND detector and its elements. Figure from [123].

The SBND detector is schematically presented in Figure 4.9. It will be a modular LAr TPC with a central Cathode Plane Assembly (CPA) and four Anode Plane Assemblies (APAs) to read out ionisation electron signals. The total number of readout channels is 2,816 per APA (11,264 in the entire detector). The TPC active volume is 4.0 m wide, 4.0 m high and 5.0 m long and it will contain 112 tons of liquid Argon. The CPA will be biased at -100 kV, and four Field Cage Assemblies (FCAs) around the TPC will maintain a constant electric field of 500 V/cm. The SBND light collection system will be based on 120 8” Hamamatsu R5912-mod PMTs mounted behind the TPC wire planes. For LAr scintillation light detection, 96 PMTs will be coated by wavelength-shifting material Tetraphenyl Butadiene (TPB), and 24 will be left uncoated for observing visible light. The light collection system will also use the ARAPUCA [124] (and X-ARAPUCA [125]) photon trap and light guiding bars equipped with silicon photomultipliers (SiPMs). In order to improve uniformity and light collection efficiency in the SBND volume, TPB-covered reflector foils will be placed on its cathode plane. The HV compatibility tests of applying the foils on the cathode are described in Chapter 8.

The TPC will be housed in a membrane cryostat, maintaining the LAr temperature of 87 K and allowing LAr recirculation and purification at a constant rate. The cryostat will be almost entirely surrounded by a solid scintillator-based Cosmic Ray Tagging (CRT) system to help reject cosmic background events.

The SBND detector construction is well on its way with all the components being ready for assembly and installation. The detector commissioning should start in 2023. Once ready, the detector will provide an accurate flux estimate before oscillation and a crucial sample of neutrino interactions for cross-section measurements on Argon and for studying neutrino-nucleus interaction modelling. SBND will observe neutrino interactions in an energy range from a few hundred MeV to several GeV. It will also serve to test a membrane-style cryostat, which is planned to be used in the DUNE detector of the Long Baseline Neutrino Facility (LBNF).

4.3.2 SBN Intermediate detector: MicroBooNE

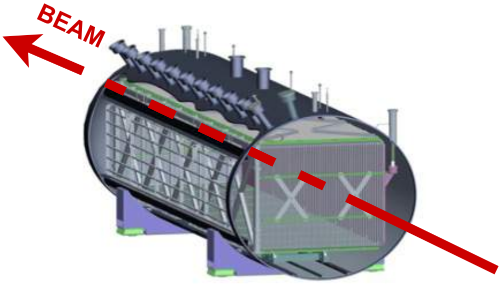

Figure 4.10: The MicroBooNE detector cryostat. The field cage is shown inside the cryostat. Figure from [126].

The MicroBooNE detector is schematically shown in Figure 4.10. The active region of the TPC is a rectangular volume of dimensions of 2.33 m × 2.56 m × 10.37 m. The detector contains 85 tons of liquid Argon. The MicroBooNE TPC design allows ionisation electrons to drift up to 2.56 meters to a three-plane anode wires. Three anode readout planes (Y, U, V), spaced by 3 mm, form the beam-right side of the detector, with 3,456 Y wires arrayed vertically and 2,400 U and 2,400 V wires oriented at ±60° with respect to the vertical ones. An array of 32 PMTs is mounted behind the wire planes on the beam right side of the detector to collect prompt scintillation light produced in LAr.

MicroBooNE can also record interactions from an off-axis component of the NuMI neutrino beam. MicroBooNE has taken data since 2015, and the CRT system has helped reject background since 2018. The first physics results obtained by the MicroBooNE collaboration are presented in Section 4.4.

4.3.3 SBN Far detector: ICARUS T600

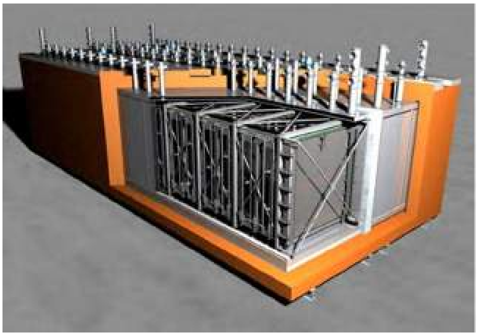

Figure 4.11: The ICARUS detector schematic showing both modules and the common insulation surrounding the detector. Figure from [108].

ICARUS is the largest among the three SBN detectors and it is schematically shown in Figure 4.11. It serves for detecting the oscillated neutrino flux in both electron and muon flavours. As the contributions to the ICARUS detector work in the SBN program are the subject of this PhD thesis, Chapter 5 is entirely dedicated to it. Its main characteristics are also presented in Section 3.3, when discussing the LAr TPC functionality. However, a short description is also given here for consistency with the descriptions of the SBND and MicroBooNE detectors.

The ICARUS detector consists of two large identical modules (see Section 3.3 for dimensions) filled with 760 tons of liquid Argon in total (476 tons of LAr active mass). Each module houses two TPCs separated by a common central cathode, thus the ICARUS detector houses four TPCs in total. Each TPC anode, consisting of three parallel wire planes, 3 mm apart, with 3 mm pitch, is spaced 1.5 m from the cathode. The wires are oriented at 0°, ±60° with respect to the horizontal direction. Globally, 53,248 wires with length up to 9 m are installed in the detector. In order to help rejecting cosmic bakcground, the detector will be surrounded by Cosmic Ray Taggers and covered by almost 3 m of concrete overburden.

The ICARUS detector, after extensive refurbishing at CERN, was installed at FNAL in the SBN far site in 2018. The detector cool down, filling with LAr, and cryogenic commissioning was completed in May 2020. The detector is filled with liquid Argon and in stable operations at the nominal drift field of 500 V/cm since August 27th 2020, with the first physics data taken in June 2021.

4.4 Initial results of the MicroBooNE data taking

The SBN program can already thrive on the MicroBooNE experience that has been stably operating since 2015. Mastering the challenging but powerful LAr TPC, MicroBooNE collaboration has presented several publications related to a better understanding of this detection technology, energy reconstruction and improvements of the simulation models and publications concerning the neutrino cross-section measurements on Argon.

Significant progress has been made in the MicroBooNE TPC data analysis, including TPC noise filtering [127], wire signal processing and deconvolution [128, 129], reconstruction algorithm development, including the Pandora multi-algorithm pattern recognition [130], deep learning with convolutional neural networks [131, 132], and a 3D imaging of the ionisation electrons prior to the pattern recognition, based on the most fundamental information like time and amplitude of the signal and the detector geometry [133].

The next improvement concerns the simulation of bulk properties such as the space charge effect, which distorts the electric drift field and is caused by the accumulation in LAr of positive ions from the high rate of cosmic rays impinging the detectors operated near the surface. In particular, techniques to measure and correct for space charge effects in large LAr TPCs have been developed using a dedicated UV laser system and the cosmic muon MicroBooNE data [134, 135]. A novel method, the charge-light matching, that pairs the TPC charge activity to the detected scintillation light signal, enables a powerful rejection of cosmic ray muons in the MicroBooNE detector [136]. Considerable reduction of the detector related uncertainties has also been achieved by the correct simulation of induced charge on neighbouring wires and a much-improved calibration procedure.

Besides the improvements in the reconstruction software, the number of background events due to cosmic muons has also been reduced significantly by using the Cosmic Ray Tagger system [137].

By developing novel reconstruction and data analysis techniques, the MicroBooNE detector performed a series of cross-section measurements on Argon. The two important ones, namely of the inclusive ν_μ charged current cross-section [138] and of the combined inclusive $\nu_\mathrm{e}+\bar{\nu}_\mathrm{e}$ flux-averaged charged-current cross-section [139] are briefly discussed below.

The inclusive ν_μ charged-current interaction cross-section on Argon in MicroBooNE using improved detector response simulation, reconstruction, and with improved cosmic background rejection using an external CRT has been measured using data collected from the BNB beam between December 2017 and July 2018, corresponding to an integrated exposure of 7.6×10^{18} POT. The ν_μ CC inclusive cross-section measurement on Argon resulted in $\sigma = 0.800 \pm 0.030 \pm 0.101 \times 10^{-38}$ cm^2 [140]. Comparing its central value with the previously published result, of $\sigma_{previous} = 0.693 \pm 0.010 \pm 0.165 \times 10^{-38}$ cm^2 [138], the new value agrees within the uncertainty with the previous measurement. It also agrees with the cross-section extracted from simulation $\sigma_{MC} = 0.801 \times 10^{-38}$ cm^2 using the passing signal events instead of background-subtracted data, which is also presented in Figure 4.12.

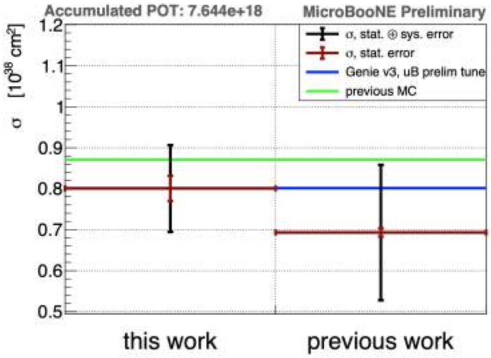

Figure 4.12: Comparison of the improved ν_μ interaction cross-section measurement with the MicroBooNE previous result including the full systematic uncertainties. Figure from [140].

The combined inclusive $\nu_e + \bar{\nu}_e$ flux-averaged charged-current cross-section on Argon has been measured using an off-axis NuMI beam data [139]. The reconstruction of 214 candidate $\nu_e + \bar{\nu}_e$ interactions with an estimated exposure of 2.4×10^{20} POT was performed. The estimated purity of 38.6% gives a sample of 80 $\nu_e + \bar{\nu}_e$ events in Argon, the largest one up-to-date. A fully automated discrimination technique of electron and photon-induced showers, based on particle energy loss measurements on LAr TPC was applied in the analysis of these data. The $\nu_e + \bar{\nu}_e$ flux-averaged charged-current total cross-section was measured to be $\sigma = 6.84 \pm 1.51$ (stat.) $\pm$ 2.33 (sys.) $\times 10^{-39}$ cm^2 per nucleon, for neutrino energies above 250 MeV and an average neutrino flux energy of 905 MeV for this threshold. The measurement is sensitive to neutrino events where the final state electron momentum is larger than 48 MeV/c, covers the entire angular phase space of the electron, and matches with the theoretical predictions from the GENIE and NuWro [141] neutrino generators. This analysis also demonstrates (for the first time) the electron neutrino reconstruction in a LAr TPC exposed to a considerable cosmic background, which is a critical task for surface experiments, like the SBN. A candidate ν_e interaction in the MicroBooNE detector is presented in Figure 4.13.

During the last stage of this thesis editing, the results of analyses of data taken with the MicroBooNE detector addressing the low-energy excess of electron-like events observed by the MiniBooNE detector, as discussed in Section 2.1.2, have been published. Addressing the MiniBooNE anomaly, the MicroBooNE collaboration adopted two methods of analysis. The deep-learning-based analysis selecting

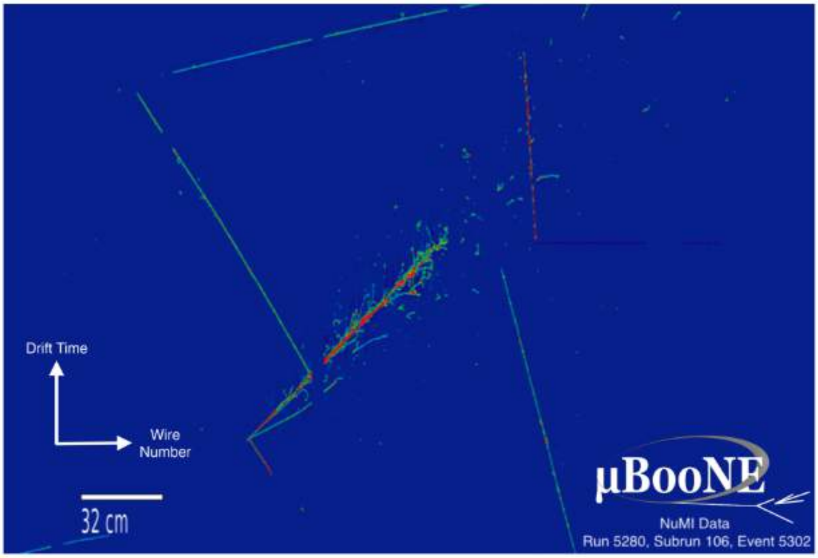

Figure 4.13: A display of a selected electron neutrino candidate recorded by the MicroBooNE detector using the NuMI beam alongside a number of cosmic ray tracks. The horizontal direction represents the wires on the collection plane, and the vertical direction represents the electron drift time. Colours represent the amount of charge deposited on the wires, with blue corresponding to the smallest and red corresponding to the largest deposit. The gaps in some of the cosmic-ray tracks and the electromagnetic shower are due to unresponsive wires. Figure from [139].

neurino interactions consistent with kinematics of CCQE-like events [142] and by analysing single electron final states across multiple signal topologies [143].

The MicroBooNE analysis was performed using 7×10^{20} POT of Fermilab BNB neutrino-mode data. About half of the collected dataset, with each analysis examining a hypothesis for the nature of the MiniBooNE low-energy excess, was used. Thanks to the capabilities of the LAr TPC technology to image various leptonic and hadronic final states, the searches featured excellent signal identification and background rejection. In addition, the analyses used data-driven ν_e estimates constrained by high-statistics samples of π^0 and ν_μ CC events. The expected event rate was dominated by intrinsic ν_e CC events originating from the beamline rather than background photons.

Both analyses indicated that the results are consistent with the nominal ν_e rate from the BNB beam and no excess of the low-energy ν_e candidates was observed. For the analysis of multiple final state topologies the mutually compatible, statistics-limited measurements were either consistent with or modestly lower than the predictions for all ν_e event classes, including inclusive and exclusive hadronic final-states, and across all energies. MicroBooNE rejected the hypothesis that ν_e CC interactions are fully responsible for the MiniBooNE low-energy excess at 97% CL.

Chapter 5

ICARUS detector for the SBN program

This chapter describes some of the ICARUS detector subsystems regarding their refurbishment at CERN and installation at Fermilab. Given the operation in the SBN experiment at Fermilab, the detector required several improvements to operate in the large cosmic background conditions. Therefore, in the first section of this chapter, the main improvements made during the detector refurbishment at CERN are described, followed by a description of the detector installation and commissioning at Fermilab.

During the detector overhauling, I was present at CERN as a technical student and contributed to this process already back then. My contributions include the leak-tightness and mechanical vacuum testing of the new cold vessels necessary to certify the their reliability, preliminary tests of the PMTs, tests of dedicated electronics boards, and cabling and installation of the PMTs inside the detector. I was also responsible for collecting and documenting all the available data for the future PMT database of SBN. This data has already been used for several purposes, and some of the results concerning the PMT tests were presented at many international conferences and published in scientific journals. During that time, I also carried out the reliability tests of the new Decoupling and Biasing Boards (DBBs) at both room and LAr temperatures.

5.1 ICARUS detector overhauling at CERN

The ICARUS detector was transported from Gran Sasso to CERN at the end of 2014 for overhauling oriented towards its future use in the SBN experiment. During its operation in the underground Gran Sasso laboratory, the detector was working in low background conditions. At FNAL, the detector operates on the Earth's surface and is therefore exposed to significant cosmic background. In order to prepare for the new operating conditions and fulfil the SBN requirements, a proper refurbishment of the detector had to be undertaken. The WA104 programme at CERN was conceived for the required refurbishment operations.

The renovation was held for each ICARUS module separately in a dedicated clean room at CERN building 185, as it is shown in Figure 5.1. The refurbishment operations, in a framework of the WA104 programme at CERN, included:

- construction of new cold vessels and the new passive thermal insulation;
- refurbishing the cryogenic and purification equipment;
- implementation of new cathodes with a better geometric uniformity;
- improvement of the existing warm electronics;
- replacement of the old light collection system with a new one based on 360 PMTs.

Figure 5.1: A photograph of one of the ICARUS modules inside the clean room at CERN. Image credit: CERN.

5.1.1 New cryostats and cryogenic system

The new cold vessels made of double-wall extruded Aluminium profiles welded together were designed and assembled by CERN/INFN personnel. New passive insulation with a maximal heat loss of 10 to 15 W/m^2 was also installed around the vessels. After moving the detector to FNAL into the new building dedicated to the detector, the cold vessels surrounded by the insulation were placed in a warm vessel. The warm vessel and the insulation share the same design featured in all the other cryostats built within the Neutrino Platform (cryostats of SBND and two ProtoDUNE detectors).

The cryogenic plant refurbishment was related to the installation of a new cold shield, circulating dual-phase N_2 around the cold vessels and intercepting residual heat losses through the insulation in the warm vessel. Moreover, Argon circulation, cooling and purification circuits were also completely redesigned and assembled.

5.1.2 The TPC cathode correction and new readout electronics

The ICARUS TPC cathodes are made of a stainless steel frame structure that supports punched stainless steel sheets. The cathodes were disassembled and subjected to a thermal procedure to reduce the out-of-plane deviations by a factor of 10 (the original deviations were $\sim$25 mm). The correction aims to obtain a more homogeneous electric field, which allows for greater precision in the neutrino interaction studies, as indicated by the analysis of the LNGS data on muon momentum measurements with multiple scattering [144].

The new electronics, housed onto the wire signals feed-through flange, required wire biasing inside the detector to avoid having signal cables biased to the wire voltage. INFN Padova and CERN experts jointly have developed new Decoupling and Biasing Boards (DBBs) to decouple HV bias and signal on TPC wires. The boards, their tests and installation are presented in Figure 5.2. Each DBB is made of 16 simple RC circuits. However, due to some defects caused during the manufacturing and assembly process, they had to be modified by replacing the RC modules.

Another improvement was related to a new *warm* electronic chain for the TPC readout exploiting the same past architecture while profiting from newer, higher-performing components and technologies. The term *warm* means that the readout electronics are located outside the detector. The new components were tested at CERN on a small 50-litre LAr TPC (for more details on the 50-litre LAr TPC, see Chapter 8). Each TPC readout board hosts 64 low front-end noise, charge sensitive preamplifiers, 64 serial 12 bit ADC (2.5 MHz), FPGA, memory, and optical link interface. Nine boards (serving 576 wires) are housed in a mini-crate specially designed to connect directly to a feed-through of the cold vessel's flange. Reducing its size allows getting rid of heavy racks occupying a large section of the cryostat roof.

The analysis of the cosmic data collected with the CERN test stand resulted in a noise RMS of $\sim$2 ADC counts, i.e., $\sim$1000 e^-, on all wire planes, and a signal-to-noise ratio not higher than 10 [145]. The bipolar induction signal showed symmetric and almost un-distorted shape even in heavily-populated showers. This yields clear track separation even for crowded events and allows for charge measurement even in the induction views.

In ICARUS, the 53,248 TPC wires will be connected to 1664 32-channel flat cables and served by 856 DBBs on 96 flanges, with nine DBB cards (576 channels) being hosted on each flange.

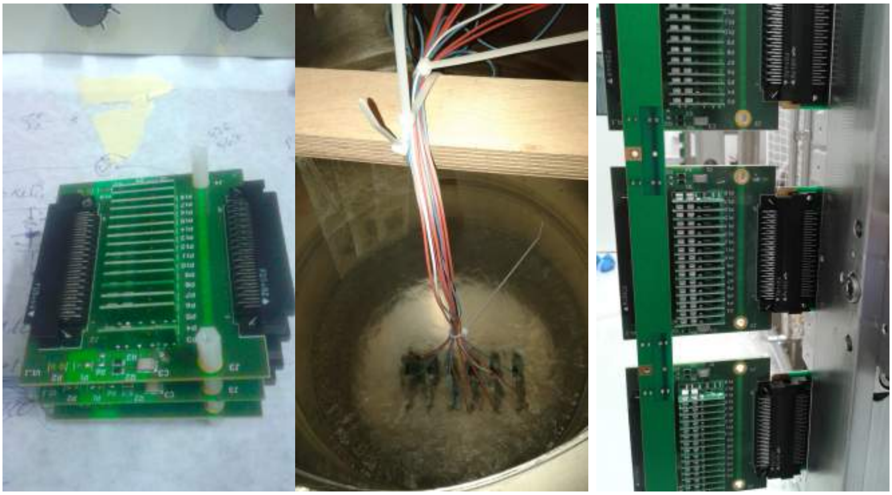

(a) (b) (c)

Figure 5.2: The Decoupling and Biasing Boards tests and installation at CERN. The boards were tested several at a time by placing one on top of the other (Figure 5.2a) and then immersing them in a LAr bath (Figure 5.2b) to measure decoupling RC at HV and test the thermal shock. After tests, the DBBs were installed in the detector (Figure 5.2c).

5.1.3 New light detection system

A light detection system based on 74 ETL 9357 FLA (8-inch diameter) PMTs mounted behind the wire chambers was adopted in the T600 detector for the LNGS run. ICARUS at Fermilab, facing more challenging experimental conditions than at LNGS due to the expected significant cosmic background, required several improvements. Namely, an increased number of PMTs as well as a PMT model with better sensitivity down to 100 MeV of deposited energy and improved time resolution of $\mathcal{O}(1 \text{ ns})$. The system should identify events with energy deposited in LAr volume from 100 MeV to 1 GeV to cover the full expected energy range in the SBN configuration. The increased number of PMTs and improved timing resolution are needed to localise the tracks associated with every light pulse along the ∼20 m of the longitudinal detection direction, with accuracy better than 1 m, i.e., shorter than the expected average spacing between cosmic muons in each TPC image. In this way, the light detection system will provide the absolute timing for each track, which allows to identify those originating from a neutrino interaction by matching the time of each track with the time of the beam spill among the several tracks in the LAr TPC image.

Several studies were performed to select the best PMT layout in terms of triggering, event localisation, and identification [146]. The various layouts were considered with both 8-inch and 5-inch diameter window PMTs. The optimal solution was found to be the layout of 90 8-inch PMTs per TPC wall, resulting in a total of 360 PMTs in the whole ICARUS detector, corresponding to a 5% coverage of the wire plane surface.

As a next step, several PMT models manufactured by different producers, such as Hamamatsu and ETL, were tested [147] to identify the most suitable one for the ICARUS light detection system requirements at the SBN experiment. The selected model was the Hamamatsu R5912-MOD with a diameter of 8 inches.

The tests of these photomultipliers at CERN and the detailed characteristics of the new light detection system are described in the next chapter dedicated to that system. Some of the PMT tests and their results are described in my master diploma thesis [148]. In addition, the input data for the PMT database are presented in its Appendix.

5.2 ICARUS detector at FNAL

After refurbishment, the detector was transported to Fermilab in 2017. The final placement of the two modules in the SBN far detector building at Fermilab was completed in 2018. In 2019, the insulated cold vessels (filled with air only) were installed into the warm vessel at the experimental hall as shown in Figure 5.3.

5.2.1 Detector installation and commissioning

The activities related to the cryogenic commissioning of the ICARUS detector started shortly afterwards. The procedure consisted of four main subsequent phases:

- detector volume evacuation;
- cryostat cooling down;
- LAr filling and GAr purification/recirculation start-up;
- LAr purification/recirculation start-up.

After installing the vacuum system in April 2019, due to the testing and vacuum operation procedure approval, the vacuum pumping on the East cold vessel started in June 2019. Pumping of the West module started after installing and testing the transfer line connecting the LAr recirculation pump. The vacuum pumping phase continued for three months until the start of cooling down the detector. The achieved

Figure 5.3: ICARUS insulated cold vessels assembly into the warm vessel at Fermilab. Figure provided by the ICARUS collaboration.

vacuum level on the West module was $\sim 10^{-5}$ mbar, and $\sim 5 \times 10^{-5}$ mbar on the East one.

In September 2019, the East module was taken from vacuum to atmospheric pressure to rearrange the readout cables of the TPC horizontal wires. In October 2019, the East module was put back under vacuum at about 5.5×10^{-5} mbar. At this point, the system was ready for the activation of the LAr filling. The first LAr delivery was expected by the end of October 2019.

On February 13, 2020, the two main cold vessels were filled with ultra-purified gas Argon (GAr). The detector cool down started on February 14 by injecting liquid Nitrogen into the cold shields. It took about four days to bring the temperature on the wire chamber below 100 K. On February 19, the gas recirculation units were put into operation to purify the GAr before filling the detector with LAr. The continuous filling with ultra-purified LAr started on February 24 and was completed on April 19. The level of the liquid Argon during the filling of the ICARUS detector is presented in Figure 5.4. Stabilisation and the start of LAr recirculation and purification were completed in May 2020.

The remaining installation and commissioning activities were delayed due to travel and onsite presence constraints consequent to the COVID-19 pandemic outbreak. Due to the prevailing restrictions, I could not travel to Fermilab in person as planned to help to commission the detector components. The pandemic situation delayed the detector readiness for the data taking by a few months.

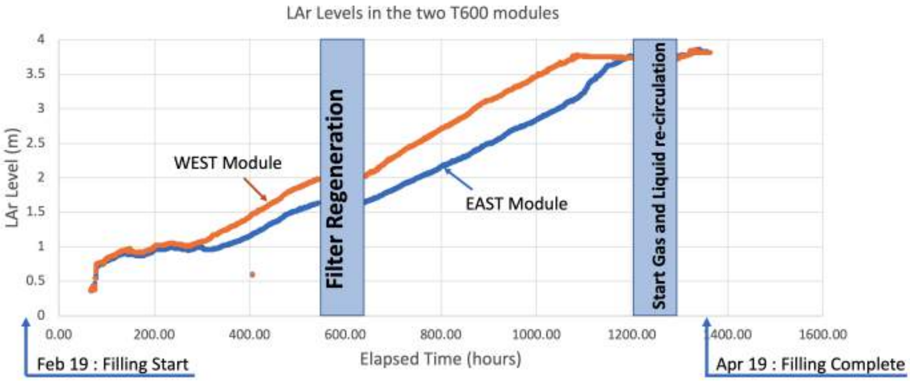

Figure 5.4: The LAr levels (in meters) in both ICARUS modules during the filling procedure that took place from February 19 until April 19. The LAr level in the West module is represented by the orange line and in the East module by the blue one. Figure provided by the ICARUS collaboration.

The PMT system was activated in July 2020. Since its activation, the system has shown excellent stability regarding PMT functioning and DAQ electronics. On August 27, the TPC wire planes and cathode HV were set at the nominal voltages. The HV is stable at -75 kV, without glitches or other issues. In August 2020, ICARUS recorded the first particle tracks from cosmic rays.

The bottom and side CRT walls (see next section) have been steadily operational since November 2020. The trigger system that brings together all the other subsystems is still under commissioning and is described in Chapter 7, which is fully dedicated to that system. During the cryogenic commissioning, the TPC, PMT and CRT systems have been continuously monitored to detect effects related to the operation of the cryogenic systems.

ICARUS began taking test data from the BNB in December 2020. Exposed to both neutrino beams at Fermilab, the ICARUS detector has recorded the first muon and electron neutrino candidates, as shown in Figure 5.5.

5.2.2 Cosmic Ray Taggers

One of the ICARUS systems installed at Fermilab was the Cosmic Ray Tagger (CRT). This system has been proposed for all the SBN detectors for a better identification of cosmic rays crossing the LAr volume [110]. The ICARUS CRT will consist of scintillator planes on all sides of the detector, with different implementations for the top, side and bottom areas, covering a surface of ∼1000 m^2. The CRT system, initially planned to be designed and built from scratch, was later partially adopted

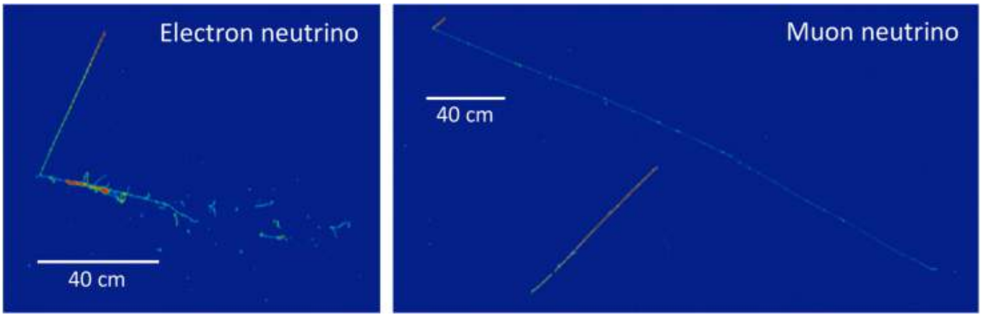

Figure 5.5: The left part of the figure shows an electron neutrino interaction candidate that produced a proton (top track) and an electron that produced an electromagnetic shower (bottom tracks). The right part of the figure illustrates a muon neutrino interaction candidate that produced a proton (short track, top left) and a muon (3.4-meter-long track). Next to the muon neutrino interaction, a cosmic-ray track interaction is also visible in the lower half of the image. In both cases, the images were registered by the collection plane and the neutrino beam came from the left. Image credit: ICARUS collaboration.

from other experiments.

Space and time constraints limit the possibilities for the bottom CRT. Space constraints because of the cryostat support, time constraints because the bottom CRT needed to be in place before the warm vessel installation. Fortunately, the Double Chooz detector, which has just stopped collecting data, made use of cosmic ray veto modules that could be retrieved and installed under the ICARUS detector to serve as a bottom CRT. The Double Chooz modules provide a total area of ~200 m^2 of scintillator planes that cover about 50% of the bottom area, as shown in Figure 5.6.

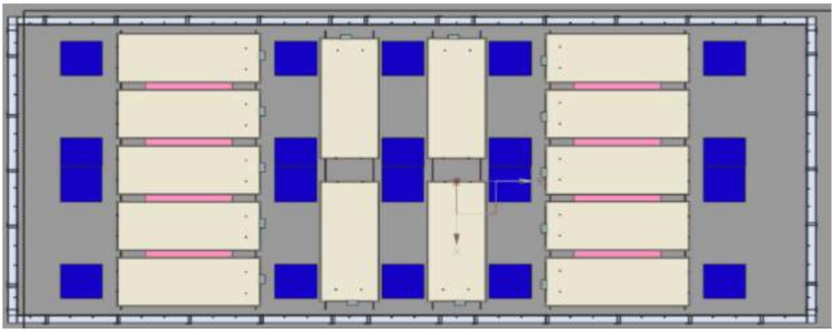

Figure 5.6: Bottom CRT layout, each module is illustrated as a light yellow rectangle. Figure provided by the ICARUS collaboration.

At the same time, the MINOS far detector has just been decommissioned. The main detector was largely destroyed during this process, but the cosmic ray veto shield was recovered. 173 MINOS scintillator modules were retrieved from the Soudan mine and shipped to Fermilab, building up a ∼450 m^2 side CRT for ICARUS.

The remaining ∼400 m^2 of the CRT for covering the top side of the cryostat is a new construction developed by CERN and INFN groups.

The final CRT layout, updated from the basic conceptual design presented in the SBN proposal, is shown in Figure 5.7. The bottom and side CRT modules, that are already installed at the ICARUS detector, are illustrated in Figures 5.8a and 5.8b. By the time of this thesis' final editing, the top CRT (Figure 5.8c) has been completed, while the commissioning of the whole CRT and the installation of a concrete overburden are scheduled for early 2022.

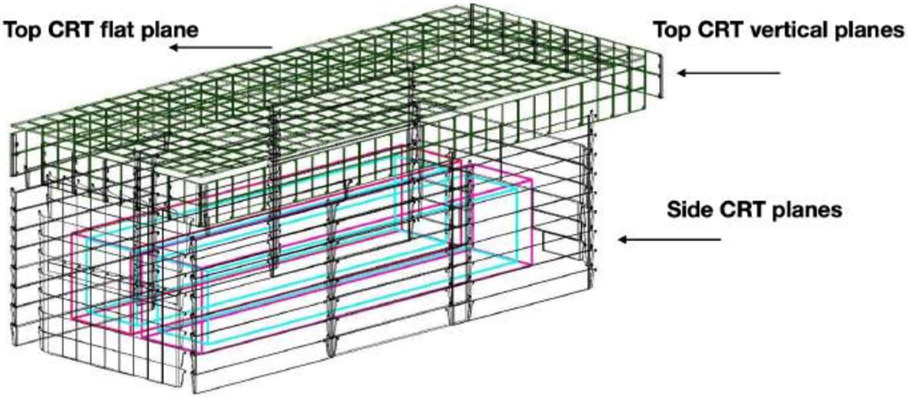

Figure 5.7: The top and the side CRT layout, including the cold vessels (magenta) and the Argon active volumes (cyan). The top CRT consists of horizontal and vertical planes, as indicated in the drawing. Figure provided by the ICARUS collaboration.

(a) Bottom CRT. (b) Side CRT modules. (c) Top CRT modules.

Figure 5.8: The pictures show the bottom (5.8a) and side (5.8b) parts of the CRT system that are already installed at the detector and 125 top CRT modules (5.8c) ready to be shipped to Fermilab. Pictures provided by the ICARUS collaboration.

Chapter 6

ICARUS light detection system

The primary task of the light detection system is to provide time information based on fast LAr scintillation light, which forms the basis of the trigger system and complements the information available from the anode wires to determine spatial positions of tracks in the detector. As indicated in the previous chapter, the light detection system upgrade was critical for the ICARUS operation at a shallow depth to handle the expected substantial cosmic background. The new ICARUS light detection system was characterised and installed during the detector overhauling at CERN after studies based on simulations and laboratory tests devoted to optimising its performance.

In this chapter, the system overview and tests of the photomultiplier tubes (PMTs) performed at CERN with definitions of the measured parameters are presented. It is based on several publications [1, 2, 3, 4] co-authored by me. My contributions include PMT tests at room and LAr temperatures, data analysis, installation and cabling of PMTs. I was also responsible for collecting and documenting all the available data for the future PMT database of SBN.

6.1 System overview

The new light detection system of the ICARUS detector is equipped with 360 Hamamatsu R5912-MOD 8" PMTs. The PMTs are distributed among four detector walls, 90 per wall. Figure 6.1 illustrates a schematic of the layout of 90 PMTs on one wall. This arrangement is also applied to the remaining three walls.

The PMTs are mounted on the wire chamber frames placed 20 cm behind the wire planes of each TPC, at a minimum distance of 5 mm between the PMT photocathode and the wires of the Collection plane. Each PMT is mounted on a dedicated structure that maintains its correct position and orientation and prevents electrical interference with the wire planes through additional grounded screening grids. In addition, a 50 μm optical fibre in front of each PMT and pointing towards its photocathode

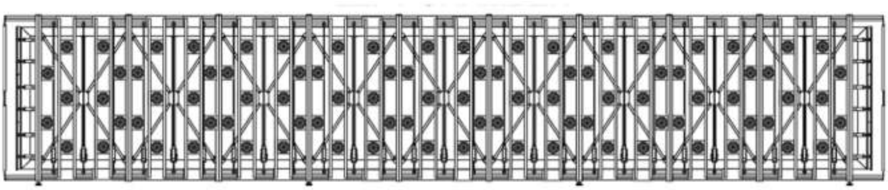

Figure 6.1: A schematic picture of the 90 PMTs (dark circles) placed on one of the ICARUS walls. Figure provided by the ICARUS collaboration.

centre is installed, allowing for the gain and timing calibration using fast light pulses generated by an external laser. Figure 6.2 shows a photograph, taken in the dedicated cleanroom at CERN, of a part of the ICARUS module with installed PMTs.

Figure 6.2: PMTs installed on the ICARUS detector wall according to the schematic shown in Figure 6.1. Figure from [2].

More detailed information about all elements of the ICARUS T600 light detection system is given in the Appendix to my master thesis [148]. In particular, the positions of all 360 PMTs in the ICARUS coordinate system are defined, and the naming and numbering conventions are presented. The PMT serial number is given together with indices of the connected HV cable, signal cable, and optical fibre for each PMT position.

6.2 PMT characteristics

Photomultiplier tubes, converting a scintillation light signal into a usable electrical pulse, without adding a big amount of random noise to the signal, allow to detect light even at a single-photon level.

6.2.1 PMT construction and basic definitions

A typical PMT, schematically shown in Figure 6.3, consists of two major elements: a photosensitive layer, called the photocathode, and an electron multiplier structure, composed of several dynodes and an anode. All these elements are placed in a sealed glass envelope with a high vacuum inside. The incident photon entering the PMT through the input window (faceplate) can be absorbed by the photocathode, and its energy is used for a photoelectron (phe) emission through the photoelectric effect. The efficiency of converting photons into photoelectrons is known as the photocathode's quantum efficiency (QE). It depends on the wavelength of the photon and properties of the photocathode material, and its typical values are between 15% and 30%. The emitted photoelectrons are accelerated by the applied electric field towards a first dynode, from which the secondary electrons are released. Each of these electrons is accelerated along its path and unleashes successive electrons from subsequent dynodes. As a result, a typical input scintillation pulse will give rise to about 10^7 - 10^{10} electrons, which is the output charge signal collected at the anode. Apart from the photocathode quantum efficiency and the efficiency of the electron multiplier, the intensity of the output signal depends on the number of photons incident on the photocathode and their energies. A detailed description of the PMT construction and performance can be found in Ref. [149].

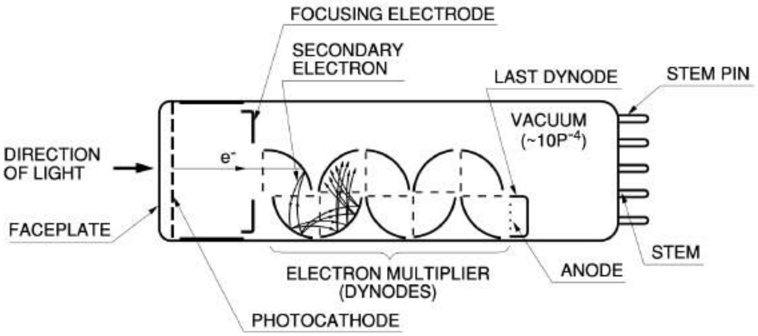

Figure 6.3: Schematic picture of the photomultiplier tube. Figure from [149].

The most important characteristics of the PMT performance are related to its output signal distribution (noise, gain) and its timing properties (electron transition time and its spread, rise time, fall time). Other important factors are signal linearity and saturation. There are several characteristics of the PMT individual components, e.g., photocathode uniformity.

A schematic output signal distribution of the PMT, with and without an input optical signal, is shown in Figure 6.4. The so-called dark current, which is the main source of the PMT noise, is composed of leakage currents between electrodes on the glass and insulating surfaces of the tubes and electrons emitted from the photocathode and dynodes as a consequence of the thermoelectric effect. In the case of input signals at the single-photon level, the number of photoelectrons is described by the Poisson distribution, and the signal peak in Figure 6.4 corresponds to a single photoelectron response (SPR[1]). The PMT gain, defined as the ratio of the number of electrons at the PMT output to a single photoelectron at the input, is given by the position of this peak. PMT responses corresponding to two and three photoelectrons, which cause broadening of the signal distribution, are usually also considered.

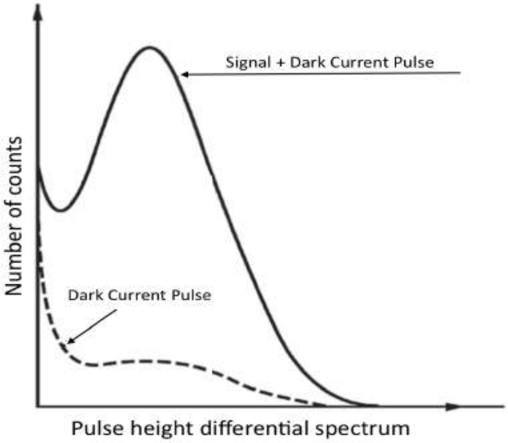

Figure 6.4: Demonstration of the PMT output signal reproduced from [149].

PMTs are characterised by very fast responses. Parameters characterising their timing properties are presented in Figure 6.5. The time needed for electrons to traverse the whole photomultiplier tube is called the transit time (TT). It varies for the individual incident photons, so the transit time spread (TTS) is an important PMT characteristic. The rise time of the electrical signal is defined as the time it takes the output pulse to rise from 10% to 90% of the peak pulse height. The fall time is defined as the time it takes for the electrical signal to change from 90% to 10% of the peak output pulse height.

---

[1] The alternative abbreviation SER is also commonly used in literature.

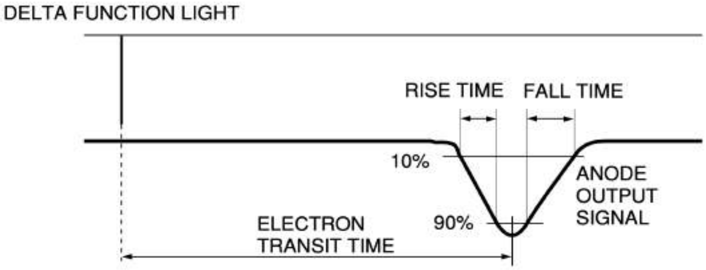

Figure 6.5: Simplified illustration of the PMT timing definitions. Figure from [149].

6.2.2 Characteristics of the ICARUS PMTs

Several tests with different PMT types were carried out to select the most suitable ICARUS PMTs to fulfil SBN requirements. The final results of the tests for the three types of PMTs considered are given in Table 6.1. All the measured parameters of each PMT type were compatible with what was reported by the manufacturer. Although all three models marked good photocathode uniformity and linear behaviour, the Hamamatsu R5912-MOD PMT was chosen because of its best performance at the cryogenic temperature [147].

Table 6.1: The comparison of three PMT types [147].

	Hama R5912[1]	Hama R5912-02	ETL 9357KFLB
No. dynodes	10	14	12
Gain (typical)	10^7 (at 1500 V)	10^9 (at 1700 V)	10^7 (at 1500 V)
Rise time (ns)	3.8	4	3.5
TTS (FWHM ns)	2.4	2.8	4
Dark current (nA)	50	10^3	10
QE at 390 nm (%)	25	25	18

[1] This is the chosen PMT model, which later in the text is referred to as Hamamatsu R5912-MOD.

The PMT Hamamatsu R5912-MOD with 8 inches (20 cm) diameter is shown in Figure 6.6. The feature window of this model is made of borosilicate glass. It has 10 dynodes and a bialkali photocathode (K_2CsSb) with platinum undercoating to restore the photocathode conductivity at cryogenic temperatures. A custom-made base circuit was installed at each PMT to supply the high voltage for the photocathode grids, dynodes and anode, and to make possible the signal readout directly from the anode. The main characteristics of the Hamamatsu R5912-MOD PMTs, as provided by the producer, are reported in Table 6.2. This model has very good timing characteristics and its response is linear up to 150 phe.

Figure 6.6: The PMT model Hamamatsu R5912-MOD. Figure from [1].

The scintillation light emitted by particles in LAr is characterised by photons with a wavelength $\lambda = 128$ nm. This wavelength is too short for penetrating through the glass enclosure of the PMT. Thus, it is necessary to convert this light to one with a longer wavelength ($\sim$500 nm) by depositing a special wavelength shifter on the photocathode. The uniform layer of the TPB (Tetraphenyl Butadiene) wavelength shifter of a thickness of $\sim$200 μg/cm^2 was deposited by the ICARUS collaboration on the sensitive surface of each PMT by using a dedicated evaporation system [150].

Table 6.2: The main PMT features and acceptance requirements for the visible light, provided by the manufacturer. Table from [151].

Spectral response	300 - 650 nm
Window material	borosilicate glass (sand blasted)
Photocathode	bialkali with Pt under-layer
Max. supply voltage (anode-cathode)	200 V
Photocathode QE at 420 nm	15 - 16%
Typical gain	10^7 at 1500 V
Nominal anode pulse rise time	3.6 ns
Nominal Peak-to-Valley ratio	2.5
Max. dark count rate	5000 Hz
Nominal electron transit time	54 ns
Max. transit time variation	2.5 ns
Pulse linearity variation	± 10% up to 150 phe

6.3 PMT tests and measurements at CERN

The 400 PMTs (360 to be installed in the detector and 40 spares) were tested at room temperature to evaluate their performance and conformity to the requested features. In addition, 60 of them were also tested at cryogenic temperature to evaluate any parameter variation which could affect the LAr scintillation light detection. Moreover, some specific tests, such as the signal linearity as a function of supply voltage and light intensity were performed for smaller number of PMTs. All these tests also aimed at cross-checking the acceptance tests performed by the producer.

6.3.1 Test setups

Tests at room temperature took place in a specially arranged dark room at CERN's IdeaSquare building (Figure 6.7a) [1]. The measurement apparatus located in the adjacent electronics workshop was based on a laser diode producing fast pulses of light with a wavelength of 405 nm and a repetition rate of about 1 kHz. The light intensity was set using calibrated optical filters mounted on two-wheel brackets, providing various attenuation combinations (factor of 1 to 1000). The light was focused on the PMT windows using 100 μm multimode optical fibres. The PMT output was integrated by a charge preamplifier (CANBERRA 2005) and shaped by an amplifier (ORTEC 570). The PMT charge distribution was recorded by a multichannel analyser (CAEN N915), and the PMT waveforms by a 10 GS/s oscilloscope (LeCroy-WaveRunner 104MXI).

(a) IdeaSquare.

(b) Building 182.

Figure 6.7: The test setups at CERN for PMT tests at room (left) and cryogenic (right) temperatures. Pictures from [1].

Tests at cryogenic temperature were carried out at CERN, in building 182 [1]. In groups of 10, as presented in Figure 6.7b, the PMTs were directly immersed inside a large dewar filled with liquid Argon (T = 87 K) and illuminated using a single 100

μm multimode optical fibre. The same acquisition system described above was used and maintaining darkness and thermal isolation was guaranteed.

6.3.2 Gain and dark current determination

The gain and dark current are determined based on the PMT output charge distribution for single photoelectron excitation. An increase of the supplied voltage results in an increase of both of them. An example of the PMT output charge distribution, one of many analysed by me, is shown in Figure 6.8.

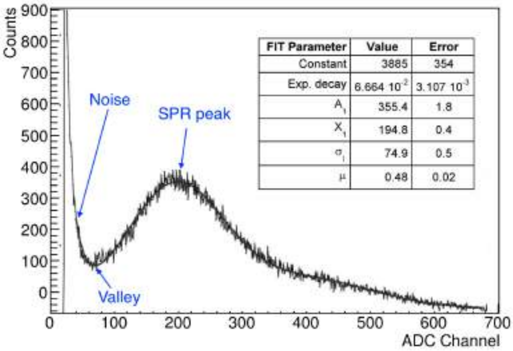

FIT Parameter	Value	Error
Constant	3885	354
Exp. decay	$6.664\ 10^{-2}$	$3.107\ 10^{-3}$
A_1	355.4	1.8
X_1	194.8	0.4
σ_1	74.9	0.5
μ	0.48	0.02

Figure 6.8: The PMT charge distribution under single-photon illumination. The result of the fit, using the formula described in the text, is represented by continuous black line. The plot can be found in Ref. [1].

The PMT charge distributions were fitted with an analytical expression consisting of an exponential function that accounts for PMT and electronic noise and one, two or three Gaussian functions[2] that describe the PMT response to one, two or three photoelectrons:

$$\mathrm{F}(x) = \mathrm{C} \cdot \exp(-\alpha x) + \sum_{n=1}^{3} \mathrm{A_n} \exp\left(-\frac{(x - \mathrm{X_n})^2}{\sigma_\mathrm{n}^2}\right). \tag{6.1}$$

The following parameter constraints were used:

$$\mathrm{X_n} = \mathrm{n}\mathrm{X}_1,\ \sigma_\mathrm{n} = \sigma_1\sqrt{\mathrm{n}},\ \mathrm{A_n} = \frac{\mu}{\mathrm{n}}\mathrm{A}_{\mathrm{n}-1}, \tag{6.2}$$

where $\mathrm{X_n}$ is the position of the $\mathrm{n^{th}}$ Gaussian curve with σ_n width and $\mathrm{A_n}$ amplitude. The μ parameter represents the mean of the Poisson distribution of the number of detected photoelectrons.

---

[2] The choice of the number of Gaussian functions is chosen so as to make the fit χ^2 value not too big.

The position X_1 of the first peak allows the evaluation of the PMT gain G. The gain dependence on the PMT supplied voltage was measured by modifying the voltage in a range of values producing PMT gains from about $G = 10^7$ to $G = 5 \times 10^7$. The PMT nominal voltage was defined as the value needed to attain a gain $G = 10^7$. The nominal voltage distribution for the whole set of 400 PMTs operating at room temperature is shown in Figure 6.9. The distribution has a mean value of 1390 V and $\sigma \approx 100$ V, so the differences among the ICARUS PMTs are relatively small.

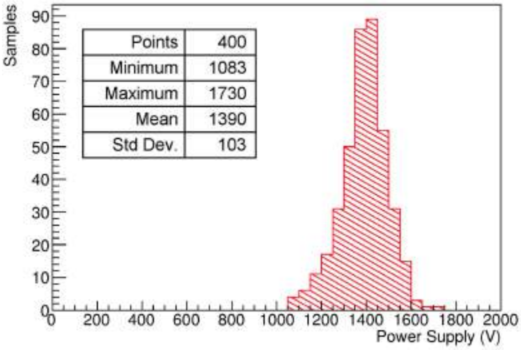

Figure 6.9: Distribution of supply voltages to achieve a nominal gain $G = 10^7$ for the total set of 400 PMTs operating at room temperature. Histogram available in Ref. [1].

The PMT dark current was evaluated by measuring the rate of the PMT pulses in the absence of light, with the discrimination threshold level set to the minimum value between the pedestal and the SPR peak. Figure 6.10a shows the dark current rate as a function of the power supply voltage. The dark current shows several trends with the voltage dependence. The trend at lower power supply values is attributable to the presence of a leakage current through the device. As the voltage increases, a second component appears, which is due to the constant thermionic emission from the photocathode [149]. The histogram of the dark current rate for 400 PMTs tested at room temperature is shown in Figure 6.10b. The average dark current rate is below the maximum value provided by the producer at room temperature.

6.3.3 Timing properties

Tests of 60 PMTs at the nominal gain of 10^7 were performed to check their timing characteristics at both room and LAr temperatures [2]. The number of initial photons was chosen to optimise a single photoelectron emission from the photocathode.

The resulting PMT anode pulses were directly sampled by the 10 GS/s oscilloscope (50 Ω input impedance). No significant variations were observed among the different tested samples, and the same mean values resulted at room and LAr tem-

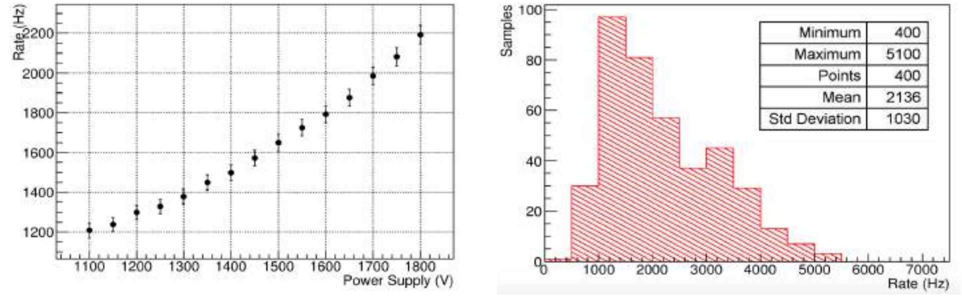

(a) The dark current rate for several voltages. (b) The dark current rate for the 400 PMTs.

Figure 6.10: The PMT dark current rate. Figure 6.10a shows the dark current rate for different values of the PMT power supply voltage with the vertical bars denoting the measured counting spreads. Figure 6.10b represents the dark current rate measured at room temperature for the 400 PMTs, with supplied voltage assuring gains at the level of 10^7. Figures from [1].

peratures: a rise time of 3.9 ± 1.1 ns, a FWHM of 5.6 ± 1.1 ns and a fall time of 10.3 ± 1.6 ns [1], in good agreement with the nominal values indicated by the manufacturer (Table 6.2).

Other tests of the ICARUS PMTs timing characteristics, like their dependence on the supplied voltage, on the position of photoelectron emission on the photocathode and on the orientation of the PMT to the Earth's magnetic field, which had been done at CERN with my participation, are summarised in Ref. [3]. They were performed at room temperature on 7 PMTs without TPB coating, and some of them were repeated at LAr temperature to evaluate possible differences.

The tests made use of a pulsed laser diode providing light with a wavelength of 405 nm and a pulse width of 120 ps FWHM and its repetition rate of 1 kHz (regulated by a pulse generator). Light intensity was set at the single-photon level, as needed for this kind of study. The light was split, using two optical fibres, towards a fast calibrated photodiode and the PMT under test. Output signals from both devices were acquired, in a common trigger mode, by a sampling 10 GS/s oscilloscope. To maintain the fibre in a fixed orientation, normal to the PMT window, but at various places, a special fibre support was produced. It is shown in Figure 6.11. The measurements were performed with fibre at position 0, i.e., illuminating the centre of the photodiode, except it is explicitly mentioned.

Figure 6.12 shows the measured PMT time characteristics (transit time and its spread, signal FWHM and rise time) as a function of the PMT power supply voltage. The correction related to the delay caused by the length of the cables was taken into account.

As expected, any increase of the inter-dynodic electric field due to an increase

Figure 6.11: The mechanical structure used to adjust the fibre position. Figure from [3].

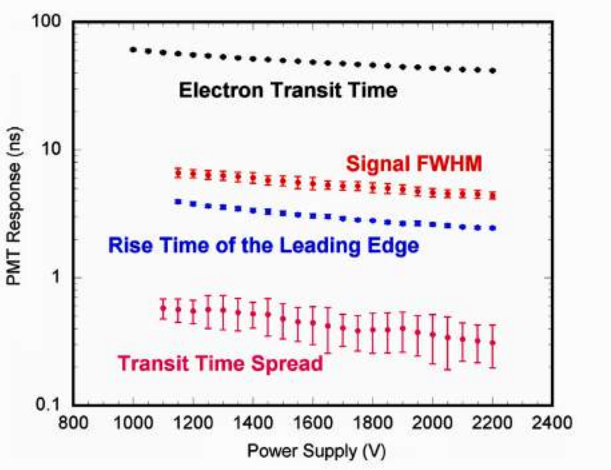

Figure 6.12: The PMT timing characteristics as a function of the supplied voltage for a single PMT (serial number: FB0389). Figure from [3].

of the supplied voltage enhances the electron speed, resulting in decreased electron transit time, reduced signal rise time and width, and decreased time spread.

Figure 6.13 illustrates the electron transit response of a single PMT as a function of the power supply voltage measured at room temperature (300 K) and at the LAr temperature (87 K) for the same PMT sample. The results are consistent with the assumption that the transit time improves in inverse proportion to the square root of the supplied voltage. The observed variation of the electron transit time between the two temperatures of ∼0.8 ns is within the systematic error of the measurement of ∼1 ns. The results of measurements performed for other PMT samples indicate good uniformity of the PMT response among them and that the PMT time characteristics are preserved at the LAr temperature.

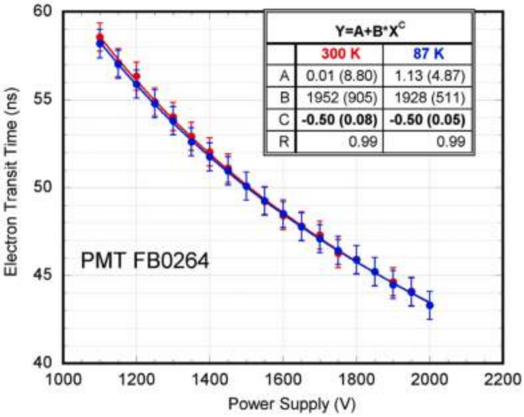

Figure 6.13: Electron transit time of the PMT with serial number FB0264, measured at different power supply voltage at room (300 K) and at LAr temperature (87 K) plotted in red and blue, respectively. Figure from [3].

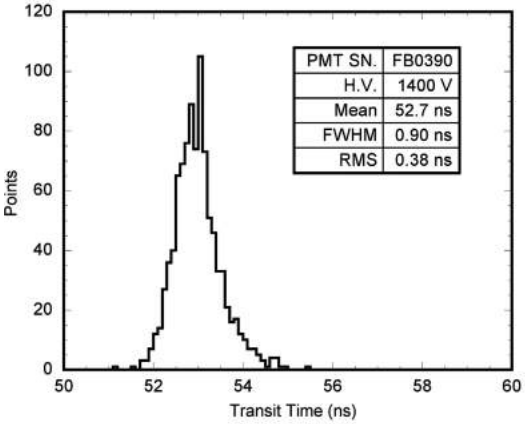

Figure 6.14: The transit time distribution for the PMT with serial number FB0390 obtained by illuminating the centre of the photocathode with the optical fibre. Figure from [3].

The spread of the electron transit time is caused by fluctuations of the transit time arising from the electron multiplication process and the photoelectron's emission position on the photocathode. In order to distinguish between these two components, the measurements with the optical fibre illuminating the centre of the photocathode and illuminating other parts of the photocathode were performed. The PMT gain was always set to 10^7.

Figure 6.14 shows an example of the transit time distribution obtained with the optical fibre illuminating the centre of the photocathode. The measured spread, RMS = 0.38 ns, can be ascribed to non-uniformity of the electron multiplication process.

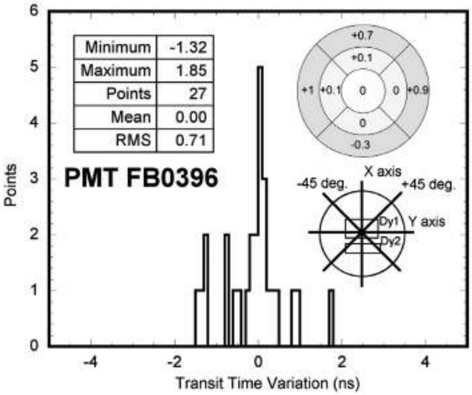

Figure 6.15: The distribution of the transit time variation for the PMT with serial number FB0396 measured by varying the optical fibre positions at the photocathode, and a map of the PMT window are shown. Figure from [3].

The results obtained by moving the optical fibre to illuminate different parts of the photocathode are shown in Figure 6.15. From the map shown in Figure 6.15, it is visible that the electron transit time increases at the photocathode boundary compared to the centre. This second effect of up to ∼1 ns is the dominant source of electron transit time variation in large area PMTs.

The resulting total transit time spread of about 2 ns FWHM at a gain of 10^7 is in agreement with the value indicated by the manufacturer.

The measurements were also performed by changing the orientation of the PMT relative to the Earth's magnetic field. Opposite to a clear dependence of the gain on the PMT orientation, with relative signal changes up to 30% - 35% [147], no corresponding changes in electron transit time were observed.

6.3.4 Signal linearity and saturation

In SBN, the ICARUS PMTs will deal with a large range of energies deposited in LAr by charged particles entering the detector or produced in the interactions with Argon nuclei. This requires good PMT linearity of up to at least 100 photoelectrons.

The response characteristics of the PMTs as a function of incident light intensity was evaluated to check the linearity and saturation. A comparison of the behaviour at room and LAr temperatures was also carried out [4].

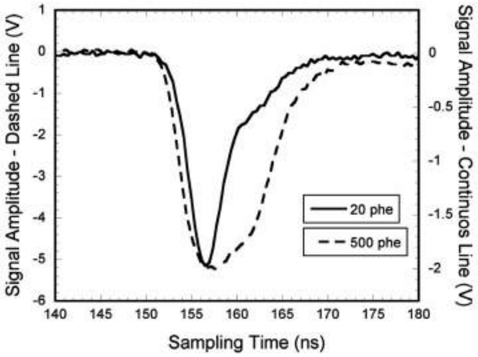

Figure 6.16: Signal distortion at high illumination values. Figure from [4].

Significant deviations from the linearity and saturation happen when the amount of incident light is very large. At high illumination values, the signal peak amplitude begins to deviate from linearity and the signal width increases. The comparison of a normal signal shape at 20 phe illumination with a distorted signal at 500 phe illumination is shown in Figure 6.16.

The dependence of the signal peak amplitude and of the total released charge on the incident light level for five different voltage supply values (from 1200 V to 1600 V) is shown in Figure 6.17. Deviations from linearity are more visible for the signal peak than for the total released charge. With increasing supplied voltage, the deviations start at lower light levels.

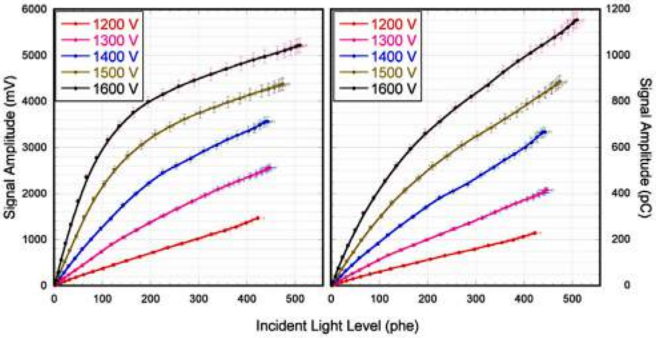

Figure 6.17: Signal peak (left) and released charge (right) as a function of the incident light level (phe) and for different power supply voltages. Figure from [4].

Figure 6.18 shows the linearity variation as a function of the incident light level at room and LAr temperatures and at a PMT gain of 1.3×10^7. The figure shows the signal peak and area reduction when compared to ideal values estimated from the light intensity setting. An improvement in PMT response at LAr temperature is visible. A possible explanation is that as the ICARUS PMTs were designed to be used in LAr, the adopted optimisation enhances current limits at low temperatures.

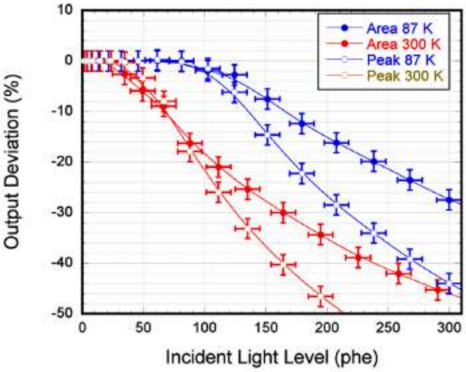

Figure 6.18: Linearity variation as a function of the incident light level at the fixed PMT gain $G = 1.3 \times 10^7$ at room temperature (300 K) and at LAr temperature (87 K), represented by red and blue plots, respectively. Figure from [4].

To summarise, significant deviations from linearity of the ICARUS PMT responses appear only above 100-150 photoelectrons and for high supply voltages. In addition, an improvement of the PMT behaviour was observed at LAr temperature. Thus, the PMTs fulfil the requirements related to their use in the ICARUS light detection system in the SBN program.

Chapter 7

ICARUS trigger system

The ICARUS detector operation at the Earth surface leads to one of its biggest challenges as it is exposed to the huge cosmic-ray background of the order of 10 kHz, which can mimic genuine neutrino interactions. The resulting total event rate dominated by the cosmogenic background would be too high to be processed or even stored. Therefore, it is fundamental to distinguish as early as possible the signals during spills of the neutrino beams from those occurring between spills, i.e., exclusively induced by cosmic rays.

The ICARUS primary trigger type, called Majority trigger, is based on the prompt signals from the LAr scintillation light in coincidence with the BNB and NuMI beam spills and is designed to provide the efficiency for capturing neutrino interactions close to 100% while eliminating background as much as possible.

The expected event rates, the developed trigger logic and its hardware implementation, followed by the future improvements, and including information about the trigger commissioning during the data taking at Fermilab in 2021, are the subject of this chapter. It is mostly based on Ref. [5] and Ref. [6]. Some information can also be found in Ref. [7] and in Ref. [152].

My contribution to the trigger development was mainly based on the work performed at the LAr test facility assembled at CERN. First tests of the electronic trigger components and preliminary studies of the trigger efficiencies performed at the CERN facility are described in the next chapter. These studies provided input to trigger simulation development, based on which further analysis of the system was carried out. The description of the trigger simulation and the results of my analyses are presented in Chapter 9.

7.1 Event rates in the ICARUS T600 detector

Concerning the signal due to neutrino interactions, the ICARUS detector is primarily exposed to the on-axis BNB beam, but also to the off-axis NuMI beam. The time structure of the BNB and NuMI beams (spills and their bunched substructures) are described in Chapter 4. A summary of their main characteristics is presented in Table 7.1. At the nominal BNB intensity of 5×10^{12} POT per spill extracted during the 1.6 μs beam gate window with 5 Hz proton extraction rate, about one neutrino interaction every 180 spills is expected to occur in the ICARUS detector [110]. Thus, the expected neutrino event rate from the BNB results in 0.027 Hz. Given the NuMI off-axis intensity of 6×10^{13} POT/spill, the spill duration of 9.5 μs and the 0.75 Hz extraction rate, one neutrino event every 53 spills is expected to cross the LAr volume [110]. The resulting neutrino interaction rate is therefore 0.014 Hz.

Table 7.1: The neutrino beam characteristics summary.

Beam:	POT/spill:	Spill duration:	Rep. rate:	Neutrino interaction rate:
BNB	5×10^{12}	1.6 μs	5 Hz	0.027 Hz
NuMI	6×10^{13}	9.5 μs	0.75 Hz	0.014 Hz

Neutrinos from both beams can interact in the material surrounding the detector active volume, resulting in an extra signal considered as background. These beam-induced events, called dirt events can occur once every 210 BNB spills [110]. The most important background is cosmic radiation that generates a dominant event rate, one over 55 BNB spills, which together with the dirt events results in 0.12 Hz of an additional signal. The background estimation for the NuMI case results in one trigger every seven spills, also mainly due to the cosmic rays in coincidence with the NuMI spill, corresponding to 0.1 Hz. Due to the decays of the cosmic muons crossing the detector up to a few μs before the BNB and NuMI spill time window, an additional signal must be considered. About 15% of these muons will come to rest, contributing globally with an additional 0.03 Hz of event rate.

Thus, even the total expected rate of ∼0.29 Hz of in-spill physical events is dominated by cosmic-background events and decreasing this background contribution is of utmost importance.

7.2 Trigger logic and its hardware implementation

The main goal of the ICARUS trigger system is to activate the data recording by all the detector subsystems (PMTs and TPC wires already now, CRTs after their commissioning) when conditions specified by the trigger logic are fulfilled.

Two types of trigger logic, the most relevant for physics, have been developed up to now: Majority and MinBias. The Majority trigger initiates the readout of the event in the presence of the coincidence between a defined sequence of PMTs with scintillation light signals above a defined threshold (called majority or trigger primitive and described in Section 7.2.2) and a spill of the BNB or the NuMI beam. The MinBias trigger, also called the “spill-only trigger”, begins the readout of the event in the presence of the beam spill without the request for accompanying scintillation light signal. For example, the MinBias trigger can be used to test the trigger efficiency.

The ICARUS experiment at Fermilab is at its early stage, so the trigger is still under development. However, both trigger types have already been tested during the trigger commissioning with the beams in spring 2021, the first period of physics data taking (RUN0) in June 2021 and trigger commissioning with only cosmic rays in summer 2021. The POT collected during the RUN0 was 27.8×10^{18} for the BNB beam and 52.0×10^{18} for the NuMI beam, with 95% data taking efficiency in both cases [152].

The ICARUS trigger system as a whole and the PMT-TRIGGER system are shortly presented in the following two subsections.

7.2.1 Trigger system overall architecture

The primary ICARUS trigger, which is the Majority trigger, is based on two signals, PMT-TRIGGER and GLOBAL-TRIGGER, as shown in Figure 7.1. The PMT-TRIGGER signal appears when the requirement concerning the majority condition of a defined PMT sequence with scintillation light signals above a defined threshold is fulfilled. The GLOBAL-TRIGGER signal appears when PMT-TRIGGER is generated in coincidence with the BNB/NuMI beam spill. The beam arrival time for both beams is determined based on the early warning signals for proton extractions transmitted on the White Rabbit[1] network [153] and corrected for the delays due to the time for protons on target and the time of flight of neutrinos from the target to the ICARUS detector.

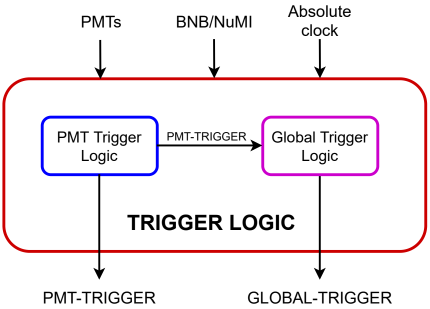

Figure 7.1: Trigger logic at the ICARUS detector. Figure reproduced from [5].

The most important gate signals for the ICARUS trigger system are the *beam spill* gate marking the BNB and NuMI spills (1.6 μs and 9.5 μs, respectively) and

---

[1] The White Rabbit, deployed for the entire SBN program at Fermilab, is an extension to Ethernet technology that allows for synchronisation of remote devices within one nanosecond.

the *enable* gate of ±1 ms around the *beam spill* gate to search for PMT majorities to generate the PMT-TRIGGER signals.

The full trigger logic is handled by the National Instruments (NI) trigger crate, presented in Figure 7.2. Its main components and their functions are:

- SPEXI board: receives the beam early warning signals for a proton extraction, transmitted on the White Rabbit network and activates the trigger system by initialising the appropriate gate signals, e.g., *enable* gate and *beam spill* gate.
- Two 7820R FPGA PMT Trigger boards, one per ICARUS T300 module: generate the PMT-TRIGGER signal based on PMT majorities associated with the 2 ms *enable* gate. They are also used to generate external signals to the PMT digitisers for the PMT waveforms recording.
- 7820R FPGA Global Trigger board: combines the PMT-TRIGGER with the *beam spill* gate signals from SPEXI to generate a GLOBAL-TRIGGER signal; the CRT signal is planned to be added later for the global trigger evaluation.
- Real Time controller, integrated with the crate: manages the communication between SPEXI, FPGAs and the DAQ system, such as monitoring available buffer space and generating veto instances.

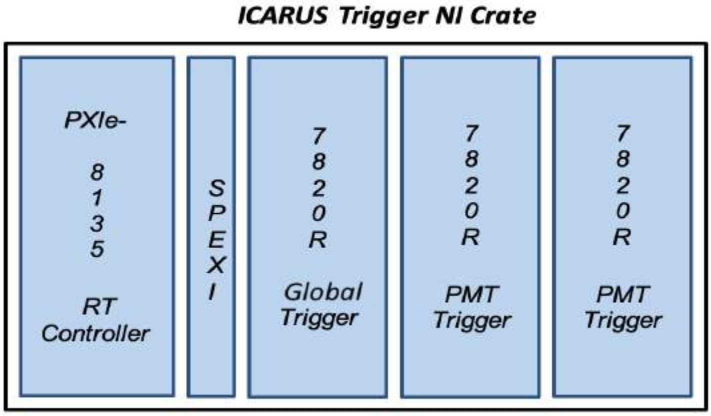

Figure 7.2: National Instrument (NI) crate for trigger system components. Figure from [5].

7.2.2 PMT trigger

The PMT trigger layout is illustrated in Figure 7.3. One can see that the two T300 modules are independent, so the PMT-TRIGGER signal is generated for each of them separately. Thus, it may happen that for some beam spills, the GLOBAL-TRIGGER is generated only for one T300 module.

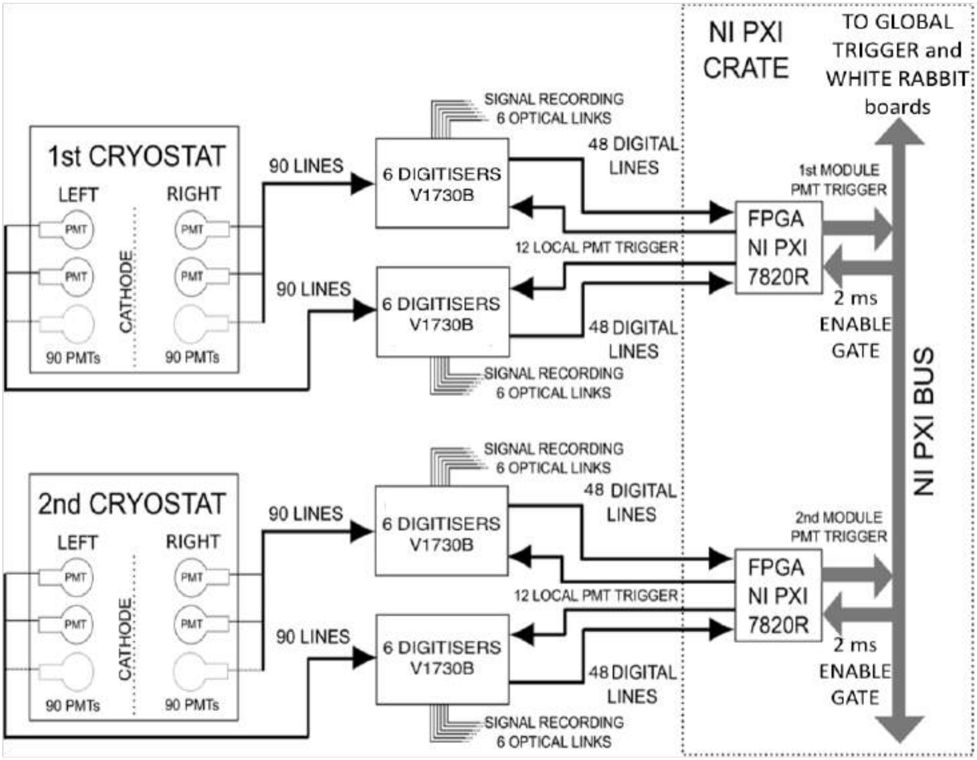

Figure 7.3: The schematic representation of the PMT trigger layout. Figure reproduced from [7].

As presented in Figure 7.3, the 90 PMTs of each TPC are directly connected to 6 CAEN V1730B boards, with 16 channels each. The boards play a double role. They provide the sampling of the PMT signals (500 MS/s, 14-bit resolution), making them available for recording the PMT waveforms through dedicated optical links. They also discriminate the PMT output signals in the Low Voltage Differential Signaling (LVDS) standard[2]. The LVDS signal is a square pulse generated over two inputs

---

[2] LVDS standard allows for high-speed, digital transmission of one bit at a time over two inputs (differential).

every time, one or both of them, depending on the applied logic (OR or AND, respectively), cross a predefined discrimination threshold.

In the case of ICARUS, the two inputs for the LVDS signal, which is 200 ns long, correspond to output signals of a pair of PMTs. An applied pairing scheme of adjacent PMTs into OR/AND logic gates is illustrated in Figure 7.4. It results in 8 LVDS outputs for a set of 15 PMTs (seven pairs and one unpaired PMT) connected to a single V1730B board.

The discrimination threshold of the PMT output signal is configurable and is optimised to ensure the full detection efficiency of neutrino interactions and cosmic events with energy down to 50 MeV in the whole detector active volume. It also helps to decrease the number of spurious signals due to the electronic noise and the ^{39}Ar radioactivity. For example, during RUN0, the discrimination threshold was set at 48 mV (8 photoelectrons), and the OR logic was applied to the PMT pairs.

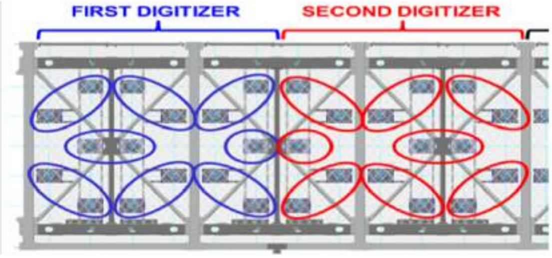

Figure 7.4: The PMT pairing scheme. The PMTs are arranged in groups of 15 that are connected to the same V1730B digitiser board. The hollow ellipses show the pairing system of adjacent PMTs. This pairing scheme means seven pairs and one unpaired PMT per digitiser, but all of them are referred to as pairs for uniformity. Figure from [5].

Due to the low energy of BNB and off-axis NuMI beams, neutrino interactions are expected to be spatially confined in a small section of the detector. From the simulation studies, it was concluded that neutrino interaction contained in the ICARUS active volume covers a section of 30 PMTs in case of CC interactions and 15 PMTs in case of NC interactions. As shown in Figure 7.4 this is taken into account by the longitudinal division of the TPC detectors into six sections, each 3 m long, corresponding to 15 PMTs connected to the same digitiser.

Since 8 LVDS outputs are available for each V1730B board, there are 48 digital LVDS outputs in total for each TPC. The number of the LVDS signals above the discrimination threshold is usually much smaller than the number of available LVDS outputs.

The generated LVDS signals from two TPCs belonging to the same T300 module are sent to this module's programmable FPGA trigger board. The unpaired LVDS signals, corresponding to two neighbouring PMTs, are coupled by the FPGA. Based on the received LVDS signals, a PMT majority is calculated. The PMT majority is defined by the number of LVDS signals occurring in coincidence within 150 ns inside the 2 ms long *enable* gate. When this number is higher than a predefined majority value, set in the trigger logic, the PMT-TRIGGER signal also called trigger primitive, is generated. For example, during RUN0, at least 5 LVDS signals generated in a 6 m slice inside one T300, i.e., corresponding to two pairs of V1730B boards, each pair serving one TPC, were required to generate the PMT-TRIGGER signal. During the entire *enable* gate, there could be several PMT-TRIGGER signals generated.

The PMT-TRIGGER signals are sent to the global trigger FPGA, and a check of the coincidence with the BNB or NuMI *beam spill* gate is performed. If the coincidence occurs for one of the PMT-TRIGGER signals, the GLOBAL-TRIGGER signal is generated.

Based on the MC simulations and initial tests performed at CERN, various trigger algorithms have been implemented in the FPGA units, tested and tuned, taking into account the noise in the detector.

At present, data collected in 2021 within the SBN program are the main source of information for further improvement of the ICARUS trigger.

7.2.3 Relation between trigger signals and data recordings

The choice of ±1 ms for the *enable* gate around the *beam spill* gate is dictated by the detector physics. The scintillation light and ionisation electrons are generated along the charge particles' tracks at any time such particles appear in the active LAr volume of the ICARUS detector. For tracks at the TPC cathodes, 1 ms is needed for ionisation electrons to reach the TPC anode wires. This determines 1 ms time reserved for the readout of ionisation electrons from the entire TPC following the *beam spill* gate.

Because of the cosmic rate of the order of 10 kHz, an average of ten tracks related to the cosmic muons is expected during the TPC 1 ms readout time. In the ideal case of a perfect trigger logic, the PMT-TRIGGER signals should be generated for all these tracks with timestamps precise to the level of 1 ns. To guarantee a safety margin for the assignment of scintillation light signals to tracks appearing during this 1 ms, the PMT activity recording starts 1 ms before the *beam spill* gate, resulting in a 2 ms long *enable* gate.

At present, once the PMT-TRIGGER signal is generated in the FPGA board of a T300 module, it is sent to all its 12 digitisers to start the waveform recording for all PMTs of this module. In the future, only the PMT-TRIGGER signal generated during *beam spill* gate will be sent to all the 12 digitisers, while for PMT-TRIGGER signals generated during *enable* gate only the digitisers directly involved in their generation will be triggered. During RUN0, each of the PMT waveforms collected had the readout length of 30 μs Ref. [152], but ultimately the 10 μs readout length should be used.

An example of *enable* gate with several PMT-TRIGGER signals around the BNB *beam spill* gate is shown in Figure 7.5. The time profiles of the scintillation light signals collected during the 30 μs around the expected BNB and NuMI *beam spill* gates are shown in Figure 7.6. Data come from RUN0. Spill profiles of both beams are very well reproduced.

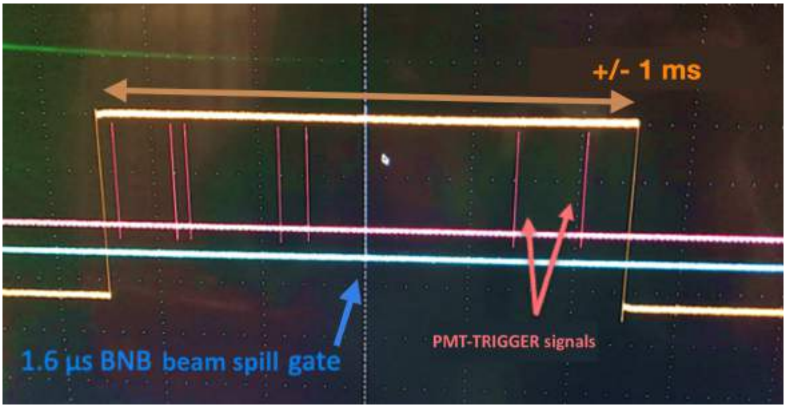

Figure 7.5: An example of *enable* gate, marked by the orange line, with several PMT-TRIGGER signals, marked by the pink vertical lines, around the BNB *beam spill* gate, which is marked by the blue vertical line. Image credit: Andrea Scarpelli.

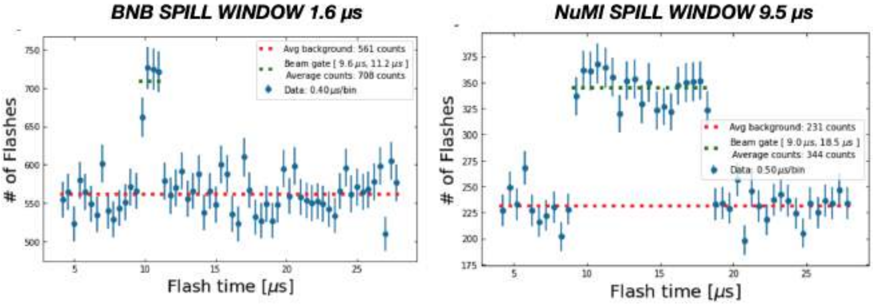

Figure 7.6: Beam profiles based on trigger tests during RUN0. An excess of the PMT light signals in correspondence with the 1.6 μs BNB *beam spill* gate (*left*) and the 9.5 μs NuMI *beam spill* gate (*right*) is observed. Image credit: Andrea Scarpelli.

When the GLOBAL-TRIGGER signal is generated, the TPC data from the anode wires are recorded during 1 ms. At the end of *enable* gate, the TPC 1 ms long image as well as PMT recordings (with their timestamps) corresponding to all PMT-TRIGGER signals issued during 2 ms long *enable* gate are written down on the disk for further off-line analyses. This set of data should help the assignment of the t_0 time values to the tracks in the TPC and the identification of the track or tracks which occurred during the *beam spill* gate and generated the GLOBAL-TRIGGER signal.

7.3 Present and future developments

The trigger system is rapidly evolving. After validation of the present trigger, more advanced triggering can be implemented, based on the simulations and tests guidance. The experience gained during the 2021 running is also very important.

7.3.1 PMT trigger improvements

Two possible improvements, aiming at the background reduction, have already been considered.

At the second level trigger, the collected event sample can be quasi-online filtered out by exploiting the BNB structure of the 1.6 μs spill with 81 bunches of 2 ns FWHM, $\sim$19 ns apart (as presented in Section 4.2.1), to reject cosmic triggers occurring between bunches by reconstructing the actual event interaction timing with the PMT system. This improvement requires a precise PMT timing calibration and good knowledge of the scintillation light propagation in LAr. The former requires defining the PMT delays that may vary in time due to temperature excursions, power supply variations or other reasons. The latter must be determined through a reliable measurement, as presented in Section 8.4. The timing performance can be evaluated by delivering a fast calibration pulse to each PMT channel. During the timing calibration with the laser, the repetition of which depends on the stability of the whole light detection system, a table with the resulting variation of the PMT delays will be written. This table will be then used to make the appropriate correction during the second level trigger. Accounting for $\sim$3 ns resolution in the event time measurement a cosmic background rejection factor of two can be conceived at 90% CL.

Another improvement assumes that the PMT trigger logic can be complemented by exploiting not only the individual PMT signals, but also the analogue sum of a certain percentage of signals of the 15 PMTs in 3 m long sections. For this purpose, signal splitters and analogue adders will be included in the trigger scheme. Each splitter will leave almost unaffected individual signals sent to the digitisers (90% signal amplitude on 50 Ω impedance) while summing up the remaining 10% of signal amplitudes of 15 PMTs of one section. Each analogue sum will be discriminated at a proper discrimination level intended to preserve the neutrino interaction detection efficiency unaffected, but reducing trigger rate due to the electronic noise and the radioactive ^{39}Ar contamination in the detector. The discriminated outputs will be then included in the trigger logic for further signal processing (by FPGAs) and the GLOBAL-TRIGGER signal generation.

A prototype splitter board with 10 channels, realised in the NIM standard[3] electronic assembly, has been implemented and tested at the CERN test facility (see Section 8.2.4). A set of 6 boards with 15 channels each (for one TPC chamber) has been produced and installed during summer 2021 at Fermilab. They are implemented in the VME standard[4] electronic assembly.

Additional enhancement of the trigger could be the offline selection of neutrino interaction events using machine learning techniques. A suitable tool using low-level timing information from the PMTs is already being developed by me and two collaborators and the first results as well as the methodology are described in Chapter 10.

7.3.2 Combining PMT, CRT and TPC

Following the commissioning of the external CRT system, one can develop an initial rough event reconstruction in a second level trigger, rejecting additional cosmic muons by exploiting the time-of-flight information, provided by CRTs and PMTs. Installation of all CRTs should be completed by the end of 2021. Dedicated simulations, including the PMT time resolution and the spatial and timing resolution of CRTs, are being accomplished to check the performance of the trigger layout with CRTs included.

7.4 Data volume

Data from the detector, consisting of waveform information from 53,248 TPC wires and several PMT recordings, as well as charge information from particles striking the CRT system, are collected and combined by the data acquisition system, based on the ArtDAQ [154] software framework. They are written to local disk storage at the detector site. The data is dominated by the size and number of the waveforms from the TPC wires, and with compression, it is approximately 70 MB per event if both modules provide triggers.

Along with collecting data from the BNB and NuMI neutrino beams, out-of-spill data will be collected in-between neutrino beam spills and in periods of no neutrino beam to obtain a sample of cosmic-ray-induced events to study cosmogenic backgrounds. It is expected that if the final trigger rate is between 0.5 - 1 Hz on average during continuous operation of the experiment, the data throughput will be ∼35 - 70 MB/s, and total data volume approximately 1.1 - 2.2 PB/year.

---

[3] The Nuclear Instrumentation Module standard specifies mechanical and electrical terms for electronics modules used in experimental particle and nuclear physics.

[4] The VME (Versa Module Eurocard) standard is a communication system specification for data transfer between components inside a computer or between computers that characterises the electrical and mechanical system to design devices that will reliably and unambiguously communicate with other VME boards to optimise the cost and performance without affecting compatibility.

Chapter 8

Measurements at the LAr test facility at CERN

The hardware realisation of the ICARUS trigger system, described in Chapter 7, required extensive tests of the trigger electronics, the programming of suitable logic in FPGAs and integration of the whole readout system. Since the ICARUS trigger system is based on the LAr scintillation light, a very important test concerned the PMT system performance in terms of the trigger efficiency and timing resolution, with a view to its application in the ICARUS detector as part of the SBN program.

To facilitate tests of the ICARUS scintillation light collection system and the development of its trigger system before the detector installation at Fermilab, a liquid Argon test facility with ICARUS-like electronics chain and ICARUS photodetectors has been built at CERN, in addition to the test setups described in Chapter 6. The test facility is described in Section 8.1, while tests, which were the main task of this facility, are described in Section 8.2. Nevertheless, the test facility was also used to perform two other tasks related to the understanding of liquid Argon as a scintillation medium. The first one was related to the ^{39}Ar contamination studies and is described in Section 8.3. The second task aimed at measuring the velocity of scintillation photons in liquid Argon. Two methods were adopted for this task and are described in Sections 8.4 and 8.5. In addition, studies of design alternatives with different wavelength shifters to improve the light yield and its readout have been performed using a 50-litre liquid Argon TPC at CERN and are described in Section 8.6. Apart from the direct needs of the ICARUS light and trigger systems, all the above studies provide important information for theoretical models describing the propagation of scintillation light in LAr and are of interest for other experiments searching for rare events like neutrino and dark matter interactions.

This chapter is based on several publications [7, 8, 9, 10] that are co-authored by me. My contribution concerns participation in: the installation of the system, monitoring the facility, performing tests and their data analysis, and interpreting the obtained results.

8.1 Experimental setup

The LAr test facility was operating at CERN since August 2018 until September 2019. Its photograph and the schematic drawing are shown in Figure 8.1.

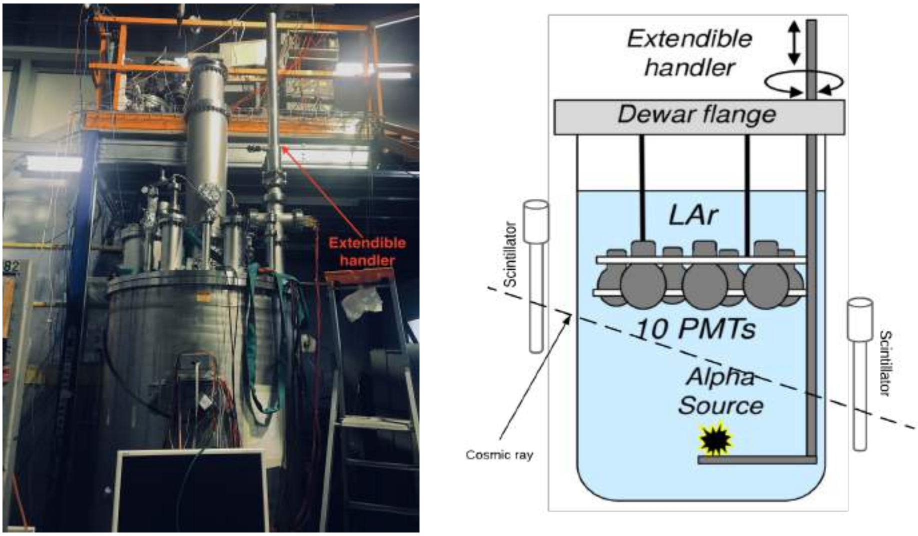

(a) The photograph of the cryostat.

(b) The schematic picture.

Figure 8.1: The photograph of the LAr test facility at CERN (8.1a); the schematic drawing of the cryostat with 10 ICARUS-like PMTs immersed in LAr and the external cosmic-ray trigger based on scintillation counters (8.1b). Figures from [9].

The base of the LAr test facility consisted of a ∼1500-litre double-wall, vacuum-insulated cryostat, approximately 2 m high, with 112 cm external and 96 cm internal diameter as presented in Figure 8.1a. The cryostat was filled with pure commercial liquid Argon (^{40}Ar), certified to have purity better than 1 ppm of O_2 equivalent. During standard operation, the system ran in an open loop, i.e., keeping it in over-pressure with respect to the environment and allowing LAr to evaporate.

Inside the cryostat, there was a light detection system installed, as illustrated by a schematic drawing in Figure 8.1b and a photograph in Figure 8.2. It was based on 10 Hamamatsu R5912-MOD PMTs with 8" photocathodes, among which 6 were coated with ∼200 μg/cm^2 of TPB, a wavelength shifter for detecting the 128 nm VUV LAr scintillation light, while 4 remaining ones were left without a wavelength shifter to detect the visible photons only. For calibration purposes, the light detection system was also equipped with a laser system and optical fibres directed to the PMT photocathodes.

The system was completed with external plastic scintillation counters that allow selecting cosmic-muons crossing the cryostat. In addition, the facility was supplemented with an extendible handler (see Figure 8.1) with custom-made mechanical support for tests with a radioactive source.

Figure 8.2: The 10 PMTs that formed the light detection system for the LAr test facility at CERN. The number of PMTs with TPB coating has been reduced to 6 replacing 4 PMTs with PMTs without TPB coating. Aluminium screens have been installed to isolate the PMTs with the TPB deposition to limit the optical cross-talk caused by them. Figure from [8].

8.2 Small-scale measurements for the SBN program

The primary task of the LAr test facility at CERN involved tests of the new PMT and trigger electronic components and the implementation of the new data acquisition (DAQ) system to define the correct electronic synchronisation and the DAQ timing as required for the ICARUS running at Fermilab. It has also been used to develop the PMT calibration and equalisation procedures, evaluate background and electronic noise, and carry out preliminary studies on the trigger logic.

8.2.1 Tests of the PMT readout boards

As a first step, the PMT readout boards CAEN V1730B have been installed. As described in Chapter 7, these new readout boards perform the PMT signal recording and generate discriminated digital outputs for trigger purposes. The signals from 10

PMTs digitised by two CAEN boards (5 PMTs per board) with signal sampling at 500 MS/s, 14-bit resolution and 2 V dynamic range were connected through dedicated CONET2 A3818, 1.25 Gb/s bandwidth optical links (one per V1730B board) to the acquisition computer. First checks aimed at understanding the PMT signal recording, and the results obtained with random trigger data at 2.5 Hz (Figure 8.3) showed that the CAEN V1730B boards provide a successful signal recording. Since the PMTs were kept in conditions of total darkness, by covering the dewar with its cap, the PMTs without the wavelength shifter coated on the photocathodes detected a very small signal with respect to the PMTs with the wavelength shifter.

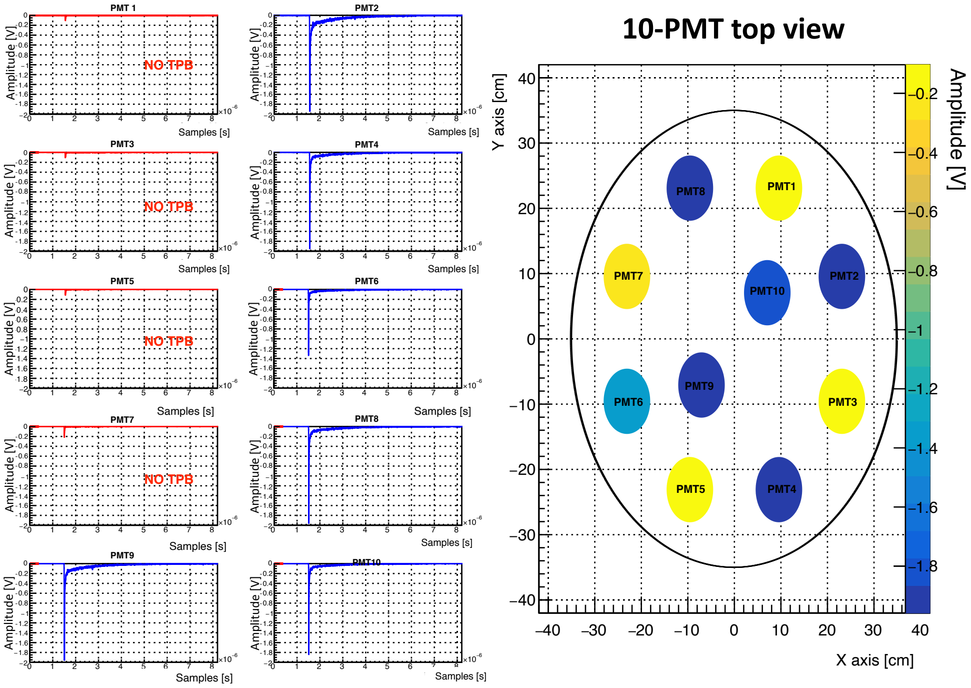

Figure 8.3: An example of a random trigger event recorded by 10 PMTs. The PMT signals from PMTs without TPB are marked in red, and the signals from PMTs with the TPB coating are marked in blue. The plot of the PMT positions in 2D (top view) and their signal amplitudes in volts is shown on the right.

The random trigger data at 2.5 Hz was also used for the determination of the noise at the input of the CAEN modules. After internal calibration (according to the procedures indicated by CAEN) a noise with RMS of ~3 ADC counts corresponding to 0.3 mV was evaluated (1 ADC count = 2 V/(2^{14}-1) = 122.078 μV).

8.2.2 PMT gain equalisation and timing calibration

The most important parameters of PMTs, such as their gain and timing characteristics, are subject to variation in cryogenic temperatures, as observed from the PMT test campaign described in Chapter 6. Therefore, a gain equalisation and timing calibration of 10 PMTs after their immersion in LAr were essential for performing further measurements using the test facility.

Gain equalisation and time calibration were performed using a solid-state fast laser source (Hamamatsu C10196), injecting light pulses ($\lambda = 407$ nm, width = 60 ps) into a multimode 50 μm optical fibre. The laser was set at a very low intensity of 30 - 50 photons per pulse. The number of photoelectrons was estimated from the pulse height variance of the laser (measured by the oscilloscope), and the charge per photoelectron was calculated for each PMT high voltage setting. The approximate laser calibration resulted in the gain equalisation of 20%. The PMT HV settings corresponding to G = 2.5×10^6, which provides an amplitude of 2.2 mV for a single photoelectron are shown in Figure 8.4. They were used in all the measurements described in this chapter unless another value of the gain is explicitly stated.

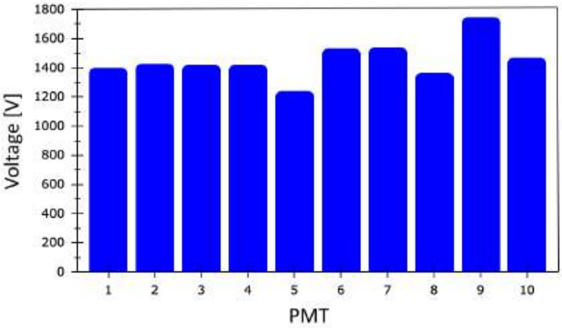

Figure 8.4: The histogram of PMT voltage settings to obtain gain G = 2.5×10^6.

Timing characteristics of the PMT pulses were checked for a very high and a very low laser intensity. At the very high laser intensity, the PMT pulses were mostly uniform, with a broad top likely due to the laser pulse width and saturation. At higher power, the laser pulse is determined by the shape of the current pulse applied to the diode. At the very low laser intensity, all the PMTs give 30 - 50 photoelectrons with similar pulse height distributions. At lower power, there are four constants to consider: turn-on time of the laser, the rise time of the PMT, turn off time of the laser, fall time of the PMT. It was found that the relative timing calibration has been possible for each voltage setting with a time resolution better than 1 ns for all 10 digitiser channels. An example illustrating this resolution for one of the PMTs is presented in Figure 8.5.

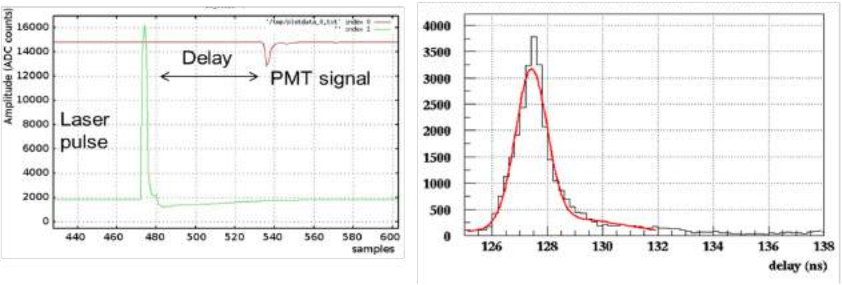

Figure 8.5: Example of measured time delay between the PMT response to laser illumination and the laser pulse ($left$). Due to the multiple sampling of the input pulses, it was possible to reconstruct the leading edge of the PMT signal and evaluate the time response at 50% of its amplitude. The time delay distribution for one PMT illuminated with a laser multiple times is shown on the right. The resolution resulting from a Gaussian fit $\sqrt{\sigma^2_{Laser} + \sigma^2_{PMT}} = 0.67$ ns is better than the digitiser sampling time of 2 ns. This figure was published in Ref. [8].

8.2.3 Tests of the trigger electronic components and checks on trigger efficiency

In order to perform the test of electronics relevant for the ICARUS trigger system, the test facility at CERN was equipped with electronics items identical to those installed in the final configuration of the ICARUS detector at Fermilab. A basic scheme of the PMT-TRIGGER electronics chain and the PMT DAQ at the test facility is shown in Figure 8.6.

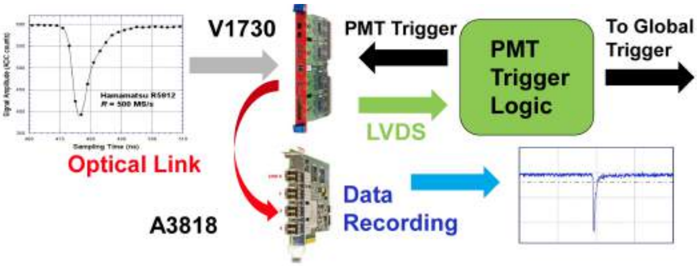

Figure 8.6: The CERN test facility PMT trigger and DAQ scheme. Figure from [7].

The PMT data readout was performed by CAEN V1730B. Recorded signals were then transferred through the optical links A3818 to the data storage. The V1730B board also generated a set of discriminated output signals (LVDS), which were input to the programmable logic unit FPGA 7820R, following the trigger system description from Chapter 7.

In order to test the two available 7820R FPGA PMT trigger boards, signals from 10 PMTs were analysed by each of them one by one. They were programmed with the LabVIEW FPGA tools to produce output signals corresponding to various multiplicity conditions, in either OR or AND logic, controlled by settable parameters, described in Chapter 7, adaptable to various possible trigger sources (beam, cosmic-rays, calibration). An example of trigger logic LabVIEW FPGA programming for 10 PMTs at the CERN test facility is shown in Figure 8.7.

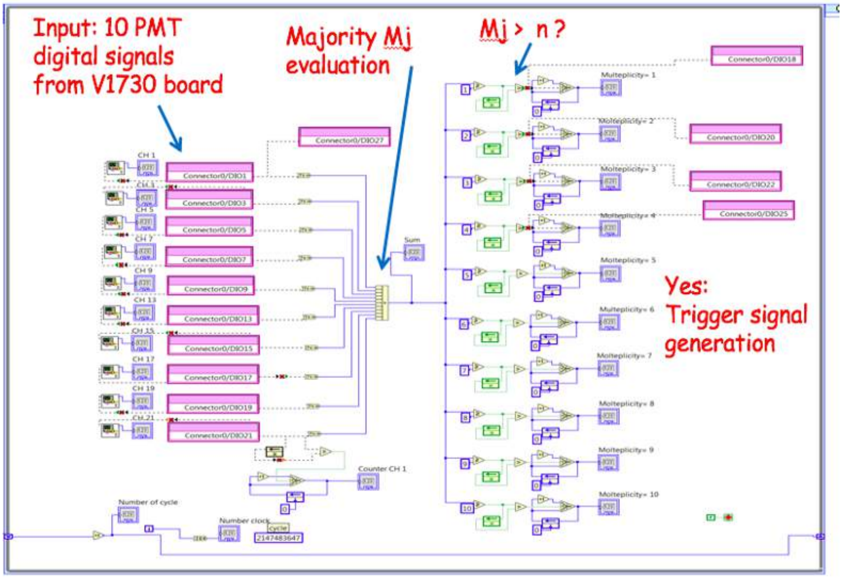

Figure 8.7: An example of the LabVIEW code illustrating the implementation of the PMT majority logic using the LVDS inputs at the CERN test facility. Based on the input of 10 PMT digital signals and the required value of the majority parameter (M_j), the trigger signal is generated, provided that the number of true input signals (n) is bigger than M_j. Figure from [5].

Figure 8.8 shows the recorded trigger rate as a function of the number of PMTs with the signal above the discrimination threshold (majority) for four different threshold settings. As expected, for each value of the discrimination threshold, the trigger rate decreases with an increasing value of the PMT majority. For each value of the majority, the trigger rate decreases with an increasing value of the discrimination threshold, the effect being stronger for the low values of the majority at lower values of the threshold, while for high values of majority at higher values of the threshold.

For the ICARUS detector operating at the surface at Fermilab, the trigger is

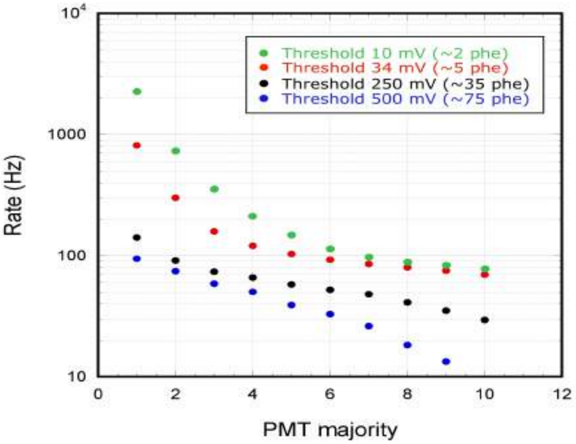

Figure 8.8: The recorded trigger rate with four different discrimination thresholds as a function of the PMT majority.

given by a signal from the PMT system in coincidence with the *beam spill* gate. For the tests at CERN, the signal from cosmic muons triggered by the coincidence of the external scintillators was used instead. Figure 8.9 shows an example of the detection efficiency of a horizontal muon crossing the system for various combinations between the PMT signal threshold and the PMT majority. The results show reasonably high detection efficiency in all the cases, pointing to a good functionality of the trigger electronics components and to a properly set-up trigger logic.

Direct conclusions related to the trigger efficiency for the ICARUS detector at Fermilab cannot be drawn from the measurements at CERN because of the completely different experimental conditions in the two cases.

8.2.4 Additional tests

Analogue adders

As already mentioned in Chapter 7, due to the low energy of the BNB and off-axis NuMI beams, the neutrino interactions are expected to be spatially confined in a small section of the detector corresponding to 15 - 30 fired PMTs. Therefore the linear analogue sum signal of 15 PMTs in 3 m detector slices can be included in the trigger scheme to help further the identification of the ν interactions and the reduction of trigger rate due to stochastic noise and ^{39}Ar background.

The 10-channel analogue adder scheme, developed for the test setup at CERN, is presented in Figure 8.10. It consists of two independent branches, each summing up signals from 5 PMTs and splitting the input signal in a way that 95% will be

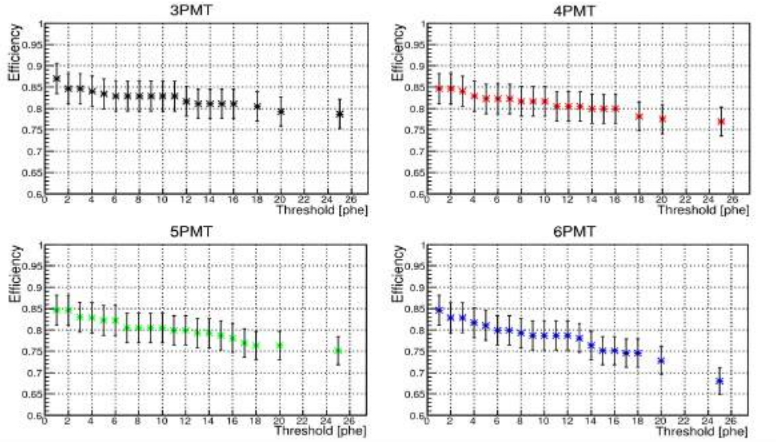

Figure 8.9: Trigger efficiency of the horizontal muons detection for four different PMT majorities as a function of the discrimination threshold (in photoelectrons).

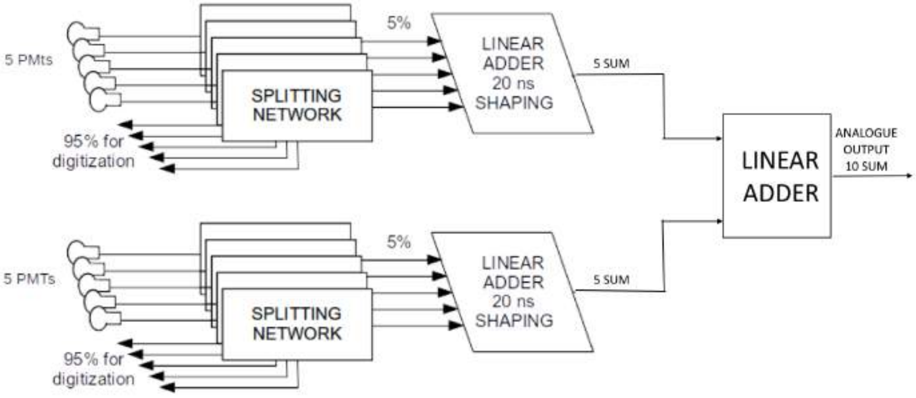

Figure 8.10: The schematic drawing of the PMT signal adder prototype.

available for the digitisation and 5% for the final analogue sum of 10 PMTs from both branches. The resulting signal is then integrated over 20 ns to overcome the time spread among different input channels.

The prototype of this 10-channel adder has been realised in NIM standard and successfully tested with the 10 PMTs at the CERN test facility.

For the ICARUS detector operation at Fermilab, the final configuration of the analogue adder will consist of three independent branches. A different splitting of the PMT signals than the one used at CERN will be applied, namely summing up five input signals with 10% amplitude and returning the 90% amplitude for data recording. The three sums coming from the three branches will be added to give a 15 PMT analogue sum.

Initial system synchronisation

The timing synchronisation of the whole ICARUS detector and the handling of the beam extraction messages is performed by the SPEXI board, which is a part of the National Instrument (NI) trigger crate, as described in Chapter 7.

The primary purpose of the synchronisation test at the CERN test facility was to check that the signals' transmission works and that the time synchronisation of the readout electronics of the TPC wires (CAEN 2795[1]) and the PMTs (CAEN V1730B) is guaranteed. Therefore, it was necessary to check that the SPEXI board reads and sends information correctly and that synchronisation between the readout boards can be ensured. The distribution of the trigger signals has been set up to the SPEXI board from its front panel and verified that the SPEXI properly encoded them into the Timing and Trigger Link (TT-Link) signal. The TT-Link signal is used to distribute the sampling clock and a set of real-time commands to all the TPC readout electronics boards. The test of the TT-Link distribution from SPEXI to the TPC boards, using the CAEN DAQ code, has been successfully managed.

The next step to be performed was a synchronisation of clock distribution to PMT and TPC readout boards. A straightforward configuration of triggering both the TPC wires and PMTs simultaneously with an independent readout for each system has been applied. This configuration allows basic tests of internal timestamps. The time between events for three time intervals with different trigger rates is shown in Figure 8.11. The event frequency was increased in order to check if the synchronisation is still ensured, which is manifested in the plot by the presence of the steps. It can be seen that increasing the trigger rate scales up the number of events per second, resulting in the increase of black dots populating the corresponding step.

The initial system synchronisation tests performed at CERN were successful and turned out to be valuable for SBN.

8.3 Argon contamination studies

One of the primary sources of low energy background in LAr TPC is the contamination of ^{40}Ar with a radioactive ^{39}Ar isotope, which undergoes $\beta-$decay to ^{39}K with an endpoint at 565 keV. The measured activity of ^{39}Ar in LAr is 1.01 ± 0.08 Bq/kg

---

[1] The readout of the TPC wires is not the subject of this thesis and thus will not be further discussed.

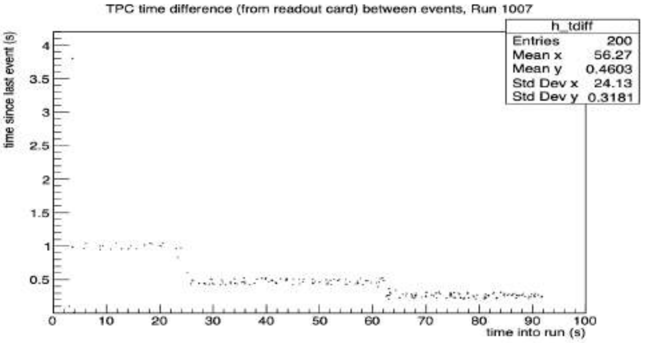

Figure 8.11: Internal timestamps. The trigger rates were changed during the run, which causes the steps in the plot.

of natural Argon, and a concentration of $(8.0 \pm 0.6) \times 10^{-16}$ g(^{39}Ar)/g(^{nat}Ar) was evaluated [155].

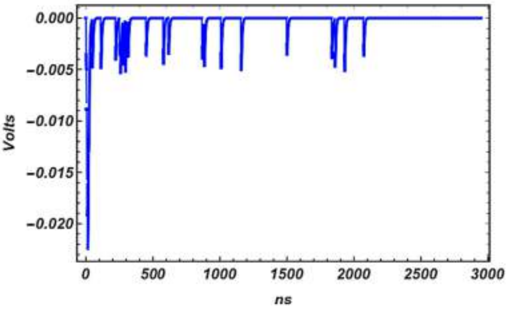

Figure 8.12: Simulated ^{39}Ar pulse, with yield of 10 photoelectrons at 1 m distance from the PMTs, PMT gain equal to 5×10^6 (assuming gain fluctuation = 40%) and PMT pulse parameters τ_r = 1.5 ns and τ_f = 5.6 ns. Figure from [8].

The study of ^{39}Ar-induced events at the CERN LAr facility was performed by applying a random trigger with 1 - 10 Hz rate and excluding PMT signals induced by cosmic rays passing through the two scintillator bars. For the mass of about 1 tonne of LAr inside the facility cryostat, one ^{39}Ar-induced background event per PMT was expected to appear every few milliseconds. The rate of cosmic muons passing the LAr and not passing the scintillator bars was estimated to be 7 to 10 times smaller than the rate related to ^{39}Ar decays.

The measurements were supported by a simple simulation, performed in Mathematica [156], of the test facility geometry, PMT response and the Argon properties, assuming 1Hz/kg ^{39}Ar rate. The model applied to the PMT response simulation is described in Ref. [157]. It implies that the PMT anode circuit may be represented by a simple parallel RC circuit with the anode time constant equal RC. Thus, the PMT signal is described by the function:

$$V(t) = \frac{GNeR}{\tau_f - \tau_r}\left[\exp\left(-\frac{t}{\tau_r}\right) - \exp\left(-\frac{t}{\tau_f}\right)\right], \tag{8.1}$$

where G denotes the PMT gain, N is the number of the photoelectrons emitted by the cathode, e is the charge of the electron τ_r is the PMT rise time and τ_f is the PMT fall time.

In the case of ICARUS PMTs with the anode time constant small in comparison to the scintillator decay time, the leading edge of the pulse has the time dependence determined by this constant and the tail of the pulse has the time dependence determined by the scintillator decay time.

Examples of the simulated ^{39}Ar signal and the measured one are shown in Figures 8.12 and 8.13, respectively. These events were selected to have almost the entire signal registered by a single PMT to facilitate their direct comparison and to investigate the ^{39}Ar background discrimination in potentially the worst case.

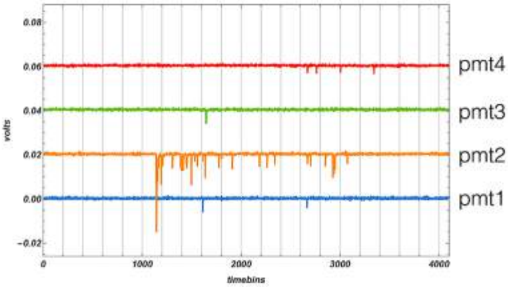

Figure 8.13: A candidate for the ^{39}Ar recorded signal. The vertical axis represents the signal amplitude in volts and the horizontal axis represents the time in nanoseconds. The signal is almost entirely recorded by PMT2 with a very small contribution from PMT4. PMT1 and PMT3 which are without TPB and therefore are not expected to have much pulse height. Figure from [8].

One can see that the simulation correctly reproduces the measured ^{39}Ar pulse distribution. In both cases, the peak corresponding to the fast component and the dispersed peaks coming from the delayed component of the LAr de-excitation have similar amplitudes, corresponding to 6-8 photoelectrons and to single photoelectrons, respectively. They also have similar time ranges of $\sim$2 μs, as expected for the slow component. One should notice that for cosmic muons the photon yields and the corresponding signals are usually higher than for ^{39}Ar.

Moreover, the simulation including neutrino interactions, cosmic muons and ^{39}Ar background [6], shows that a trigger with a majority bigger than two for signals with a discrimination threshold at a level of 5-10 photoelectrons will eliminate the background due to ^{39}Ar without influencing the trigger efficiency for neutrino interactions and cosmic rays down to 50 MeV.

8.4 Velocity measurement of scintillation light photons in LAr

The first measurement of the group velocity of scintillation photons in liquid Argon was performed at CERN using the same dewar and the R5912-MOD Hamamatsu PMTs but in a different configuration [10].

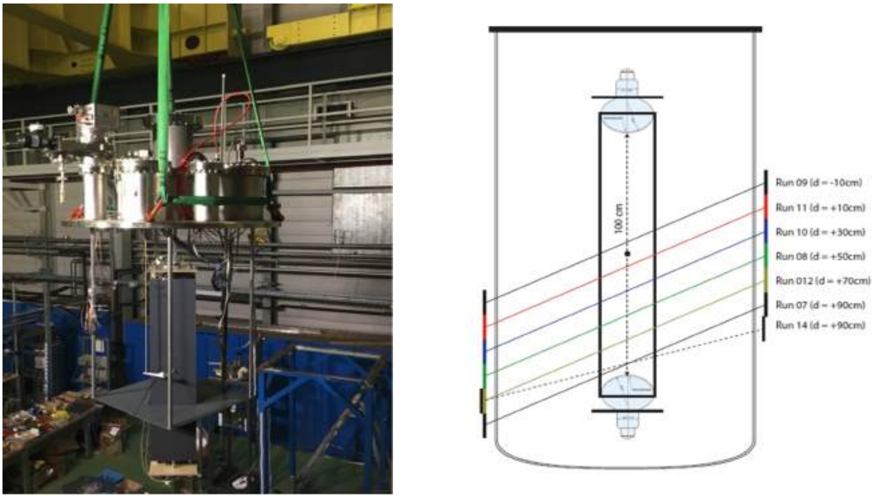

Figure 8.14: The photograph of the experimental setup before the insertion in the LAr (*left*) and the schematic drawing of the setup with the movable trigger system (*right*). The two internal PMTs are located at a distance of 100 cm from each other and immersed in LAr. Outside the cryostat, located symmetrically with respect to its central axis, two scintillator bars (coloured lines) play the role of a cosmic hodoscope and allow selecting cosmic-ray tracks crossing the box at given distances from the internal PMTs. For a given distance, different track slopes can also be selected. Figure from [10].

The experimental setup, shown in Figure 8.14, employed two PMTs immersed in

LAr and positioned facing each other at a distance of 100 cm. An external movable cosmic hodoscope, composed of two scintillating slabs (50 cm × 10 cm × 1 cm), was located symmetrically outside the cryostat, allowing for triggering cosmic muons crossing the dewar at various distances from the PMTs. By measuring the difference in path lengths and in the light arrival time at the PMTs for several positions of the external hodoscope, the scintillation light velocity could be extracted from a simple linear fit.

The system was triggered by requiring a coincidence of the two external scintillators and the two internal PMTs within a 150 ns long window, which resulted in a rate of about 100 events per hour. For each triggered event, waveforms for both internal PMTs were recorded using an oscilloscope with a sampling rate of 5 GHz. The waveforms were recorded during a time window of 5 μs to include most of the LAr scintillation light slow component. An interval of 0.5 μs before the trigger was included in the recorded time window to allow a precise baseline evaluation.

The system was triggered with six different positions of the external cosmic hodoscope, resulting in six propagation path lengths. About 2,500 - 3,000 events were collected for each path length. Data were collected for the entire set of positions for two different track slopes, $\tan\alpha = 0.23$ and $\tan\alpha = 0.39$, corresponding to a vertical mutual distance of 30 and 50 cm of the hodoscope, respectively, but with the same mean distance from the internal PMTs. By comparing the results from these two independent data samples, the stability of the measurements for the amount of light detected by each PMT, contributing to the measurement systematic error, was verified.

The analysis strategy was based on the constant fraction method, because it brings smaller systematic uncertainty than the alternative method based on the arrival time of the first photon. For the constant fraction method, the light arrival time at the PMT was calculated as the time of a given percentage of the maximal signal amplitude for each event. It is worth noticing that the search for a given value of the constant fraction is done both starting from the bottom or the top of the pulse, and only events returning the same time sample for both directions of the search were considered. Through this simple test, most of the noisy events could be removed, leading to the increased precision of the achieved results.

The results of measurement of inverse scintillation light velocity in liquid Argon for the two track slopes using a constant fraction of 50% is presented in Figure 8.15. The two lines, representing the two samples of tracks ($\tan\alpha = 0.23$ and $\tan\alpha = 0.39$) are in very good agreement.

The measurement relies on evaluating two relative quantities, i.e., the difference in time arrival (Δt) of the scintillation photons at the two PMTs and the distance travelled by these photons (Δs). By moving the external hodoscope to a different position, the relative difference in the travelled distance by the photons changes. However, it does not affect any aspect of the inner setup. Therefore, any uncertainty related to the placement of the inner PMTs, affecting the Δs calculation, carries

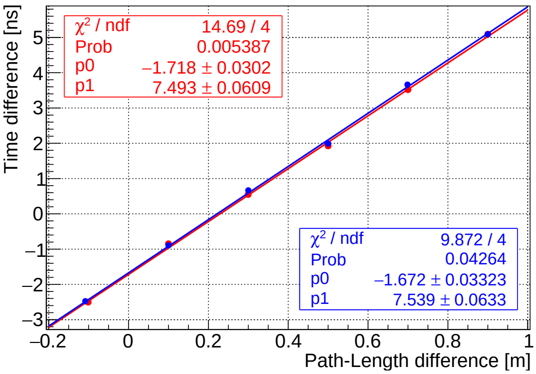

Figure 8.15: The inverse scintillation light velocity in liquid Argon extracted from the two samples of tracks ($\tan\alpha = 0.23$ and $\tan\alpha = 0.39$). The results were obtained using a constant fraction of 50%. Figure from [10].

over to the new data point unchanged. The analogue reasoning is valid for the case of the difference in photon travel time (Δt), which on a single measurement would depend on the actual distance difference covered by the photons and on intrinsic characteristics of the PMTs, like transit time and TPB conversion time. When moving the hodoscope to a new position, the PMTs properties remain the same, and the change in Δt is only affected by the corresponding variation of Δs.

Thus, the inner PMT-related uncertainties can be treated as a constant offset affecting all data points. This offset can be estimated experimentally, but it is entirely irrelevant for the actual measurement of the physical quantity of interest here, extracted from the slope of the linear relation between Δt and Δs. As a result, the only uncertainty influencing the analysis is related to the positioning of the scintillating pads of the trigger system. The error of 0.5 cm is considered in the analysis, given by the achievable precision in the positioning of the external PMTs mechanical support.

Another source of uncertainty stems from the large geometrical cross-section of the scintillation slabs, 50×10 cm^2, which turns into a wide solid angle over which cosmic tracks can be distributed. This is mitigated by collecting and measuring the time difference from a large population of events, whose mean path is well defined from the Gaussian shape of the distribution. It can be further noted that the stability of the obtained velocity result against the change in the track slope selected through the hodoscope proves that such uncertainty is mitigated.

To evaluate possible additional sources of systematic uncertainties, the analysis was complemented by dedicated simulation, which included the PMT geometry and their positions, the cosmic hodoscope, and the monochromatic 5 GeV/c muons generated at the top scintillator slab and directed towards the bottom one. The total scintillation light yield was set to 5.1×10^4 photons/MeV, and the scintillation light spectrum was simulated with a Gaussian shape centred at $\lambda = 126.8$ nm and an FWHM = 7.8 nm. The simulation also introduced Cherenkov and visible light produced by the TPB. The Rayleigh scattering length was fixed to 90 cm. The propagation velocity was estimated according to the sampled photon wavelength. The parametrisation of the refractive index as described in Ref. [158] was applied, and the group velocity was calculated as:

$$\upsilon_g = \frac{c}{n - \lambda \frac{dn}{d\lambda}}, \tag{8.2}$$

where n denotes the index of refraction and λ is the wavelength of the VUV light.

From the simulation studies, it was concluded that the data point having the external trigger positioned near the bottom PMT (i.e., Δs = 90 cm) was affected by significant uncertainties. Thus the extraction of the final velocity measurement was performed, excluding that point from the linear fit. The final value of the inverted group velocity of the scintillation light in LAr was found to be equal to 7.46 ± 0.03 (stat.) ± 0.07 (syst.) ns/m.

The measured velocity was also used to extract the index of refraction n for the VUV light region ($\lambda = 128$ nm, see Section 3.2 for details) in LAr using the Lorentz-Lorenz equation [159] in a dispersive medium, and the Sellmeier coefficients for LAr at 90 K extracted using data wavelength between 350 and 650 nm [160]. The resulting refractive index at 128 nm was 1.358 ± 0.003.

After obtaining the index of refraction, the Rayleigh Scattering length $\mathcal{L}$ could be derived [94, 161]. For a temperature of 90 K and an isothermal compressibility of $2.21 \times 10^{-4}\text{cm}^2/\text{kg}$ [162], the Rayleigh Scattering length $\mathcal{L}$ of 99.1 ± 2.3 cm was obtained for $\lambda = 128$ nm.

8.5 Studies of LAr scintillation light properties with alpha source

An alternative method to measure the velocity of scintillation photons in liquid Argon was developed, making use of the original test setup (see Figure 8.1) and of a radioactive alpha source ^{241}Am, mostly emitting α particles with an energy of ~5.4 MeV. The activity of the source is 39 kBq, and it can withstand the immersion in LAr. Due to the short range of alpha particles in LAr, the light emission can be considered as coming from a point-like source. This isotropic light signal propagates with negligible attenuation through the LAr volume of the test facility. For scintillation photons, which are not absorbed by the detector material, the time and amplitude information remain almost unaffected along their paths to the PMTs of the test facility.

The alpha source, in the form of a 22 mm diameter, 4 mm thick, stainless steel disk with an active surface of ∼2 cm^2 was placed on custom-made mechanical support, as shown in Figure 8.16. The support of hexagonal shape (110 mm width, 60 mm high), made of ABS[2] was 3D printed. Apart from holding the source, it also supported six arrays of silicon photomultipliers (16 Hamamatsu, sensitive to visible light, S12572-050P on each array) used for the data acquisition trigger. Within each array, the SiPMs were connected in a hybrid configuration (4 parallel arrays of 4 units in series) [163]. Each array was coated with TPB to make the devices sensitive to VUV light. The 16-SiPM arrays were electrically coupled in parallel in two groups of 3 arrays to have two independent trigger lines, one of which was used as a backup. The SiPM arrays also provided the t_0 signal for timing studies. A protecting cap (110 mm diameter) with a 40 mm hole was used to shade the SiPM arrays from the direct light produced by cosmic rays in the facility active volume. The hole served as a window for alpha particles emitted from the source, in addition providing their collimation.

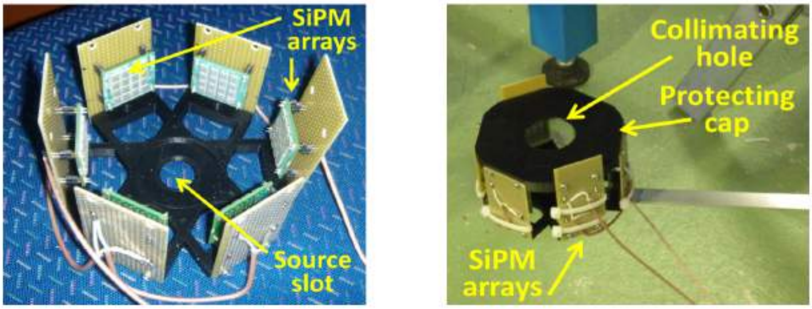

Figure 8.16: The custom-made mechanical structure supporting the alpha source and 6 SiPM arrays that were used as a trigger. Figure from [9].

The extendible handler mounted on the dewar top flange of the test facility permitted the internal translation and rotation of the equipped support. In that way, the distance between the alpha source and the PMT could have been varied in a 0 - 90 cm range. The rotation within 0 - 90 degrees range allowed placing the source under different PMTs.

The signals from the SiPM array and 3 PMTs over a 1 μs window were acquired by an oscilloscope (Tektronix MSO64, 2.5 GHz bandwidth, 12-bit 25 GSa/s). The voltage settings of the PMTs corresponded to $G = 10^7$, while the voltage of the SiPM array was set to 224 V.

The thresholds for the SiPMs and the PMTs were set to discrimination values of

---

[2] The Acrylonitrile Butadiene Styrene (ABS) is a part of the thermoplastic polymers family. It is a material commonly used by 3D printers.

a few photoelectrons. The DAQ trigger was performed by the oscilloscope, requiring a coincidence in the acquisition windows of signals above the thresholds from both the SiPM arrays the PMT positioned above the source.

In each set of acquisition runs, the horizontal position of the source was set centrally below a selected PMT. This central position was kept during the vertical source translation, leading to different values of time differences (t_1 - t_0) between the PMT activation and the SiPM response.

Two different methods were taken into account for the determination of this delay: 1) a constant fraction method, by measuring, event by event, the difference of the sampling points corresponding to a constant fraction (e.g, 50%) of the photomultiplier maximal signal amplitude; 2) a threshold method, by determining for each event the arrival time of the first detected photon, i.e., the intersection point between the baseline and the line best fitting the signal leading edge. For each source position, the distribution of the time differences between PMT and SiPM was obtained. An example of such a distribution for the source-to-PMT distance of 100 mm is shown in Figure 8.17. A slightly asymmetric shape of this distribution with a tail for higher values of time differences is observed. This effect is stronger for more extended distances between source and PMT, where the number of photons hitting the PMT is low. This is due to larger intrinsic timing uncertainties of the PMT small signals. Thus, each distribution is only partially fitted with a Gaussian curve.

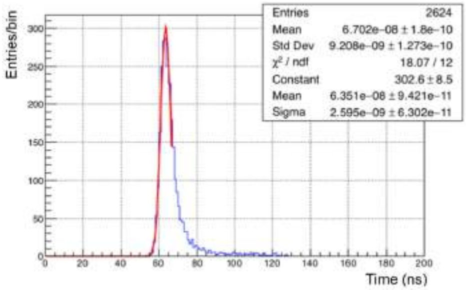

Figure 8.17: The distribution of the time difference between PMT and SiPM responses to the scintillation light induced by the alpha source with a partial Gaussian fit. The distribution was obtained using the constant fraction (50%) method for the source-to-PMT distance of 150 mm. Figure from [9].

The peak values of the distributions of the time difference between the PMT and SiPM plotted as a function of their distance are shown in Figure 8.18. The slope of the straight line fitting the time differences for different source-to-PMT distances gives an estimation of the velocity of VUV photons in LAr.

The resulting linear behaviour of the inverse of the speed of scintillation light in LAr demonstrates the capability of the system to perform this measurement. However, its quantitative interpretation strongly depends on the experimental framework used to determine the time differences. In order to obtain valuable results, knowledge of all the factors that contribute to the experimental uncertainties is required. For this purpose, a complete Monte Carlo simulation of the facility would have been helpful. The precise geometry of the adapted instrumentation, e.g., the shape of PMTs and SiPMs, actual paths of photons in the active volume, interference of visible photons and LAr properties, should have been taken into account. There was not enough time to perform such simulations. In addition, the measurement of the group velocity of scintillation photons in LAr had already been completed using the method described in the previous section. Thus, this study has not been concluded.

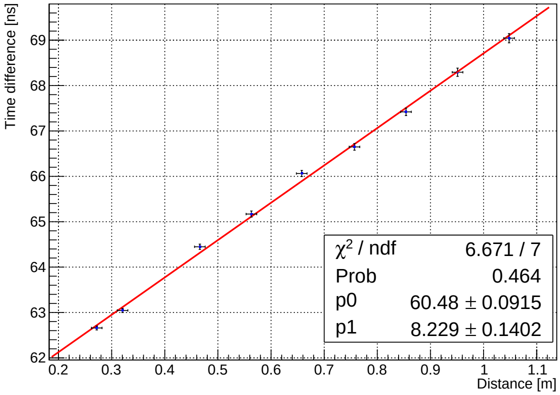

Figure 8.18: Distribution of time difference between PMT and SiPM as a function of their distance.

8.6 Light production study at the 50-litre LAr TPC

Another set of measurements was inspired by the needs of the Proto-DUNE single- and dual-phase LAr detectors [164, 165] operating at CERN. They mostly concerned studies of the effect of LXe doping in the dual-phase TPC and controlled contamination of LAr with N_2 [166], but also included tests of wavelength shifters. I was only involved in the measurements related to wavelength shifters, so I will focus on them.

The measurements were performed using the 50-litre liquid Argon TPC at CERN. The chamber is configured to have a vertical (upward) drift volume and is hosted in an inner stainless-steel cylindrical vessel (60 cm diameter, 100 cm height). The internal dimensions of the field cage are 345 mm × 345 mm. The full drift path (cathode to the first wire plane) is 520 mm long. There are three wire planes, each made of stainless-steel wires with 100 μm diameter and 2.54 mm pitch. The distance between wire planes is equal to 4 mm. The first wire plane encountered by drifting ionisation electrons acts as a shielding Grid for the other two, which are biased to have the second one working in Induction mode and the third one in charge Collection mode. This corresponds to the Grid and the Collection planes biased to ±300 V (negative for Grid, positive for Collection) while keeping the Induction at 0 V. The Induction and Collection wires are at 90° with respect to each other, while the Grid wires are parallel to the Induction wires. A more detailed description of the 50-litre TPC can be found in the Ref. [167].

For this study, the cathode was biased to have an electric field in the drift volume of 500 V/cm; the HV required to achieve this value was set to -27 kV. Three PMTs were installed above the TPC, looking into the drift volume, but only two of them were used to measure the light yield in these tests. The Hamamatsu R11065 PMT with TPB coated window (denoted as *LAr w/TPB*) and Hamamatsu R11410, which was more sensitive to the LXe scintillation light (denoted as *LXe*). The Induction and Collection wires were read out by the CAEN A2795 modules.

Figure 8.19: The photograph of the CERN 50-litre liquid Argon TPC.

The tests concerned studying the wavelength shifter and reflector foil performance applied on the chamber's cathode, including testing the perturbation of the electric field by charging up of the foil. The first run (Run1) was dedicated to the performance of a reflective foil coated with TPB. The second test (Run2) was related to a reflective foil with a polyethylene naphthalate (PEN) sheet placed on top of the cathode. The last one (Run3) was performed with the plain cathode serving as a reference to Runs 2 and 3.

The data were taken with various cosmic-muon trigger configurations. The drift velocities and the electron lifetimes were measured with muons crossing the entire drift distance. The measured electron drift velocities during each test campaign resulted in 0.148 cm/μs, 0.147 cm/μs and 0.150 cm/μs for Run1, Run2 and Run3, respectively. The electric field calculated for Run1 and Run2 based on these drift velocities is approximately 5% less than the nominal value (500 V/cm) of Run3 due to the charge up of the foil.

The single photoelectron responses of the PMTs were continuously monitored during each run and were found to be stable apart from the cool down period and some modifications such as the high voltage changes during Run1.

The electron lifetime measured during Run3 started at ~400 μs with the initial fill and reached a value of 1 ms with recirculation. This trend was also visible for the other two runs. In addition to electron lifetime, the slow component of LAr scintillation was also monitored as it indicates the contamination at ppm level of N_2 in the LAr. The values of the slow components measured with *LAr w/TPB* ranged between 1.4 μs and 1.6 μs.

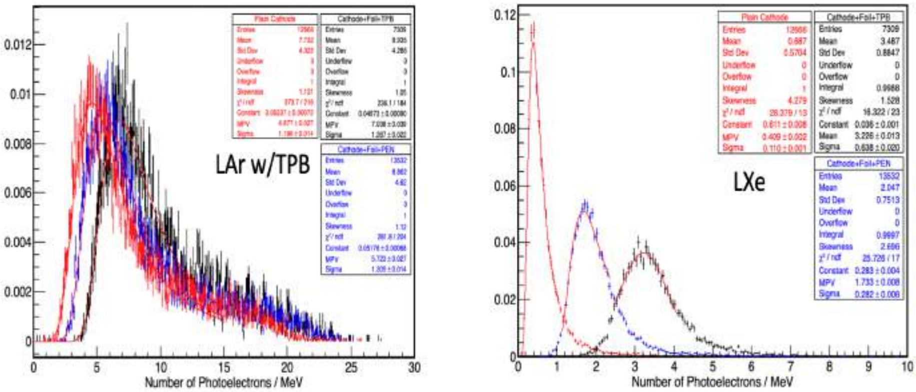

Figure 8.20: The light yield measured with the *LAr w/TPB* (*left*) and with the *LXe* (*right*).

Figure 8.20 shows the light yield measured with the *LAr w/TPB* and *LXe* for the three collected runs. The number of photoelectrons per cm is calculated using minimum ionising particle (MIP) tracks traversing the full drift distance. This was then converted to the number of photoelectrons per MeV, considering an energy loss per MIP of 2.1 MeV/cm. For the measurements with *LAr w/TPB*, the increase in light yield was 17% with PEN and 45% with TPB compared to the plain cathode response. Thus, the relative wavelength shifting efficiency of PEN/TPB is measured to be approximately 38% and is consistent with the recent similar measurements [168].

For the measurements with *LXe*, 86% of the relative increase in light yield with TPB compared to PEN was measured. The unexpected nonzero response of *LXe* with plain cathode is due to the reflections of the light shifted by the TPB coating of the *LAr w/TPB* PMT. The effect of this reflection and the effect of the transmission of visible light through the TPB coating of the *LAr w/TPB* is under investigation with Monte Carlo simulations.

Chapter 9

ICARUS detector simulation and analysis tools

In order to facilitate direct comparison of performances of its three detectors and profit from applying common tools to all of them, the SBN program makes use of LArSoft (Liquid Argon Software) [169] framework. LArSoft is a C++ based e-infrastructure and algorithm set for simulation, reconstruction, and data analysis across Liquid Argon Time Projection Chambers in neutrino experiments at Fermilab. It is built on top of the Fermilab-supported Analysis Reconstruction Tool (art) [154]. It offers a broad set of algorithms and utilities, including those for associated photodetectors and the handling of auxiliary detectors outside the TPCs (CRTs in the case of ICARUS). The LArSoft collaboration maintains the code and implements improvements or new features based on input from LAr TPC experiments.

An overview of the simulation, reconstruction, and analysis tools currently available for the ICARUS detector will be given in this chapter. In particular, the optical and trigger system simulations, as relevant for this thesis, are presented in the first section, and the studies performed by me and making use of these two systems are the subject of the second section of this chapter.

9.1 ICARUS detector implementation in LArSoft

The implementation of the experiment specific code, including the geometry and the detector readout simulation, has to be maintained by the experiment that uses LArSoft and must be stored in experiment specific repositories. In ICARUS, this repository is called *icaruscode*. The analysis is facilitated using abstract analyser modules that convert the native artROOT formatted files into ROOT [170] histograms, graphs, and trees.

Figure 9.1 illustrates the ICARUS simulation workflow chart, which is common for all the SBN detectors. Following the chart, the simulation blocks within the red

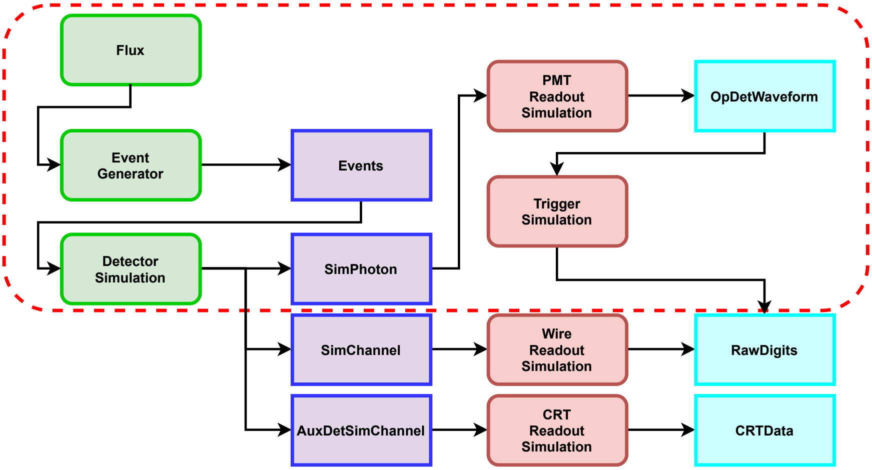

Figure 9.1: Simulation chain in LArSoft for SBN with simulation data products of the three detector subsystems: TPC, PMT, and CRT. The red dotted line demarks the part that has been used for the analyses presented in this PhD thesis.

dotted line, which are relevant for this thesis, will be briefly described.

9.1.1 Fluxes

The first step in simulating the experiment is the generation of particle interactions. In ICARUS, two main categories of events are considered: beam-related neutrino interactions and the ones from cosmic background. Thus, the simulation starts with inputting the predicted neutrino beam flux (BNB or NuMI) and the primary cosmic-ray flux to the applied physics generators.

Neutrino fluxes

The neutrino flux is modelled by a data-driven Monte Carlo (MC), tuned to the measurements of the primary proton beam and magnetic horn currents, the alignment of the neutrino beam, and the external hadron-production measurements.

As described in Chapter 4, the BNB neutrinos are produced in the decays of secondary mesons resulting from proton-Beryllium collisions. The BNB has already successfully operated for many years in both neutrino and anti-neutrino modes. The fluxes are well-understood thanks to the detailed simulation developed by the MiniBooNE collaboration [109]. The MiniBooNE beam simulation is based on the GEANT4 [114] software that generates hadronic interactions in the target and sur-

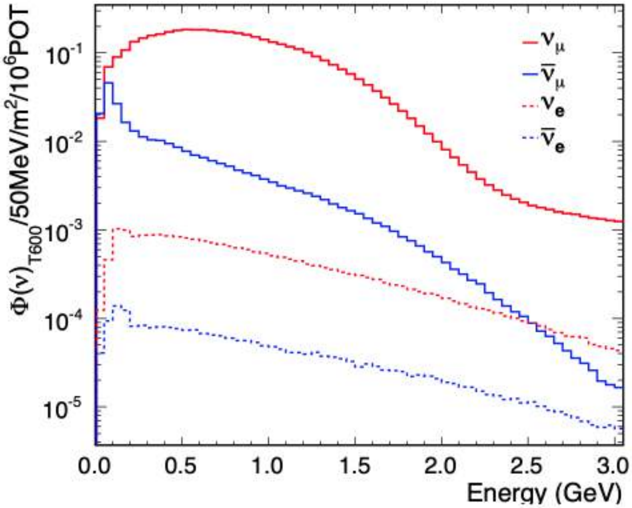

Figure 9.2: The BNB flux simulation at the ICARUS detector. Figure from [110].

rounding area, where the proton beam first interacts and produces the majority of secondary particles. The simulated model is reweighted according to external data measurements, of which the most significant come from the HARP [171] and BNL E910 [172] (pion production cross sections) and from SciBooNE [173] (kaon production cross sections) and global fits [174]. The particles produced in this simulation are tracked using GEANT4. Secondary hadronic interactions are simulated with the interaction cross sections tuned to experimental data. The secondary particles are tracked until they either decay producing neutrinos or are stopped, in particular at the beam dump. The neutrino tracks are extrapolated to the ICARUS detector to produce the predicted neutrino fluxes and energy spectra, as shown in Figure 9.2. A detailed description of the BNB beam composition can be found in Chapter 4.

The NuMI neutrino beam reaches the ICARUS detector at an off-axis angle of $\sim 6°$. The energy of neutrinos emitted at large angles to the parent meson in two-body pion or kaon decays depends only weakly on the parent meson momentum, resulting in the so-called kinematic focusing of the neutrino off-axis beam, which typically results in a significantly narrower neutrino energy spectrum than the on-axis case. The following calculation is used to demonstrate this feature.

Considering neutrinos produced in the two-body decay $\pi \to \mu + \nu_\mu$, as described in Ref. [175], from the energy and momentum conservation, an expression which relates the neutrino energy E_ν to the pion energy E_π, the pion mass m_π, and the muon mass m_μ is given by:

$$\mathrm{E}_\nu = \frac{\mathrm{m}_\pi^2 - \mathrm{m}_\mu^2}{2(\mathrm{E}_\pi - \mathrm{p}_\pi \mathrm{cos}\theta)}, \tag{9.1}$$

where θ is the angle relative to the pion direction at which the neutrino is emitted. After differentiating this formula with respect to E_π at constant θ, one can see that E_ν has a maximum when $\mathrm{E}_\pi = \mathrm{E}_\pi^{\mathrm{max}} = \mathrm{p}_\pi/\mathrm{cos}\theta$. By replacing E_π with $\mathrm{E}_\pi^{\mathrm{max}}$ in the expression above, the maximum neutrino energy $\mathrm{E}_\nu^{\mathrm{max}}$ for a given angle θ can be determined:

$$\mathrm{E}_\nu^{\mathrm{max}}|_\theta = \frac{\mathrm{m}_\pi^2 - \mathrm{m}_\mu^2}{2\mathrm{E}_\pi^{\mathrm{max}} \mathrm{sin}^2\theta}. \tag{9.2}$$

Both for pion energies greater or smaller than $\mathrm{E}_\pi^{\mathrm{max}}$, the neutrino energy is smaller than $\mathrm{E}_\nu^{\mathrm{max}}$.

Since around its extremum a regular function changes slowly, pions over a wide range of energies will decay to produce neutrinos with similar lab energies. This property is stronger for larger angles θ and effectively generates a neutrino beam with a narrowing spread of energies by positioning detectors at increasing off-axis angles. The dependence of E_ν on E_π for various angles θ is illustrated in Figure 9.3. Decreasing values of $\mathrm{E}_\nu^{\mathrm{max}}$ and narrowing of the neutrino energy spread with increasing angle θ are evident.

Figure 9.4 shows the resulting flux of the NuMI beam at the ICARUS detector for both the ν_μ beam and the ν_e contamination. The narrow distribution around the maximum energy of about 0.2 GeV is clearly visible.

Cosmic-ray flux

For a surface detector like ICARUS, an accurate prediction of the cosmic ray background is also crucial. Cosmic air showers are produced when galactic protons – or heavier elements like He up to Fe – interact with the Earth's atmosphere. This interaction leads to extensive air showers containing many particles in the interaction final states.

In the ICARUS simulation two models of cosmic-ray flux can be applied:

- *Proton-only*

  In this model, only cosmic protons are assumed to contribute to the Earth's cosmic-ray flux. The simulated primary flux is as follows:

  $$\Theta(\mathrm{E}) = 1.8 \times 10^4 (\mathrm{E}\ [\mathrm{GeV}])^{-2.71} \frac{\mathrm{nucleons}}{\mathrm{m}^2 \cdot \mathrm{s} \cdot \mathrm{sr} \cdot \mathrm{GeV}}, \tag{9.3}$$

  where E is the energy of the cosmic proton.

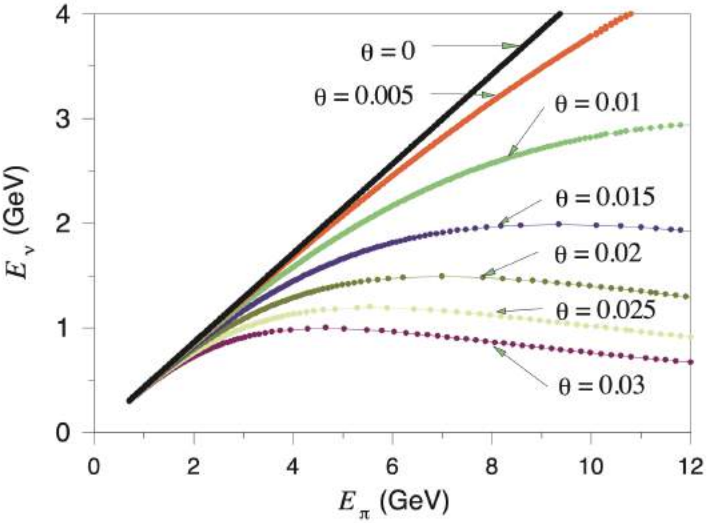

Figure 9.3: Neutrino energy, E_ν, as a function of pion energy, E_π, for neutrinos produced in two-body decays $\pi \rightarrow \mu\nu_\mu$. The distributions are shown for a number of off-axis angles θ (in radians) between the neutrino and pion directions. Figure from [176].

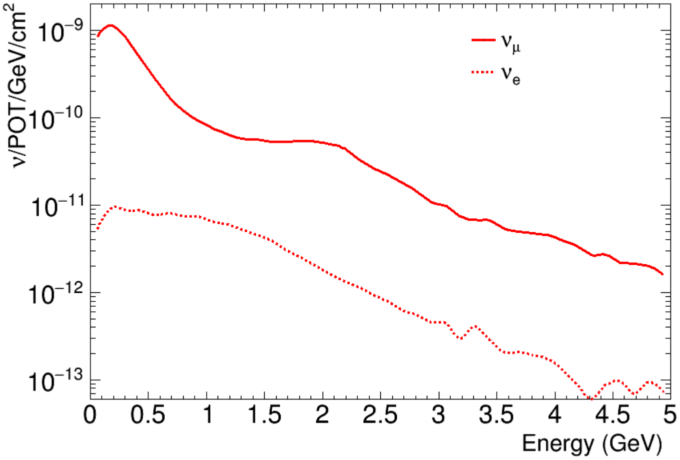

Figure 9.4: The NuMI beam flux prediction at ICARUS for forward horn current (FHC) mode. Image taken from the internal SBN technical note that is under preparation.

- *Constant Mass Composition (CMC)*
  In this model [177], the primary cosmic incident flux contains both light and heavy elements. The CMC model parametrises the spectra of individual components (e.g., protons, He, N, Mg and Fe), which are combined to reproduce the full primary particle spectrum. In this model, the flux of each primary element type is specified using:

$$\Theta_{\mathrm{A}}(\mathrm{E}) = \mathrm{K}_{\mathrm{A}}(\mathrm{E}/1\mathrm{GeV})^{-\gamma_{\mathrm{A}}}, \tag{9.4}$$

  where E, the energy of primary nucleus (per nucleon), is expressed in GeV and the index A denotes the type of incident nucleus. The spectral index γ_{A} is independent of nucleus type and is set to 2.71. K_{A} is the flux constant for primary nucleus A. It is a normalisation factor that is particle type dependent and takes the values of 1.72×10^4, 9.2×10^3, 6.2×10^3, 9.2×10^3 and 6.2×10^3 for p, He, N, Mg and Fe, respectively. The unit of K_{A} is such that the flux nucleons $\Theta(\mathrm{E})$ has the unit $[\mathrm{m}^2 \cdot \mathrm{s} \cdot \mathrm{sr} \cdot \mathrm{GeV}]^{-1}$.

Based on the above models, the primary cosmic incident flux is an input to the cosmic ray event generator.

9.1.2 Event generators

ICARUS simulation relies on open-source software packages interfaced with LArSoft to handle complex particle interactions that induce activity in the detector.

GENIE

GENIE [112] stands for Generates Events for Neutrino Interaction Experiments, and it is a ROOT-based [170] neutrino MC generator. The simulations of the neutrino fluxes result in neutrino energy, direction and spatial position distributions at some distance up to the upstream end of the ICARUS TPCs. This information is subsequently used as input to the GENIE neutrino event generator. Once GENIE is configured with a source of neutrinos, it propagates them through a geometry representing the detector to determine where and on which material neutrino interactions occur. The geometry usually includes also the detector's environment (detector hall, buildings, floor) to simulate the out of active volume interactions. GENIE sets neutrino interaction vertices in the selected volume to generate interactions proportionally to the interaction probability for different materials within that volume and covering the volume according to the beam flux. The output of the GENIE neutrino-nucleus scattering simulation is a set of final state particles that exit the nucleus. For each particle, 4-momentum, position and direction are provided.

CORSIKA

LArSoft supports two different cosmic-ray generators, CRY [178] and CORSIKA [179]. The latter, COsmic Ray SImulations for KAscade (CORSIKA), is the ICARUS default generator, and it has been used in the analysis described in Section 9.2. CORSIKA generates extensive air showers, i.e., the cascades of particles resulting from a primary cosmic-ray interactions, according to the primary cosmic flux at the top of the Earth atmosphere. The individual shower particles are tracked through the atmosphere until they undergo interactions or decays into secondary particles and then the particles from the interactions or decays are tracked. To save time, a pre-generated list of cosmic showers is available in the form of shower input files, which are randomly selected and distributed at the *ShowerArea* position/time as illustrated in Figure 9.5 for the ICARUS simulation. The position is a shower particle arrival point at the surface with preserved spatial correlations of particles within the shower. The time is the shower particle arrival time with some random offset per shower, including temporal correlations between particles within the shower. If the particles intersect the *BufferBox*, they are kept and extrapolated back to *ProjectToHeight* surface from where they are propagated down through the environment and the detector geometry using GEANT4. In the end, each event has a list of truth-level variables corresponding to each particle trajectory, energy and its full ancestry.

9.1.3 Detector simulation

The next step of the simulation is to collect the final state particles from event generators and propagate them through the detector and surrounding materials using LArSoft implementation of the GEANT4 framework, known as LArG4. This supports user-defined geometry, particle tracking, and a comprehensive library of physics models covering electromagnetic, hadronic, and optical processes.

The ICARUS geometric description has been developed based on measurements, engineering drawings and CAD models. It has been implemented in the Geometry Description Markup Language (GDML) and it includes:

- surface building, concrete pit, dirt surrounding the pit, concrete overburden;
- steel outer cryostat;
- foam insulation between outer and inner cryostats;
- aluminium inner cryostats;
- inner stainless steel structure for TPC;
- every TPC wire;
- 360 PMTs approximated by hemisphers;
- CRT modules approximated by hollow aluminium boxes.

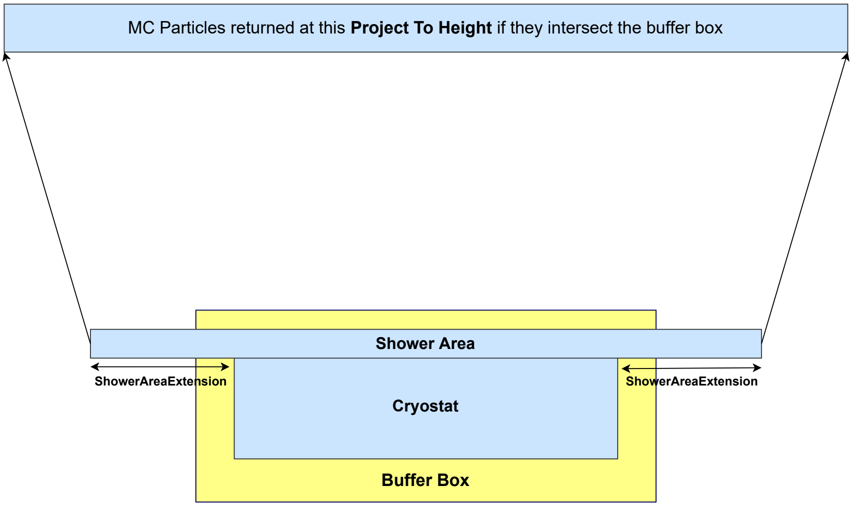

Figure 9.5: Explanatory drawing of the CORSIKA generation. *Buffer Box*: extension to the volume of each cryostat for the purpose of filtering out the particles which do not cross the detector. The surface the particles are detected through is defined by the *Shower Area* that includes both cryostats, and is located at the height of the ceiling of the cryostats. This surface can be increased by specifying a positive value for *Shower Area Extension* configuration parameter, in which case each side of the rectangle will be extended by that amount. *Project To Height*: the generated particles will appear to come from this height.

The GEANT4 simulates the paths of particles through a given medium based on the mean free path and interaction probability of the particle in that medium. This proceeds in discrete steps within the defined detector volume, resulting in simulated energy depositions at each step in the form of ionisation electrons and scintillation photons. At each step, if there is an energy deposition dE/dx$\neq$0, the charge gets drifted to anode wires, and the scintillation photons are propagated to the PMTs. In the next subsections, I will focus on the optical, PMT readout and trigger simulations, which are relevant for this thesis.

9.1.4 Optical simulation

As described in Section 3.2, in LAr minimum ionising particles generate about 40,000 photons/cm with the precise value depending on the particle species, the dE/dx, and the magnitude of the electric field, which make the optical simulation computationally challenging. For example, protons in the minimum ionisation generate 19,200 photons/MeV, while charged muons, pions and kaons produce 24,000 photons/MeV of deposited energy in a 500 V/cm drift field. Therefore, tracking each generated optical photon is not practical for regular simulation tasks. There are several strategies to address this issue. The one adopted in ICARUS is to use a *lookup table*, sometimes called a *photon library* that contains precomputed efficiencies of detecting a scintillation photon from anywhere in the active part of the detector by any of the ICARUS PMTs. Thanks to this approach, the complete optical simulation is not performed except when generating a new photon library.

To generate the photon library, the entire LAr volume of ICARUS is divided into cubic volumes called *voxels*. Given that the voxels have a side of 5 cm, about two million of them in total fit in a single ICARUS cryostat. In each voxel, 10^6 photons are generated isotropically with energies matching the LAr scintillation spectrum. The complete simulation, employing GEANT4, tracks every photon until its absorption. Each photon undergoes the simulation of the Rayleigh scattering in Argon and reflections on the surfaces within the detector, eventually being absorbed either at the active surface of an optical detector or at any other inactive surface. If the photon hits the sensitive surface of an optical detector, it is counted in as *detected* by this optical detector. If a photon, however, hits a passive surface that absorbs it, it is lost. At the end of the simulation, for a given voxel a value of a visibility is assigned to each optical detector. The visibility is equal to a number of detected photons by the optical detector divided by the total number of photons generated in a given voxel.

For a photon originating from a given voxel with a given initial momentum reaching the PMT a visibility value is saved in a table, as illustrated in Figure 9.6. This procedure is performed for each voxel covering a LAr volume of a single ICARUS cryostat. The conversion efficiency that reduces the bulk of detected photons is also applied. In the case of ICARUS, this is the PMT quantum efficiency which was measured to be equal to $\epsilon = (12.1 \pm 1.0)\%$ [180].

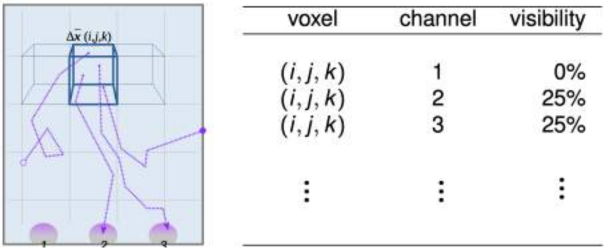

voxel	channel	visibility
(i, j, k)	1	0%
(i, j, k)	2	25%
(i, j, k)	3	25%
⋮	⋮	⋮

Figure 9.6: The visualisation of the lookup table used for the optical simulation in ICARUS. The figure represents one voxel and optical simulated photons propagation from it to the PMTs (*left*) and how the lookup table is filled (*right*). Each row of the table refers to a specific voxel location and a specific PMT channel. Image credit: Gianluca Petrillo.

The current photon library covers a single ICARUS cryostat. Both cryostats are considered identical, and dedicated software is used to cover the other cryostat with the same mapping.

With the application of the photon library, the optical simulation of an event typically takes minutes. Otherwise it would take hours.

The photon propagation time is parameterised with the group velocity of 13.5 cm/ns as measured at CERN [10]. The photon sample generated for filling the photon library is also used to generate the photon time-of-arrival distributions to optical detectors for each voxel. The distributions are fit with a combined Landau-exponential function, as presented in Figure 9.7. The parameters are then stored in the library.

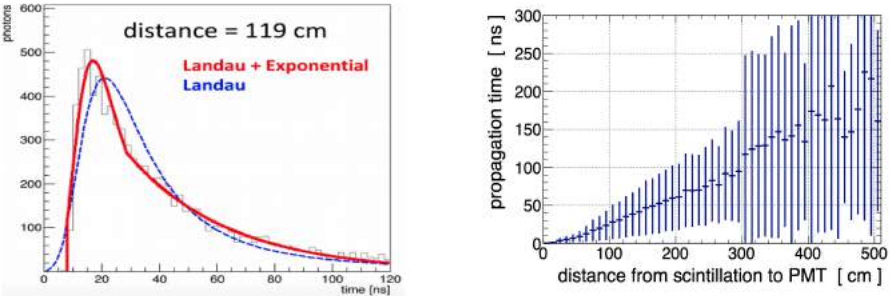

Figure 9.7: A photon arrival time parameterisation fit (*left*) and an average propagation time (Δt_p) as a function of a distance to the PMT, with error bars represented by RMS (*right*). Image credit: Diego Garcia Gamez.

In the ICARUS geometry description, the PMTs are defined as spheres with 20.32 cm (8 inches) diameter representing the photocathodes and 8.45 cm long cylinder base with 8.45 cm diameter representing the electron multiplier.

The visible fraction of photons, given by the photon library, at each PMT of a single TPC is shown in Figure 9.8 for two different slices along the drift coordinate. As could be seen, photon visibility depends on a distance to the PMT, being large in the PMT vicinity and becoming uniform at larger distances.

A clear boundary can be observed between the active and inactive volumes, i.e., inside and outside the field cage.

9.1.5 PMT readout simulation

The initial modelling of the PMT signal formation and digitisation was built on experience from the CERN test facility [8], described in Chapter 8. The single photoelectron response (SPR) signal of Hamamatsu R5912-MOD PMT (with a fixed delay matching a 37-metre coaxial cable) is used to model the PMT response with the parameters listed in Table 9.1.

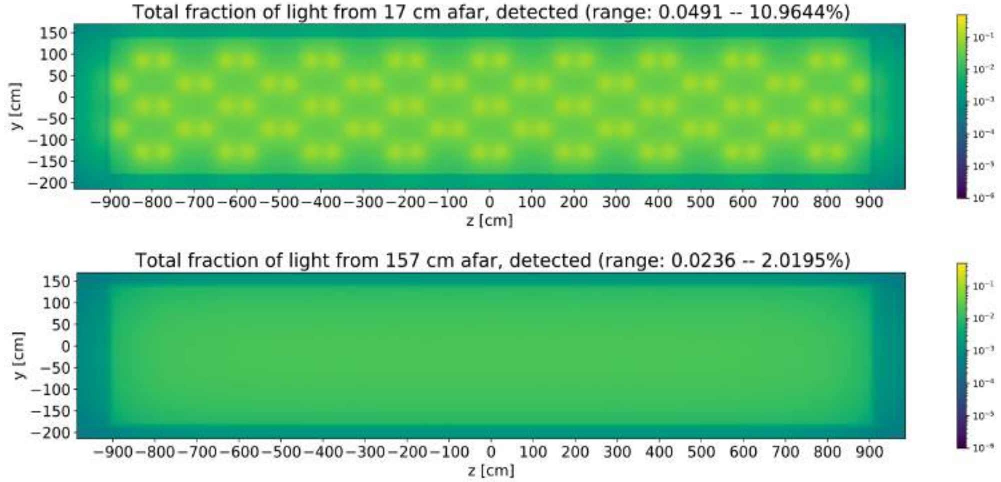

Figure 9.8: The total visibility at 17 cm from the front of the PMT plane (top). The spots of maximum visibility match the locations of the PMTs. Close to the cathode (bottom), the maximum visibility is only 2%. The shadowing by the field cage in a for of external rectangle is also visible. Figure from [181].

Parameter	Value
Transit time	55.1 ns
Rise time	1.8 ns
Fall time	4.2 ns
Amplitude	57 ADC
Gain	7×10^6

Table 9.1: Parameters of the PMT simulated response to the single photoelectron.

The PMT readout simulation starts with the signal digitisation process. After the propagation of all photons to each PMT and correcting for quantum efficiency, the converted photons are binned by their arrival time. Currently, the bin width is 2 ns. Bins are fluctuated following the Poisson statistics with 20% RMS to account for PMT gain fluctuations based on the first multiplication stage. Digitised waveforms with time discretisation of 2 ns are constructed using the fixed baseline (14999.5 ADC) and single photoelectron response for each PMT, converting from charge to ADC counts. The PMT waveform simulation assumes perfect linearity. The PMT dark current of 1 - 10 Hz can be added to the final waveform formed of the response to all detected photons. However, this option is usually disabled.

The zero-suppressed waveforms with variable length are acquired during the *enable* gate (±1 ms around the *beam spill* gate), except that 30 μs long waveform is always simulated during the *beam spill* gate. The waveforms are guaranteed to be non-overlapping, non-contiguous and sorted with increasing timestamp. Each discriminated waveform may merge information from multiple readout waveforms (raw::OpDetWaveform), but all from the same PMT. This step is performed for all 360 ICARUS PMTs. An example of a simulated PMT waveform is shown in Figure 9.9.

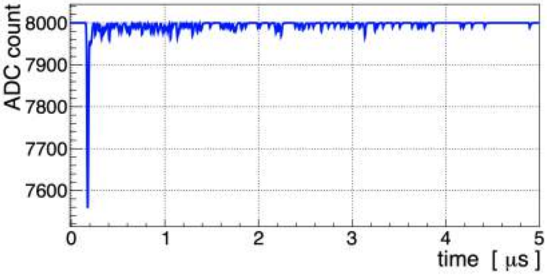

Figure 9.9: Simulated PMT waveform.

9.1.6 Trigger simulation

The ICARUS trigger simulation reproduces the system logic according to its description in Chapter 7. It is based on the simulated optical waveforms.

First, it produces single PMT discriminated waveforms according to a selected discrimination threshold. The result is one binary discriminated waveform with a value 0 when the waveform is under the threshold and 1 when it is above the threshold, with the same time discretisation as the PMT waveform.

Next, the discriminated waveforms are combined in pairs in the same fashion as the V1730B readout board produces LVDS output (see Chapter 7). The two available combinations of trigger gates are by sum (OR) or by multiplication (AND). The output of this step is roughly half as many discriminated outputs as there were from the previous step (some channels are not paired). Every time a pair surpasses the discrimination threshold, the pair is considered "open" for 200 ns, which corresponds to the LVDS signal duration. Provided that there is the PMT majority, defined by the number of LVDS signals occurring in coincidence within 150 ns window inside the 2 ms long *enable* gate as defined in Chapter 7, the PMT-TRIGGER is generated.

The next step requires coincidence with the *beam spill* gate to simulate the trigger logic based on the PMT-TRIGGER. If the PMT-TRIGGER is present in coincidence with the *beam spill* gate, the event is triggered. Parameters such as the pairing logic, the discrimination threshold, the LVDS signal duration and the number of LVDS signals required to form the PMT-TRIGGER (majority) are adjustable by the user.

Currently, the PMT in-spill acquisition for simulated data requires the Majority trigger (defined in Chapter 7), with a majority of 5 with all 360 PMTs being read out. The PMT out-of-spill acquisition requires the Majority trigger, with a majority of 10 and 180 PMTs of the cryostat, where the logic was satisfied, being read out. The discrimination threshold and the PMT pairing scheme are adjustable by the user.

9.2 Tests using LArSoft

In this section two examples of the application of the ICARUS simulation software are given. The first concerns the effect, on the reduction of cosmic-ray background, of placing a thick concrete block above the ICARUS detector. The second gives some insight into the simulation studies of trigger efficiency.

9.2.1 Overburden study

In order to reduce the cosmic background, an overburden placed on top of the ICARUS detector and almost 4π coverage of CRTs have been proposed [110]. The overburden is a 2.845 m thick concrete block to be placed above the Top CRT layer.

I performed the initial simulation study of this overburden and its impact on the cosmic background reduction. Generation of cosmic-ray fluxes was performed using the CORSIKAGen module, which sampled from a pre-generated set of primary cosmic proton showers, predicting a reduced flux of particles through the detector. Cosmic primaries were sampled from a data library generated by CORSIKA uniformly distributed on top of the cryostats, on a surface *ShowerAreaExtension*, extended by 12 m on each side. Only the particles whose trajectory crossed the *BufferBox* encapsulating the cryostats were considered in the simulation. Each particle with kinetic energy $E_K \geq 50$ MeV was then extrapolated back to ProjectToHeight surface placed 20 m above the centre of the TPCs and fed as input to the MC simulation. These particles and their daughters with energy down to 1 MeV threshold were then propagated through the detector using GEANT4. The two samples with and without overburden were simulated. In the case of the former, the 3,880 cosmic events, while in the case of the latter 3,960 cosmic events were produced.

The impact of the overburden on the spectrum of primary cosmic particles that enter the ICARUS TPCs is shown in Figure 9.10.

The overburden reduces the dominant muon flux by $\sim$30%, stopping the muons with $E_K \leq 1.5$ GeV. The small tail at lower energy is due to particles impinging the overburden-building floor interface and crossing only a fraction of the overburden or building floor. The suppression is very effective for the hadrons, reducing by a factor of $\sim$200 the flux of primary neutrons. The electromagnetic cosmic ray component (photons and $e^{\pm}$) gets eliminated.

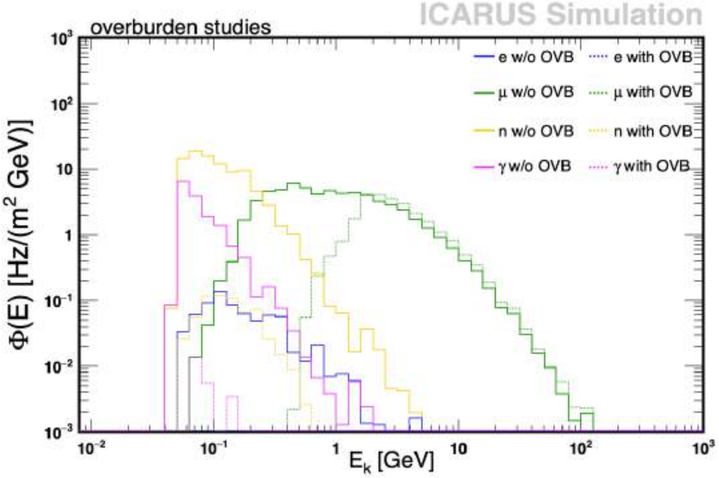

Figure 9.10: The simulated primary cosmic particle fluxes crossing the ICARUS active volume. The solid lines represent the primaries crossing the detector active volume using a complete geometry description of surrounding materials without the overburden (w/o OVB), while the dashed lines illustrate the flux of primary cosmic particles intersecting the detector active volume with the overburden included (with OVB). The plot does not show the smaller contributions from kaons and pions.

9.2.2 Simulated trigger efficiency

In order to test the ICARUS trigger design in terms of its efficiency in detecting neutrino interactions from the BNB and NuMI beams while minimising the amount of recorded data, the studies of the trigger response were carried out based on simulated PMT waveforms (raw::OpDetWaveform) used as an input to the simulated trigger.

By the time of performing this work, the joint work of the Trigger Working Group based on simulation had delivered the initial value of the PMT discrimination threshold of 200 ADC that reduces trigger rates of cosmic rays and strongly suppresses background due to ^{39}Ar decays and random noise (both not included in this study). Further optimisation of all trigger parameters is needed to minimise the background trigger rates and maximise the trigger efficiency of neutrino interactions.

In order to study different trigger conditions, i.e., BNB and NuMI trigger, the two neutrino Monte Carlo samples were generated using GENIE and BNB, and NuMI simulated fluxes, respectively. Moreover, to study the trigger impact on the cosmic background reduction, a CORSIKA generator was used to produce cosmic-ray events.

The generated samples were input to the detector simulation (with geometry including the concrete overburden) followed by the optical and trigger simulation steps described in the previous section. In the latter step, the MinBias trigger was applied (see Chapter 7) with the beam gate set to 1.6 μs for BNB and 9.5 μs for NuMI beam. The trigger condition was satisfied if either or both modules had the PMT majority above the discrimination threshold. The study included different trigger settings. Two combinations of PMT pairing schemes (OR or AND) and PMT majority requirements in the range of 1 - 10 were considered. The samples contained 1,776 BNB and 1,486 NuMI neutrino events, while the cosmic-like samples included 4,500 events.

As presented in Figure 9.11, the efficiency for BNB-like charged current interactions is close to 99% with the PMT majority requirement set to 1 for both PMT pairing combinations. The calculated trigger efficiency for νCC is compared to the corresponding ones for cosmic-ray events. Cosmic background events, depositing large amount of energy in the detector, trigger the system very easily, as long as they fall in the time window of the beam spill gate. The AND pairing scheme reduces better trigger rates of cosmic background, however the OR combination permits higher neutrino efficiencies even at higher PMT majorities.

By comparing the same studies for the NuMI case (Figure 9.12), the cosmic backgrounds are more efficiently rejected by the BNB trigger with keeping the neutrino interaction efficiencies at the similar levels.

Figure 9.13 presents the simulated trigger efficiencies for different neutrino interaction types. The efficiency for charged current interactions (mostly ν_μ) is predicted to be close to 99% with the loosest settings, while the neutral current interactions are more challenging to be triggered due to a lack of charged lepton in the final state. These effects are more visible for the BNB case than for NuMI.

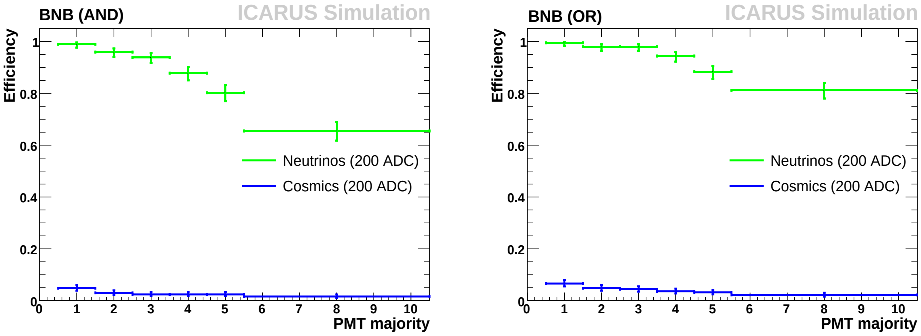

(a) AND.

(b) OR.

Figure 9.11: Trigger efficiencies for BNB beam simulated neutrinos (CC interactions), marked in green, and cosmic-ray events with applied BNB trigger conditions, marked in blue.

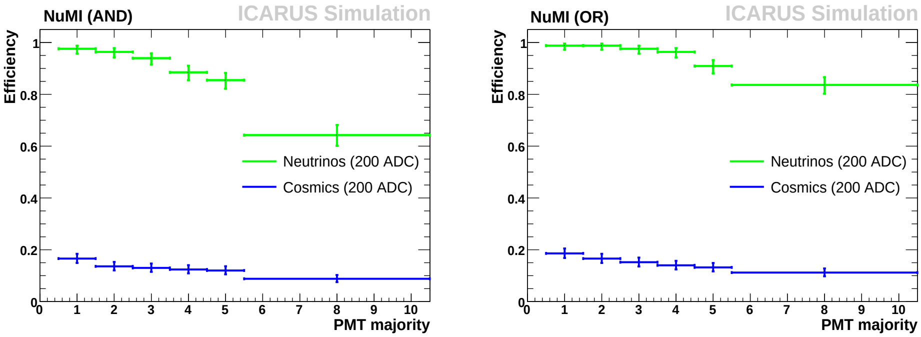

(a) AND. (b) OR.

Figure 9.12: Trigger efficiencies for NuMI beam simulated neutrinos (CC interactions), marked in green, and cosmic-ray events with applied NuMI trigger conditions, marked in blue.

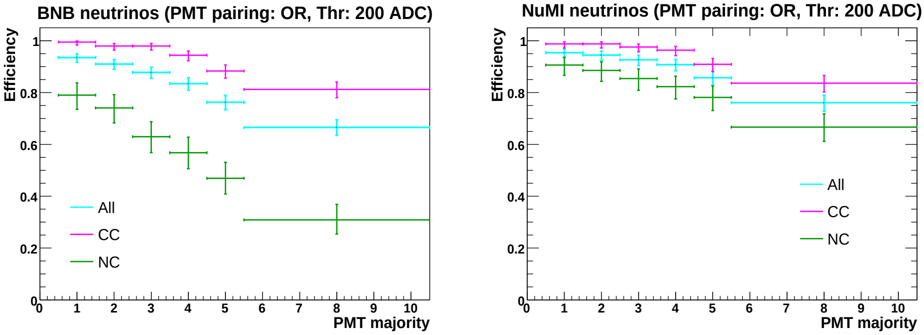

(a) BNB. (b) NuMI.

Figure 9.13: Trigger efficiencies for BNB and NuMI simulated neutrinos with respect to different neutrino interaction channels.

Chapter 10

Signal and background discrimination in the ICARUS detector using deep learning

The cosmic-ray background rejection in ICARUS starts at the online trigger based on the PMT information to reject most of the events outside and some events inside the neutrino beam spill window, as described in Chapter 7. However, the online trigger does not prevent the acceptance of most background events that enter the detector during the beam spill window. Rejection of such background is often possible using traditional cut-based selections, but this typically requires the prior use of computationally expensive reconstruction algorithms, applied to signals from both the anode wires and the PMTs. Once the CRTs are fully functional, analysis of their signals will also help to reduce the cosmic-muon background.

In this chapter, an alternative approach of using deep learning, a family of machine learning (ML) methods, is considered. 3D Convolutional Neural Networks (CNNs) trained on low-level timing information from the ICARUS PMTs and its modifications to reduce simulation dependence are described. This chapter also includes a brief introduction to the deep-learning concepts. Finally, first results of the networks application to the real data are presented.

The work described in this chapter was my initiative and has been already presented at the international conference [11]. The independent article with extended results is under final review by the internal ICARUS committee and will be submitted for publication.

10.1 Concept of the study

The focus of this study is to achieve a better rejection of cosmic rays than performed by the trigger whilst maintaining almost all neutrino interactions. This also results in reduction of data that must be processed by higher-level analyses. Although currently developed for offline analyses, this method could even be applied online as a higher level trigger.

As presented in Chapter 7, the PMT system provides the means to trigger signals within the beam spill windows. For each beam spill window, the ICARUS trigger system can assess which PMTs have signals exceeding a predefined threshold (called *openings*), at what time that signal was recorded with respect to the start of the beam window and how many times the PMT recorded an *opening* above the threshold.

For this study, the 3D position of each PMT pair, alongside its *opening* time and a number of *openings*, are converted into images and used to train a Convolutional Neural Network (CNN) [182, 183]. CNNs are especially effective when the detector data is represented as images, and its application for event classification is well established across the field of neutrino physics [184, 185, 186]. CNN algorithms learn how to classify images from a training sample (e.g., simulated neutrino and cosmic muon events) to be later used to make accurate predictions on new images (e.g., real data). A short introduction to the CNN algorithms will be given in next section.

An example of the images provided as input is shown in Figure 10.1. For this study, 396,200 PMT readout windows (events) containing cosmic rays and 120,000 containing a single BNB-like neutrino interaction were simulated.

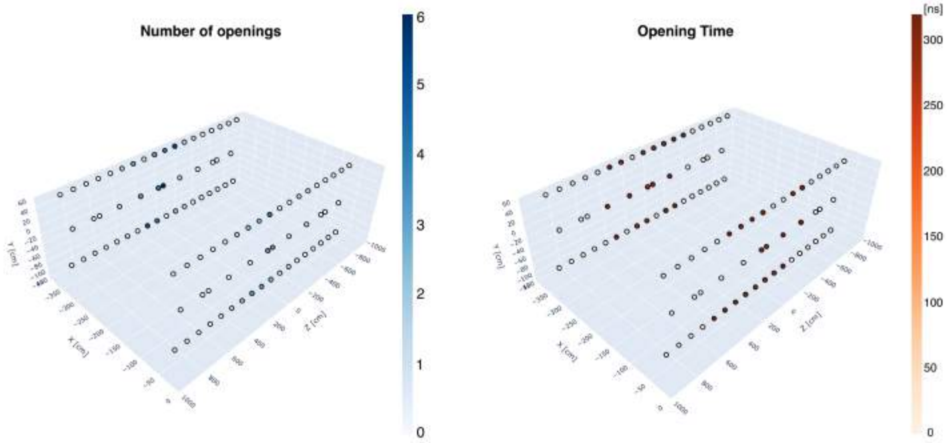

Figure 10.1: Example images of neutrino event input to CNN. Each dot represents a PMT pair distributed across the walls of one of the ICARUS TPC. The colour of the dots represents the number of *openings* (*left*) or the *opening* time (*right*), while the hollow dots represent PMTs with the signal below threshold. Figure from [11].

These events were processed by applying the simulated BNB MinBias trigger (see Chapter 7), PMTs paired in OR logic and a discrimination threshold set to 200 ADC (corresponding to ∼5 phe). This reduced the samples to 45,167 and 114,589 for cosmic events and BNB neutrino events, respectively. The samples were further divided into the CNN training, validation and test sets. The role of dividing the input data into training, validation and test sets is clarified in the next section.

The analysis was also performed for the NuMI case, with 598,900 simulated PMT readout windows (events) containing cosmic rays and 261,592 containing a single NuMI-like neutrino interaction. These events were processed by applying the simulated NuMI MinBias trigger, PMTs paired in OR logic and a discrimination threshold set to 200 ADC, reducing the samples to 259,060 and 258,400 for cosmic events and NuMI neutrino events, respectively.

The simulated events for both NuMI and BNB cases do not include the concrete overburden simulation to reflect the current state of the detector and hence make the comparison with the real data possible. The results of the analyses for both beams are presented in Section 10.3.

CNNs are a powerful tool for classifying events, but, like many analysis methods, they can suffer from a strong reliance on the details of the input simulation such that minor changes can result in significantly altered classification performance when applied to real data. To address this problem, the CNN classifier may rely on domain adaptation (DA) techniques [187, 188] so that the classifier learned from the training domain (i.e., simulated data) can also be applied to the testing domain (i.e., real data). This DA can be achieved through the application of Domain Adversarial Neural Networks (DANNs) [189], in which the real data is used in an unsupervised (or semi-supervised) manner to prevent the CNN exploiting features that differ between data and simulation. The concepts of unsupervised and supervised learning are explained in the next section, while the results obtained by applying a DANN and its comparison with the CNN results are presented in Section 10.4. DANNs were first used in neutrino physics by the MINERνA experiment, where the bias of a deep-learning-based neutrino vertex identification method was mitigated using these techniques [190].

10.2 Introduction to deep learning

In this section, the fundamentals of deep learning are introduced mainly based on Ref. [191] and Ref. [192].

Machine learning

Machine learning is based on taking some data, training a set of algorithms (regarded as a model) on that data, and using the trained model to make predictions on new data. Training a model can be regarded as a *learning* process. Typically, the data used is divided into three subsets, ideally, independent of each other, that are used in different stages of the creation of the model:

- **Training set**: the model learns from this set only. This set must be the largest.

- **Validation set**: it is used to evaluate the model (usually after every training epoch) and fine-tune the model hyper-parameters[1] (e.g., the learning rate or the model architecture itself).
- **Test set**: it is used to evaluate the model once it is fully trained.

During the learning process, new, unfamiliar data (from the training set) is gradually given to the model. At each step, the model makes predictions and receives feedback about how accurate its predictions were. This feedback is used to correct the errors made in the prediction. It may take many iterations to train a model with high predictive performance. Depending on the total number of training examples (m) and a number of training examples given to the model at the same time (n), it will take m/n iterations to go through the whole training set. This represents one epoch, which is used to separate training into distinct phases. At the end of each epoch, the trained model is validated using the validation set. The learning process continues until the predictions of the model no longer improve on the validation set.

Supervised learning

Supervised learning is based on algorithms that attempt to map each input with a specific output, following a set of examples $\boldsymbol{x}$ and outputs $\boldsymbol{y}$ (also known as targets or labels) to be trained on. In supervised learning, it is assumed that there is a relation between inputs and outputs, and the algorithm aims to learn this relationship. Supervised learning problems are divided into *classification* and *regression* problems. The classification problem example can be illustrated by tagging pictures of pets as cats or dogs while predicting house prices based on house features is a regression problem example.

Unsupervised learning

Unsupervised learning is based on algorithms that attempt to address problems with little or no knowledge of what the results should look like, based on a set of examples $\boldsymbol{x}$ to learn from. The main difference between supervised and unsupervised learning problems is that in the case of the latter, there are no labels $\boldsymbol{y}$ available for training. An example of unsupervised learning would be identifying meaningful patterns in 2D data.

Artificial neural network

---

[1] The difference between hyper-parameters and other parameters is that the former impact the learning process, while the latter are derived through the learning process.

Various types of models have been investigated for machine-learning systems. Deep learning, a family of ML algorithms, is based on artificial neural networks trying to imitate how the human brain works. An artificial neural network, as presented in Figure 10.2, is a combination of artificial neurons used to build multi-layer circuits that can perform several functions and learn non-linear features from the input data. The first and last layers in a network are called input and output layers, respectively, and all layers in between are called hidden layers. An artificial neural network learns multiple layers of non-linear[2] features and combines them in a final layer to produce a prediction.

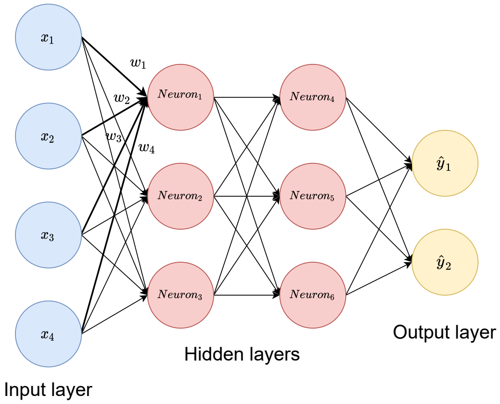

Figure 10.2: Example of artificial neural network that consists of an input layer based on four values, two hidden layers, also known as fully-connected layers, that contain three neurons each, and an output layer that is built of two neurons. All the neurons in one layer are connected with every neuron from the previous layer.

The artificial neuron can be thought of as a mathematical function that receives a vector of inputs $\boldsymbol{x}$ (which are outputs from other neurons or the actual input data) weighted by a weight vector $\boldsymbol{w}$ and a bias[3]. The artificial neuron sums them up to produce an output also known as *activation*. This output is then passed to the next layer or is the output result of the network as in the case of the sigmoid activation function explained in training section.

More precisely, the weighted sum of all inputs together with the bias inputs is

---

[2] The non-linearity of the classifier, defined by the network structure, is assumed to find the indicative feature combinations.

[3] The intercept term b is known as the bias parameter of the affine transformation. This term derives from the fact that the output of the transformation is oriented towards being b in the absence of any input data. Instead of adding the bias parameter b, one can continue using the model with weights but augment $\boldsymbol{x}$ with an extra entry set to 1. The weight corresponding to the extra entry plays the role of the bias parameter.

passed through a threshold-based non-linear function[4], known as an activation function, to obtain the neuron output.

Training

The neural network training will be explained using an example of logistic regression, i.e., a method of binary classification used to model the probability of input variables to be either *true* or *false*.

In this example, a simple neural network based on one neuron will be used. It accepts an input $\boldsymbol{x}$ that is passed to a linear equation $z(\boldsymbol{x}) = \boldsymbol{wx} + b$, followed by an activation function to output the prediction $\hat{y}$. $\boldsymbol{w}$ and b are the model parameters $\boldsymbol{\theta}$. The most common activation function for binary classification problems is the sigmoid function σ:

$$\sigma(z) = \frac{1}{1+e^{-z}}. \tag{10.1}$$

- If z is a large positive number, then $\sigma(z) \approx 1$.
- If z is a large negative number, then $\sigma(z) \approx 0$.
- If $z = 0$, then $\sigma(z) = 0.5$.

For each input example, the algorithm aims to make the prediction $\hat{y}$ as close as possible to the truth output y. For this reason, the network has to be trained by tuning the network parameters $\boldsymbol{\theta}$.

To start with, the values of the network parameters $\boldsymbol{\theta}$ (in this example, $\boldsymbol{w}$ and b) are set using one of the initialisation methods[5]. A neural network training can be divided into two steps: *forward propagation* and *backward propagation*.

Forward propagation

In forward propagation, for each input example $\boldsymbol{x}^{(i)}$, the corresponding prediction $\hat{y}$ is computed using:

$$\hat{y}(\boldsymbol{x};\boldsymbol{\theta}) = \sigma(\boldsymbol{wx}+b) = \frac{1}{1+e^{-(\boldsymbol{wx}+b)}}. \tag{10.2}$$

---

[4] The most common activation function for the hidden layers is the rectified-linear unit (*ReLU*). By definition ReLU$= max(0,x)$, thus if split from (-∞, 0] or [0, +∞) then the function is linear. However, it is easy to see that $f(-1) + f(+1) \neq f(0)$, hence by definition ReLU is not linear. A neural network where all the neurons from the hidden layers run a ReLU activation function is able to learn complex non-linear features from the input data [193].

[5] The initialisation step can be critical to the model's ultimate performance, e.g., initialising all the weights with zeros leads the neurons to learn the same features during training. Initialising with values too small or too large leads respectively to slow learning or divergence. Choosing proper values for initialisation is necessary for efficient training and thus requires proper methods. Common initialisation methods are *Xavier* and *He* [194].

Subsequently, the discrepancy between $\hat{y}$ and the true output y is estimated using a loss function (error function) L, which in binary classification problems is binary cross-entropy loss function:

$$L(y^{(i)}, \hat{y}^{(i)}) = -(y^{(i)} \log(\hat{y}^{(i)}) + (1 - y^{(i)}) \log(1 - \hat{y}^{(i)})). \tag{10.3}$$

- If $y^{(i)} = 0$, then $L(y^{(i)}, \hat{y}^{(i)}) = -\log(1 - \hat{y}^{(i)})$, where $\hat{y}^{(i)}$ should be close to 0 in order to minimise L.
- If $y^{(i)} = 1$, then $L(y^{(i)}, \hat{y}^{(i)}) = -\log(\hat{y}^{(i)})$, where $\hat{y}^{(i)}$ should be close to 1 in order to minimise L.

Next, the average loss function for the entire training set is calculated to obtain the cost function J:

$$J(\boldsymbol{\theta}) = J(\boldsymbol{w}, b) = \frac{1}{m}\sum_{i=1}^{m} L(y^{(i)}, \hat{y}^{(i)}) = -\frac{1}{m}\sum_{i=1}^{m}(y^{(i)} \log(\hat{y}^{(i)}) + (1 - y^{(i)}) \log(1 - \hat{y}^{(i)})), \tag{10.4}$$

where m is the number of training examples (input examples).

Backward propagation

After calculating the cost function J, the next step is to find the $\boldsymbol{\theta}$ parameters that minimise $J(\boldsymbol{\theta})$. A way of doing this is by computing the partial derivatives of J with respect to the parameters $\boldsymbol{\theta}$ ($\boldsymbol{w}$ and b in the logistic regression example). The partial derivatives will indicate how the J function will change with varying the values of $\boldsymbol{w}$ and b. The derivatives of J with respect to $\boldsymbol{\theta}$ are known as *gradients*. The computed gradients are used to update the value of $\boldsymbol{\theta}$ as follows:

$$\theta \to \theta - \alpha \frac{\partial J(\boldsymbol{\theta})}{\partial \theta}, \quad \forall \theta \in \boldsymbol{\theta} \tag{10.5}$$

where α is the learning rate, the most critical hyper-parameter in ML models.

The learning rate determines the step size used for updating the network parameters $\boldsymbol{\theta}$. The larger the step, the faster the algorithm approaches the global minimum, with the risk of “bouncing around” the minimum. Conversely, choosing the value too small may result in a long training process that may get stuck in the local minimum. The backward propagation computations are usually vectorised to handle several input examples at the same time.

Gradient descent

In neural networks, the algorithm that iteratively computes the predictions (forward propagation), computes the derivatives (backward propagation), and updates the weights is known as *gradient descent*. However, the traditional gradient descent is slow on huge training datasets. Thus, to improve the optimisation algorithm converge, a *stochastic gradient descent* (SGD) is used. In SGD, only a small randomly selected portion (called a mini-batch[6]) of the training dataset is used in each iteration. Neural networks tend to converge after computing several training epochs [195].

Under- and overfitting

Training neural networks, to be ready to make predictions on unseen data, is usually not an easy task. There are two undesired ways of how a model can fit the training data:

- Underfitting: where the model is too simple to reliably learn the behaviour of the training data.
- Overfitting (also known as overtraining): where the model is too complex to make proper predictions on unseen data.

Regularisation methods

Dealing with underfitting is typically solvable by increasing the training time, getting more training examples, adding more complexity to the model (i.e., adding more layers or more neurons per layer). However, overtraining could be a more severe issue since simplifying the network may reduce the model capacity. If the training set is small, adding more training examples could help. However, increasing the size of the dataset is not always possible. Then, *regularisation* is needed. Regularisation techniques introduce minor modifications to the network architecture, the training phase, and even to the input data to improve model performance (even on data unfamiliar to the model). Some common regularisation techniques are:

- L^1 and L^2, which are the most common regularisation methods that prevent overtraining by penalising the model weights [196]. They update the loss function by adding a so-called *regularisation term* that is different for L^1 and L^2. In L^1, the sum of absolute values of the network parameters $\boldsymbol{w}$ to the original loss function L is added:

$$L' = L + \lambda \sum_{i=1}^{N} |w_i|, \tag{10.6}$$

while L^2 adds the sum of the squared values of the weights $\boldsymbol{w}$ to the loss:

---

[6] Batch or mini-batch is a set of n input examples. The input examples in a batch are processed independently, in parallel. During training, a batch results in only one update to the model (one forward pass and one backward pass).

$$L' = L + \lambda \sum_{i=1}^{N} w_i^2, \tag{10.7}$$

where λ is the regularisation term, and it should be > 0. L^2 regularisation is also known as *weight decay*, as it imposes the weights to decay towards zero (but not exactly zero).

- Batch normalisation: is a regularisation method that standardises the inputs to a layer for each input batch of data, stabilising the learning process [197].
- Dropout: is a computationally inexpensive regularisation technique that randomly ignores some non-output units from certain layers, introducing noise to the learning process and forcing the model to become robust to deal with the noise [198].
- Early stopping: training complex networks for too long could cause the training error to decrease steadily over time but make the validation (and test) error rise at some point. Early stopping [199] deals with this problem by monitoring the validation results systematically and finishing the training as soon the validation error does not decrease any more.

10.3 CNN-based approach to event filtering

The main feature of CNNs is that they learn a series of filters[7] (using convolutions), applied in sequence to extract increasingly powerful and abstract features that allow the CNN to learn a relationship between input images and target labels. CNNs do not require manual feature engineering as they can understand relevant features during training. Due to the procedure of convolution, CNNs are much more computationally efficient than regular neural networks. In addition, they can be optimised to run on any device, which makes them possible to work online.

Signals collected by the ICARUS PMT system contain enough information about interactions in LAr and lend themselves nicely to image recognition techniques such as CNN that once trained, can be applied to new images, e.g., real data, to classify the physical events and thus filter the most interesting ones.

10.3.1 Network architecture

The designed CNN architecture used in this study is depicted in Figure 10.3. The network consists of several convolutional layers followed by pooling layers. Convolutional layers detect the presence of features in an input image, indicating their

---

[7] Filters, also known as kernels, consist of a set of values that the CNN learns through the training process.

locations and strength in the form of feature maps. Pooling layers are used to reduce the size of the feature maps. Thus, the number of learning parameters and the amount of computation performed in the network is minimised. Thanks to the pooling layer, further operations are performed on summarised features instead of precisely positioned features generated by the convolution layer. This makes the model more robust to variations in the position of the features in the input image, known as translation invariance, which is especially advantageous in neutrino experiments, where signals can arrive at any location in large uniform detector volumes. The pooling operation that calculates the largest value in each patch of each feature map is called *max pooling*. There is another type of pooling used, which is called *global pooling*. Instead of down-sampling the input feature map patches, global pooling down-samples the entire feature map to a single value. The final layers are fully connected, where the softmax[8] activation function follows the final output layer.

Due to the large detector size, the input images are typically very sparse as only a fraction of PMTs registers signals for each event. As a result, relatively few pixels of the input images hold non-zero values. Thus, much of the computation time is spent unnecessarily applying convolutions to many patches of pixels with zero values. For this reason, the submanifold sparse convolutions are used as suggested in Ref. [200].

The CNN was trained using Python 3.6.9 and PyTorch 2.1.0[9] [201] using the Minkowski Engine version 0.5.4 [202] on an NVIDIA Tesla V100 GPUs. Stochastic Gradient Descent was used as the optimiser, with a mini-batch size of 32 events, and a learning rate of 0.1 (divided by 10 when the error plateaus, as suggested in Ref. [203]).

10.3.2 CNN event filtering performance

Once trained, the output of the CNN is a score for each event between 0 (neutrino-like) and 1 (cosmic-like). The distribution of CNN scores for each true event type in the test sample is shown in Figure 10.4. If a selection of neutrino events is made by cutting at a CNN score of 0.5, a 99.3% selection efficiency is maintained whilst 74.2% of cosmic-ray background events are rejected. The charged-current selection efficiency was found to be flat (i.e., unbiased by kinematics) in various tested observables. An example of neutrino selection efficiency with respect to the outgoing lepton angle is shown in Figure 10.4.

These results show how the PMT information can be used to achieve sufficient signal (neutrino interactions) to background (cosmic-ray interactions) separation.

---

[8] The softmax function is a generalisation of the sigmoid function. It transforms input values into values that sum up to 1 so that they can be interpreted as probabilities.

[9] It is a deep-learning framework that offers simplified methods for designing and training deep neural networks on both CPU and GPU.

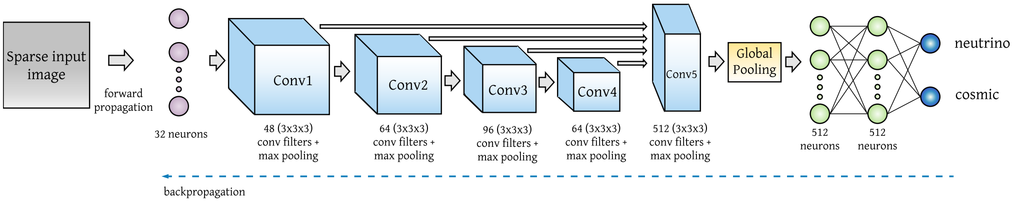

Figure 10.3: The CNN architecture used for this analysis. It consists of four convolutional blocks, where each of them applies a number of convolutional filters. The output of each convolutional block is the input to the next block so that each block learns more low-level features about the input images. Each convolutional block is followed by a max-pooling layer to reduce the size of the feature map. There is a fifth convolutional block that receives the concatenated output of the other four convolutional blocks as input and is also followed by a max-pooling layer; in that way, this last convolutional block learns from high- and low-level features at the same time. The output of the last block is passed to a global pooling layer which is also used to down-sample the feature map, but in this case, by reducing the dimensionality from 4D to 1D. The last fully-connected layers map the output of the global pooling layer into scores classifying the input event as neutrino or cosmic. Figure from [11].

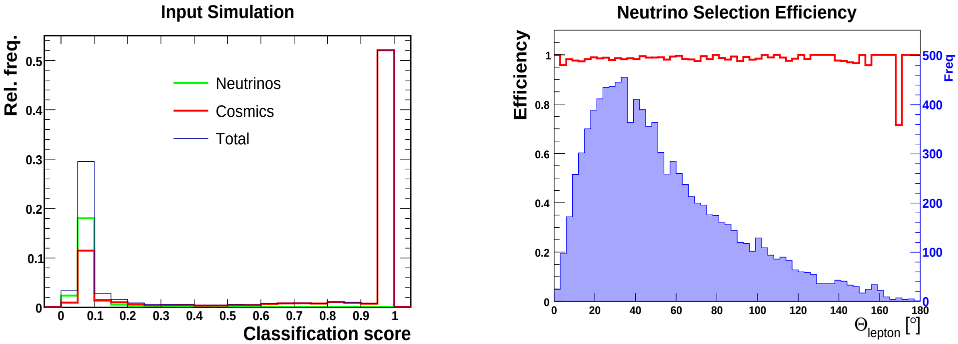

Figure 10.4: The trained CNN's classification of events in the test sample (*left*) for the BNB events. It is worth noticing that the relative normalisation of cosmic and neutrino events is fixed to approximate what would be expected in real data. The distribution of the outgoing lepton angle (blue) with respect to the incoming neutrino is shown alongside the neutrino selection efficiency of the CNN (red) following a cut at a score of 0.5 (*right*). Figure from [11].

10.4 Reducing model-dependence with DANN-based training

Whilst the CNN presented above shows excellent performance, the results assume perfect modelling of the neutrino and cosmic-ray events, the particle propagation and the detector response. If the CNN is trained with events that do not suitably represent what is in the real data, then the performance from the test sample will not be reliable. Machine learning methods can be especially susceptible to performances strongly dependent on simulation as it is unclear which features are used for classification. Ensuring that relevant aspects of physical events are well modelled is not easy. Thus, to alleviate this issue, adversarial training methods can be employed to prevent neural networks from learning features that appear in simulations but not in the real data. This analysis aims to show a possibility of mitigating simulation dependence through the application of DANNs.

In DANNs, the neural network model is trained on examples from two domains: (a) the *source* domain, consisting of labelled simulated data; and (b) the *target* domain, which includes unlabelled true experimental data. The goal is to learn a discriminator from the labelled source domain examples and use the unlabelled target domain examples to ensure the discriminator depends only on domain-invariant features to perform the predictions.

The updated network architecture is shown in Figure 10.5. It is based on a combination of a feature extractor (i.e., the bulk of the CNN described in Ref. 10.3.1) and a label predictor (i.e., the fully-connected layer(s) at the end) as one path, complemented by a second path that connects the output of the feature extractor through a gradient reversal layer with a few fully connected layers that form a domain classifier. The gradient reversal layer performs an identity transformation during the forward propagation process but multiplies the gradient by a negative constant during the backward propagation, assuring that the parameters learnt by the feature extractor are made similar for the source and target distributions. Therefore, the features learned by this model are both discriminative - thanks to the label predictor - and domain invariant - thanks to the domain classifier.

10.5 Results of the comparison of the CNN and DANN performances

In order to test the effectiveness of DANNs as a method of reducing simulation dependence, a series of *mock-data* studies were performed. For these studies, a statistically independent simulation of events (from neutrinos and cosmic rays) is produced before being modified to simulate possible mis-modelling bias. Since the coarse PMT information used in this analysis is likely not sensitive to the exact details of the neutrino interaction or cosmic-ray production, the main focus was made on applying

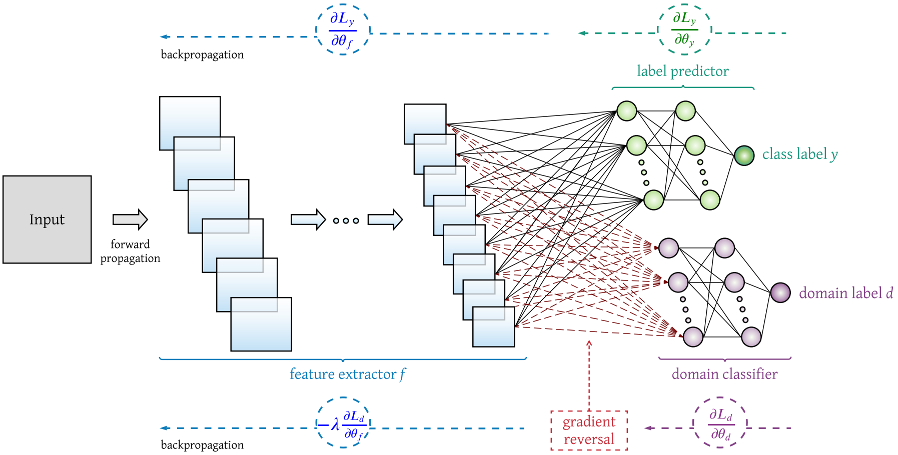

Figure 10.5: Domain-adversarial neural network architecture. The feature extractor (blue) and the label predictor (green) form a standard neural network classifier. The domain classifier (purple) provides the domain adaptation part since it is connected to the feature extractor through a gradient reversal layer, allowing the alignment of feature distributions across the source and target domains. In this study, the input are the images like the one in Figure 10.1, the class level is neutrino or cosmic-ray interactions, and the domain label is real data or simulated data. Figure from [11].

distortions to the simulated detector response. The details of the mock data are described below.

"Global noise" data: in this mock data, a noise that is uncorrelated with the event content is randomly added to each PMT with some pre-specified ('global') probability common to all PMTs. The global noise probabilities considered are 2%, 5% and 10%. The timing of the noise is considered as uniform distribution, and if noise is simulated to arrive before a PMT is opened by a simulated signal, the opening time of the signal is overwritten by that of the noise.

"Local noise" data: similarly to the global noise data, this mock data set considers the addition of random noise to each PMT but where the probability of producing noise is different for every PMT. Noise probabilities per event for each PMT were generated randomly using a uniform distribution between 0 and 2%, 5% or 10%.

For each mock data study, the DANN is trained as described in Section 10.3.1 but with an addition of 9,109 cosmic-ray mock-data events and 37,724 neutrino mock-data events, which are only labelled by the domain (i.e., as mock data or MC) and not by event type (i.e., cosmic or neutrino event). This method could equally be applied to real data.

Both the originally trained CNN and the newly trained DANN are used to classify events from the original training sample and the new mock data sample. An example of the classification scores for each model applied to the original and mock data set is shown for two mock data studies in Figure 10.6. A summary of the neutrino selection efficiency and the background rejection performance for each mock data set is shown in Table 10.1.

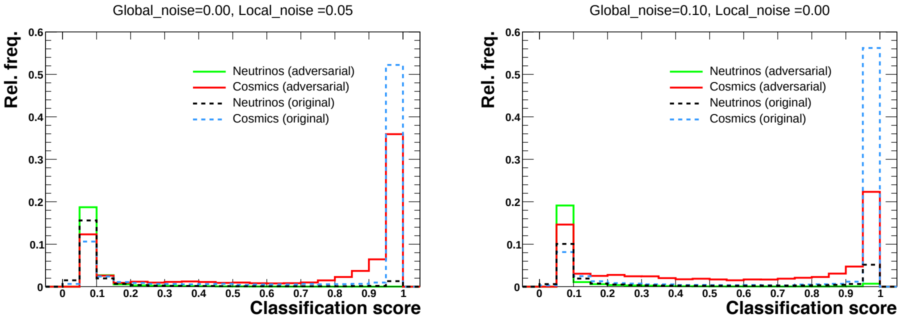

Figure 10.6: Results (BNB case) of the classification score of the nominal CNN and adversarially trained DANN model applied to the original and: local noise mock data using a 5% noise spread (*left*) and the global noise mock data using a 10% noise spread (*right*). Figure from [11].

From these results, it can easily be seen that, without the adversarial training, the original CNN can reject a sizable portion of neutrino interactions (the efficiency drops from 98.9% to 90.2% and 66.4% when adding the local noise mock data using 5% noise spread and the global noise mock data using a 10% noise spread, respectively). However, once the adversarial training is used, the network can mitigate the bias and maintain a very high neutrino selection efficiency (the main goal of the filter) whilst continuing to achieve a significant rejection of cosmic-ray backgrounds. The results of the adversarially trained network can recover the neutrino selection efficiency drop caused by introducing mock data by up to even 22%, depending on the kind of applying distortions to the simulated detector response.

10.6 Statistical uncertainties

An additional study was performed to evaluate the statistical uncertainties of the neutrino selection efficiency ($\mathcal{E}_\nu$) and cosmic background rejection ($\mathcal{R}_{cos}$) results.

In the case of the adversarial models (DANN), the total generated mock data was used, hence the statistical uncertainty in the model prediction could not be easily assessed without generating more events (which is computationally expensive).

Dataset		Model type	$\mathcal{E}_\nu$ [%]	$\mathcal{R}_{cos}$ [%]
Nominal		Original	98.9	76.3
Global noise	2%	Original	91.7	74.8
		DANNG2	92.7	76.5
	5%	Original	81.0	75.8
		DANNG5	89.7	72.1
	10%	Original	66.4	79.0
		DANNG10	88.8	71.0
Local noise	2%	Original	95.5	75.1
		DANNL2	97.6	74.2
	5%	Original	90.2	74.8
		DANNL5	89.9	75.0
	10%	Original	81.9	75.7
		DANNL10	90.2	73.3

Table 10.1: Neutrino selection efficiency ($\mathcal{E}_\nu$) and proportion of rejected cosmic-ray background events ($\mathcal{R}_{cos}$) using the original CNN (Original) and adversarially trained DANNs to classify events in the nominal simulation and mock data. The results were obtained testing networks on different datasets according to the first column.

However, for the original CNN, only a small portion (10%) of each mock data was needed to be tested on as in this case there was no adversarial training. Therefore, the network could be tested on the remaining 90% of each mock data to estimate the statistical uncertainty. The data was then divided into nine equally sized samples, resulting in 10 sets for evaluating the uncertainty of the CNN prediction for each mock dataset.

Over the ten statistically independent samples, it was found that the spread (calculated using the RMS of the samples) of the neutrino efficiency was at the level of 0.2 - 0.4% and for the background rejection between 0.7 - 0.9%. This is much smaller than the level of the difference in performance seen between the models. It seems reasonable to expect the statistical uncertainty on the DANN performance to be at a similar level (since the same number of events was used and it uses the same underlying neural network architecture for the feature-extractor and label-predictor parts). It should also be noted that the same mock data sample is used when testing the DANN and CNN, so entries in adjacent pairs of rows in the table are 100% statistically correlated.

Overall, this shows that the size of the statistical fluctuations is much smaller than the differences between model performance.

10.7 Application of the network to the real data

The ICARUS detector is still in the commissioning phase and has only recently begun providing data. However, the sample recorded with calibrated PMT system is already available and thus lend itself nicely to test the DANN on real data. The sample used was Run 6031 with 25,290 events for the NuMI off-axis beam. This sample was passed through the simulated trigger (adopted to work with real data) and divided into training, test and validation sets. Thanks to this, the DANN was trained on real data, instead of mock data like presented before. The results on the test samples for both real data and MC data are shown in Figure 10.7.

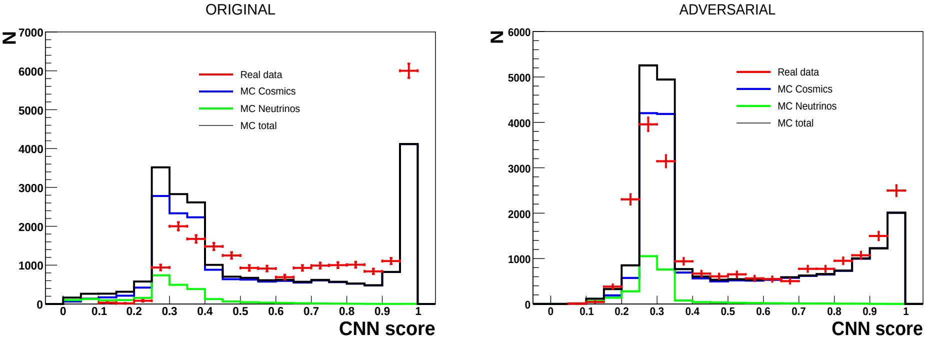

Figure 10.7: Results (NuMI case) of the classification score of the original CNN (*left*) and adversarially trained DANN model (*right*) applied to the simulated and real data.

The DANN trained on real data using Run 6031 was also tested on the real data from Run 5507 and real data from Run 5510 that were eye-scanned, using event display, by properly trained people to select neutrino candidates. Thanks to this effort in these runs it was possible to check how both networks perform with respect to human eye. The results are shown in Figure 10.8.

The average CNN score for the selected neutrino candidates is 0.31, while the achieved efficiency is 95%. Application of the DANN trained on the real data to the same list of events results in average score of 0.28 and the obtained efficiency is 99%. However, the rejection factor of the potential background decreases for DANN from 68.5% (CNN case) to 57.2%. These factors, however are strongly dependent on the selected cut as presented in Figure 10.9.

10.8 Summary of the results

The results demonstrate that using only low-level PMT information, effective filtering out of most cosmic-ray events can be achieved whilst almost no neutrino events are

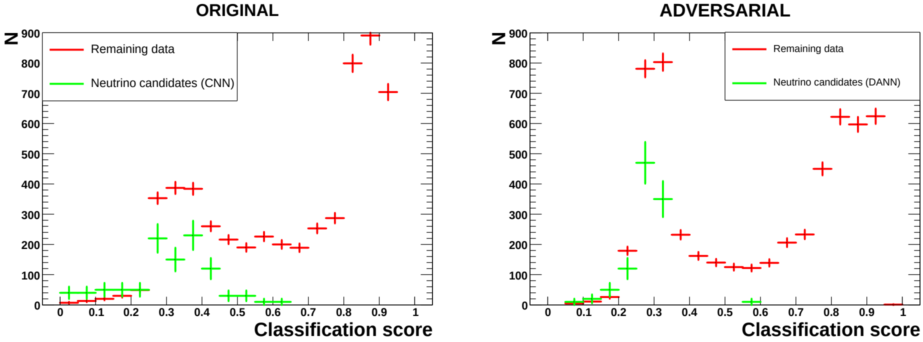

Figure 10.8: Results (NuMI case) of the classification score of the original CNN (*left*) and adversarially trained DANN model (*right*) applied to real data that were eye-scanned. The green crosses represent the events selected by the scanning group as neutrino candidates while the red crosses represent the remaining data. It is important to notice that the green distribution was scaled by factor of 10 for better visibility.

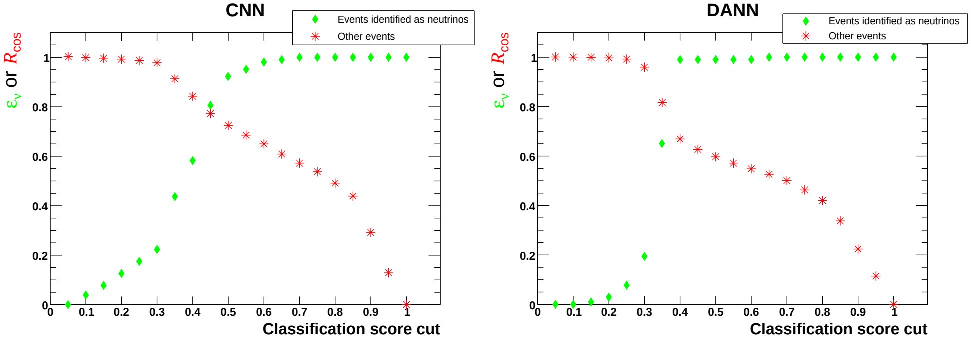

Figure 10.9: The illustration of how the filter performance can be influenced by selecting different cuts for the nominal CNN (*left*) and adversarially trained DANN model (*right*) applied to real data that were eye-scanned. For this kind of data, everything tagged by the scanning group as neutrino candidate is treated as a signal and everything else is treated as a background. Thus, this plot's efficiency and background rejection are not the same efficiency and background rejection presented when applying the network to simulations.

rejected. It is shown that mis-modelling in the input simulation can cause a trained CNN to reject neutrino events inadvertently. However, adversarial training via a DANN can mitigate the loss of efficiency at the cost of some reduced background rejection. Further studies using bigger samples of simulated events and the real data of both BNB and NuMI beams are being continued.

Conclusions and outlook

The Short Baseline Neutrino program at FNAL is well on its way to an exciting search for neutrino oscillations over a short baseline addressing the sterile neutrino puzzle, making high precision measurements of neutrino-Ar cross sections and developing LAr TPC technology in preparation for DUNE. The assembly and installation of the SBND detector are progressing, with projected activation foreseen for 2023. The MicroBooNE detector has already started producing high statistics measurements of neutrino-Ar interactions. It has also been releasing the first results on the low energy excess, based on 7×10^{20} POT, rejecting the hypothesis that ν_e CC interactions are fully responsible for the MiniBooNE excess at 97% CL in all analyses. Despite the challenges posed by the COVID-19 pandemic, the ICARUS detector was activated in August 2020 and took first neutrino data from BNB (2.8×10^{19} POT) and NuMI (5.2×10^{19} POT) in June 2021.

The ICARUS light detection system is fully functional with all the PMTs switched on (only 3 out of 360 PMTs are not working). The system requires regular calibration of the PMT gains with the laser system and fine-tuning based on counting rates. The ICARUS trigger system has been initially activated. Data collected by triggering on the BNB extraction signal in one cryostat were used to check the timing/reading of the TPCs and PMTs signals and the beam gate time, which was a prerequisite for implementing triggering. The next steps consider the trigger optimisation based on the light detection system to reduce the random triggers and ^{39}Ar-related signal. The further development considers the investigation of the bunched beam structure and the implementation of the information from the CRT system, followed by adding the concrete overburden helping to shield the detector mostly from the hadronic cosmic background. Commissioning of full Cosmic Ray Tagging system and installation of the concrete overburden are scheduled for an early 2022.

The further cosmic background rejection will be done by filtering the events based on the information available from the PMTs using machine learning. While the obtained neutrino selection efficiency and the cosmic background are very high, the Convolutional Neural Network trained only on the simulated data might be biased. Therefore, to deal with the simulation imperfections, this method was upgraded to Domain Adversarial Neural Network, which allows the filter to learn the domain invariant features. This method will be further developed, and the plan is to integrate it with LArSoft to be available for use by the ICARUS collaboration. Once ready, the filter can also be upgraded to filter neutrino flavours by adding more information from other detector subsystems (CRTs, TPC wires).

List of abbreviations

APA	Anode Plane Assembly
ArgoNeuT	Argon Neutrino Test
ART	Analysis Reconstruction Tool
ATLAS	A Toroidal LHC ApparatuS
BNB	Booster Neutrino Beam
BSM	Beyond the Standard Model
CC	Charged Current
CCQE	Charge Current Quasi Elastic (Scattering)
CERN	European Council for Nuclear Research
CKM	Cabibbo–Kobayashi–Maskawa
CL	Confidential Level
CMS	Compact Muon Solenoid
CNGS	CERN Neutrinos to Gran Sasso
CNN	Convolutional Neural Network
CORSIKA	COsmic Ray SImulations for KAscad
CPA	Cathode Plane Assembly
CP	Charge Parity (Symmetry)
CPU	Central Processing Unit
CRT	Cosmic Ray Tagger
DAQ	Data AcQuisition

DBB	Decoupling and Biasing Board
DIS	Deep Inelastic Scattering
DNN	Deep Neural Network
DONuT	Direct Observation of Nu Tau
DUNE	Deep Underground Neutrino Experiment
EM	Electromagnetic
ES	Elastic Scattering
FHC	Forward Horn Current
FNAL	Fermi National Accelerator Laboratory
FPGA	Field Programmable Gate Array
FSI	Final State Interactions
FWHM	Full Width at Half Maximum
GALLEX	GALLium EXperiment
GAr	Gas Argon
GDML	Geometry Description Markup Languag
GEANT4	GEometry ANd Tracking (version 4)
GENIE	Generates Events for Neutrino Interaction Experiments
GNO	Gallium Neutrino Observatory
GPU	Graphics Processing Unit
IC-DC	IceCube DeepCore
ICARUS	Imaging Cosmic and Rare Underground Signals
IMB	Irvine-Michigan-Brookhaven
INFN	Istituto Nazionale di Fisica Nucleare
IO	Inverted Ordering
J-PARC	Japan Proton Accelerator Research Complex
K2K	KEK to Kamioka

KamLAND	Kamioka Liquid scintillator AntiNeutrino Detector
KARMEN	KArlsruhe Rutherford Medium Energy Neutrino
KEK	The High Energy Accelerator Research Organization
LAr TPC	Liquid Argon Time Projection Chamber
LAr	Liquid Argon
LBL	Long BaseLine
LBNF	Long-Baseline Neutrino Facility
LEP	Large Electron-Positron Collider
LHC	Large Hadron Collider
LNGS	Laboratori Nazionali del Gran Sasso
LSND	Liquid Scintillator Neutrino Detector
LXe	Liquid Xenon
MBL	Medium BaseLine
MC	Monte Carlo
MEC	Meson Exchange Current
MicroBooNE	Micro Booster Neutrino Experiment
MiniBooNE	Mini Booster Neutrino Experiment
MINOS	Main Injector Neutrino Oscillation Search
MIP	Minimum Ionising Particle
MSW	Mikheyev-Smirnov-Wolfenstein (Effect)
NC	Neutral Current
NO	Normal Ordering
NOvA	NuMI Off-Axis Electron Neutrino Appearance
NuMI	Neutrinos at Main Injector
NuWro	Wroclaw Neutrino Event Generator
OPERA	Oscillation Project with Emulsion-tRacking Apparatus

PEN	PolyEthylene Naphthalate
Phe	Photolectron
PMNS	Pontecorvo–Maki–Nakagawa–Sakata (Matrix)
PMT	PhotoMultiplier Tube
POT	Protons On Target
QE	Quantum Efficiency
RENO	Reactor Experiment for Neutrino Oscillation
RES	Resonant (Scattering)
RF	Radio Frequency
RHC	Reverse Horn Current
SAGE	Soviet–American Gallium Experiment
SBND	Short Baseline Neutrino Detector
SBN	Short Baseline Neutrino
SER	Single Photoelectron Response
SGD	Stochastic Gradient Descent
SiPM	Silicon PhotoMultiplier
SM	Standard Model (of Particle Physics)
SNO	Sudbury Neutrino Observatory
SPR	Single Photoelectron Response
SSM	Solar Standard Model
STEREO	Search for STErile REactor neutrino Oscillations
SURF	Sanford Underground Research Facility
T2K	Tokai to Kamioka
TPB	TetraPhenyl Butadiene
TTS	Transit Time Spread
TT	Transit Time
VUV	Vacuum Ultra Violet
WA104	CERN West Area experiment no 104

Acknowledgements

The work presented in this thesis and the thesis itself would not have been possible without the help and support of many people. First of all, I would like to express my sincere and heartfelt gratitude and appreciation to Agnieszka Zalewska, who has offered me the opportunity to start this thesis and introduced me to the world of neutrino physics. Thank you for your remarkable dedication and patience during all these years, I have learned so much from working with you. I would also like to thank my CERN doctoral studentship supervisor, Francesco Pietropaolo thanks to whom I had the opportunity to work in one of the most inspiring research laboratories in the world. I sincerely appreciate how you have been continuously encouraging and guiding me. You have always been so friendly and supportive of all my efforts and struggles. Working under your supervision has been very enjoyable, and I have learned and grown a lot.

I have to dedicate a special paragraph to Stephen Dolan, who made me feel confident and who guided me during these last two years and always gave me precious advice in the moments I was lost and throughout the finalisation of the thesis. Thank you for being an outstanding scientist and for your invaluable support and countless physics discussions. Thanks to you, I learned not to be afraid of proposing my own ideas and that my opinion matters. I hope you will keep sharing your enthusiasm about physics with everyone!

A special thanks to one of my closest co-workers, Saúl Alonso Monsalve, who supported me and my ideas during these last two years and provided me with the most help in understanding the world of machine learning algorithms and neural networks. I will never be able to express how grateful I am for meeting you on my scientific path. Thank you for showing me that work can be so much fun!

I thank all the experts I have worked with and learned from during my hardware work at CERN. I particularly thank Gian Luca Raselli for sharing all your expertise in photodetection and triggering systems of ICARUS. I am grateful for all you have taught me.

I have had the pleasure of working with and knowing many people over the years, and one way or another, you have been really helpful as I worked towards this thesis. Many thanks to Gianluca Petrillo, Kazuhiro Terao, Milind Diwan, Angela Fava, Massimo Rosella, Alessandro Menegolli, Burak Bilki, Andrea Zani, Stefania Bordoni

and Umut Kose. I am really grateful for everything you have taught me.

Finally, I would like to thank all my family and friends for their continued support throughout this difficult period. In particular, thank you to my mum, my grandma, my boyfriend and anyone else that helped me stay sane during the writing process - there are far too many people to name, but I hope you know who you are.

Bibliography

[1] M. Babicz *et al.* (ICARUS/NP01), JINST **13** (10), P10030, arXiv:1807.08577 [physics.ins-det].

[2] B. Ali-Mohammadzadeh, M. Babicz, *et al.* (ICARUS), JINST **15** (10), T10007, arXiv:2006.05261 [physics.ins-det].

[3] M. Babicz *et al.*, Nucl. Instrum. Meth. A **912**, 231 (2018).

[4] M. Babicz *et al.*, Nucl. Instrum. Meth. A **936**, 554 (2019).

[5] M. Babicz *et al.* (ICARUS Trigger Working Group), A technical status report on the ICARUS-T600 trigger system (2019).

[6] M. Babicz *et al.* (ICARUS Trigger Working Group), An updated status report on the ICARUS-T600 trigger system (2020).

[7] M. Babicz *et al.*, Nucl. Instrum. Meth. A **936**, 358 (2019).

[8] M. Babicz *et al.*, Nucl. Instrum. Meth. A **958**, 162421 (2020).

[9] B. Ali-Mohammadzadeh, M. Babicz, *et al.*, JINST **15** (06), C06042, arXiv:2004.09231 [physics.ins-det].

[10] M. Babicz *et al.*, JINST **15** (09), P09009.

[11] M. Babicz, S. Alonso-Monsalve, and S. Dolan, PoS **ICRC2021**, 1075 (2021).

[12] W. Pauli, Letter addressed to "Liebe Radioaktive Damen und Herren", Zürich, 4 Dez. 1930, Pauli Archive at CERN .

[13] P. Hernandez, "Neutrino Physics", 8th CERN–Latin-American School of High-Energy Physics (2016), 85–142 pp., arXiv:1708.01046 [hep-ph].

[14] E. Fermi, Zeitschrift für Physik **88**, 161 (1934).

[15] C. L. Cowan, F. Reines, *et al.*, Science **124**, 103 (1956).

[16] J. C. Evans, R. Davis, and J. N. Bahcall, Nature **251**, 486 (1974).

[17] P. A. Zyla *et al.* (Particle Data Group), Prog. Theor. Exp. Phys. **2020**, 083C01 (2020).

[18] S. Schael *et al.* (ALEPH, DELPHI, L3, OPAL, SLD, LEP Electroweak Working Group, SLD Electroweak Group, SLD Heavy Flavour Group), Phys. Rept. **427**, 257 (2006), arXiv:hep-ex/0509008.

[19] University of Zurich, Standard model.

[20] G. Aad *et al.* (ATLAS), Phys. Lett. B **716**, 1 (2012).

[21] S. Chatrchyan *et al.* (CMS), Phys. Lett. B **716**, 30 (2012).

[22] Y. Fukuda *et al.* (Super-Kamiokande), Phys. Rev. Lett. **81**, 1562 (1998).

[23] Q. R. Ahmad *et al.* (SNO), Phys. Rev. Lett. **87**, 071301 (2001).

[24] Q. R. Ahmad *et al.* (SNO), Phys. Rev. Lett. **89**, 011301 (2002).

[25] D. Rein and L. M. Sehgal, Annals Phys. **133**, 79 (1981).

[26] J. A. Formaggio and G. P. Zeller, Rev. Mod. Phys. **84**, 1307 (2012).

[27] J. Nieves, I. Ruiz Simo, and M. J. Vicente Vacas, Phys. Lett. B **707**, 72 (2012), arXiv:1106.5374 [hep-ph].

[28] K. Nakamura *et al.* (Particle Data Group), J. Phys. G **37**, 075021 (2010).

[29] L. Alvarez-Ruso *et al.* (NuSTEC), Prog. Part. Nucl. Phys. **100**, 1 (2018), arXiv:1706.03621 [hep-ph].

[30] B. Pontecorvo, Sov. Phys. JETP **6**, 429 (1957).

[31] Z. Maki, M. Nakagawa, and S. Sakata, Progress of Theoretical Physics **28**, 870 (1962), https://academic.oup.com/ptp/article-pdf/28/5/870/5258750/28-5-870.pdf.

[32] A. D. Sakharov, Pisma Zh. Eksp. Teor. Fiz. **5**, 32 (1967).

[33] L. Wolfenstein, Phys. Rev. D **17**, 2369 (1978).

[34] S. P. Mikheyev and A. Y. Smirnov, Sov. J. Nucl. Phys. **42**, 913 (1985).

[35] A. Y. Smirnov, in *10th International Workshop on Neutrino Telescopes* (2003) arXiv:hep-ph/0305106.

[36] A. Cervera *et al.*, Nucl. Phys. B **579**, 17 (2000).

[37] M. Freund, P. Huber, and M. Lindner, Nucl. Phys. B **615**, 331 (2001).

[38] R. Davis, Jr., D. S. Harmer, and K. C. Hoffman, Phys. Rev. Lett. **20**, 1205 (1968).

[39] J. N. Bahcall, Phys. Rev. **135**, B137 (1964).

[40] M. Cribier (GALLEX), Nucl. Phys. B Proc. Suppl. **70**, 284 (1999).

[41] J. N. Abdurashitov *et al.* (SAGE), J. Exp. Theor. Phys. **95**, 181 (2002).

[42] K. S. Hirata *et al.* (Kamiokande-II), Phys. Rev. Lett. **63**, 16 (1989).

[43] J. N. Bahcall, M. H. Pinsonneault, and S. Basu, Astrophys. J. **555**, 990 (2001), arXiv:astro-ph/0010346.

[44] K. Eguchi *et al.* (KamLAND), Phys. Rev. Lett. **90**, 021802 (2003).

[45] A. Gando *et al.* (KamLAND), Phys. Rev. D **88**, 033001 (2013), arXiv:1303.4667 [hep-ex].

[46] D. Casper *et al.*, Phys. Rev. Lett. **66**, 2561 (1991).

[47] M. H. Ahn *et al.* (K2K), Phys. Rev. D **74**, 072003 (2006).

[48] F. An *et al.* (JUNO), J. Phys. G **43**, 030401 (2016), arXiv:1507.05613 [physics.ins-det].

[49] D. Adey *et al.* (Daya Bay), Phys. Rev. Lett. **121**, 241805 (2018), arXiv:1809.02261 [hep-ex].

[50] G. Bak *et al.* (RENO), Phys. Rev. Lett. **121**, 201801 (2018), arXiv:1806.00248 [hep-ex].

[51] H. de Kerret *et al.* (Double Chooz), Nature Phys. **16**, 558 (2020), arXiv:1901.09445 [hep-ex].

[52] X. Guo *et al.* (Daya Bay), A Precision measurement of the neutrino mixing angle θ_{13} using reactor antineutrinos at Daya-Bay (2007), arXiv:hep-ex/0701029.

[53] J. K. Ahn *et al.* (RENO), RENO: An Experiment for Neutrino Oscillation Parameter θ_{13} Using Reactor Neutrinos at Yonggwang (2010), arXiv:1003.1391 [hep-ex].

[54] F. Ardellier *et al.* (Double Chooz), Double Chooz: A Search for the neutrino mixing angle θ_{13}) (2006), arXiv:hep-ex/0606025.

[55] K. Abe *et al.* (Super-Kamiokande), Phys. Rev. D **97**, 072001 (2018).

[56] M. G. Aartsen *et al.* (IceCube), Phys. Rev. Lett. **120**, 071801 (2018).

[57] M. G. Aartsen *et al.* (IceCube), Phys. Rev. D **99**, 032007 (2019), arXiv:1901.05366 [hep-ex].

[58] K. Abe *et al.* (T2K), Phys. Rev. Lett. **112**, 181801 (2014).

[59] P. Adamson *et al.* (MINOS), Phys. Rev. Lett. **112**, 191801 (2014), arXiv:1403.0867 [hep-ex].

[60] M. A. Acero *et al.* (NOvA), Phys. Rev. Lett. **123**, 151803 (2019).

[61] M. A. Acero *et al.* (NOvA), An Improved Measurement of Neutrino Oscillation Parameters by the NOvA Experiment (2021), arXiv:2108.08219 [hep-ex].

[62] K. Abe *et al.* (T2K), Phys. Rev. Lett. **107**, 041801 (2011), arXiv:1106.2822 [hep-ex].

[63] K. Abe *et al.* (T2K), Phys. Rev. Lett. **112**, 061802 (2014), arXiv:1311.4750 [hep-ex].

[64] P. Adamson *et al.* (MINOS), Phys. Rev. Lett. **110**, 251801 (2013), arXiv:1304.6335 [hep-ex].

[65] K. Abe *et al.* (T2K), Phys. Rev. Lett. **121**, 171802 (2018), arXiv:1807.07891 [hep-ex].

[66] K. Abe *et al.* (T2K), Nature **580**, 339 (2020), [Erratum: Nature 583, E16 (2020)], arXiv:1910.03887 [hep-ex].

[67] K. Abe *et al.* (T2K), Phys. Rev. Lett. **124**, 161802 (2020), arXiv:1911.07283 [hep-ex].

[68] M. Jiang *et al.* (Super-Kamiokande), PTEP **2019**, 053F01 (2019), arXiv:1901.03230 [hep-ex].

[69] I. Esteban *et al.*, JHEP **09** (9), 178.

[70] J. H. Christenson, J. W. Cronin, V. L. Fitch, and R. Turlay, Phys. Rev. Lett. **13**, 138 (1964).

[71] K. J. Kelly, P. A. N. Machado, S. J. Parke, Y. F. Perez-Gonzalez, and R. Z. Funchal, Phys. Rev. D **103**, 013004 (2021), arXiv:2007.08526 [hep-ph].

[72] A. Aguilar *et al.* (LSND), Phys. Rev. D **64**, 112007 (2001).

[73] I. Stancu *et al.* (MiniBooNE) 10.2172/809967 (2001).

[74] B. Pontecorvo, Sov. Phys. JETP **26**, 984 (1967).

[75] K. N. Abazajian *et al.*, arXiv:1204.5379 [hep-ph] (2012).

[76] A. A. Aguilar-Arevalo *et al.* (MiniBooNE), Phys. Rev. Lett. **121**, 221801 (2018).

[77] P. Huber, Phys. Rev. C **85**, 029901 (2012).

[78] T. A. Müller *et al.*, Phys. Rev. C **83**, 054615 (2011).

[79] F. P. An *et al.* (Daya Bay), Phys. Rev. Lett. **118**, 251801 (2017).

[80] D. Adey *et al.* (Daya Bay), Phys. Rev. Lett. **123**, 111801 (2019).

[81] G. Bak *et al.* (RENO), Phys. Rev. Lett. **122**, 232501 (2019).

[82] H. Almazán *et al.* (STEREO), Phys. Rev. Lett. **125**, 201801 (2020).

[83] T. A. Müller *et al.*, Phys. Rev. D **83**, 073006 (2011).

[84] V. Kopeikin, M. Skorokhvatov, and O. Titov, Reevaluating reactor antineutrino spectra with new measurements of the ratio between ^{235}U and ^{239}Pu β spectra (2021), arXiv:2103.01684 [nucl-ex].

[85] P. Anselmann *et al.*, Phys. Lett. B **314**, 445 (1993).

[86] J. Abdurashitov *et al.*, Astropart. Phys. **25**, 349 (2006).

[87] J. N. Bahcall, Phys. Rev. C **56**, 3391 (1997).

[88] M. A. Acero, C. Giunti, and M. Laveder, Phys. Rev. D **78**, 073009 (2008).

[89] C. Giunti and M. Laveder, Phys. Rev. C **83**, 065504 (2011).

[90] P. Adamson *et al.* (MINOS+), Phys. Rev. Lett. **122**, 091803 (2019), arXiv:1710.06488 [hep-ex].

[91] M. G. Aartsen *et al.* (IceCube), Phys. Rev. Lett. **117**, 071801 (2016), arXiv:1605.01990 [hep-ex].

[92] M. Dentler *et al.*, JHEP **2018** (8).

[93] T. Doke *et al.*, Nucl. Instrum. and Meth. A **269**, 291 (1988).

[94] G. Seidel *et al.*, Nuclear Instruments and Methods in Physics Research Section A: Accelerators, Spectrometers, Detectors and Associated Equipment **489**, 189 (2002).

[95] O. Cheshnovsky, B. Raz, and J. Jortner, J. Chem. Phys. **57**, 4628 (1972).

[96] T. Heindl *et al.*, EPL **91**, 62002 (2010), arXiv:1511.07718 [physics.ins-det].

[97] A. Hitachi *et al.*, Phys. Rev. B **27**, 5279 (1983).

[98] B. Baibussinov *et al.*, JINST **5** (03), P03005–P03005.

[99] C. Rubbia, The liquid-argon time projection chamber: a new concept for neutrino detectors (1977).

[100] S. Amerio *et al.* (ICARUS), Nucl. Instrum. Meth. A **527**, 329 (2004).

[101] R. Acciarri *et al.* (MicroBooNE), JINST **12** (02), P02017, arXiv:1612.05824 [physics.ins-det].

[102] M. Antonello *et al.*, Eur. Phys. J. C **73**, 1 (2013), arXiv:1209.0122 [hep-ex].

[103] N. Agafonova *et al.* (OPERA), Phys. Rev. Lett. **115**, 121802 (2015), arXiv:1507.01417 [hep-ex].

[104] T. Adam *et al.* (OPERA), JHEP **01**, 153, arXiv:1212.1276 [hep-ex].

[105] M. Antonello *et al.* (ICARUS), Phys. Lett. B **711**, 270 (2012), arXiv:1110.3763 [hep-ex].

[106] M. Antonello *et al.* (ICARUS), Phys. Lett. B **713**, 17 (2012), arXiv:1203.3433 [hep-ex].

[107] M. Antonello *et al.*, JHEP **2012** (11), 1, arXiv:1208.2629 [hep-ex].

[108] M. Antonello *et al.* (ICARUS), ICARUS at FNAL (2013), arXiv:1312.7252 [physics.ins-det].

[109] A. A. Aguilar-Arevalo *et al.* (MiniBooNE), Phys. Rev. D **79**, 072002 (2009).

[110] M. Antonello *et al.* (MicroBooNE, LAr1-ND, ICARUS-WA104), A Proposal for a Three Detector Short-Baseline Neutrino Oscillation Program in the Fermilab Booster Neutrino Beam (2015), arXiv:1503.01520 [physics.ins-det].

[111] P. A. Machado, O. Palamara, and D. W. Schmitz, Annu. Rev. Nucl. Sci. **69**, 363–387 (2019).

[112] C. Andreopoulos *et al.*, Nucl. Instrum. Meth. A **614**, 87 (2010), arXiv:0905.2517 [hep-ph].

[113] C. Andreopoulos *et al.*, The GENIE Neutrino Monte Carlo Generator: Physics and User Manual (2015), arXiv:1510.05494 [hep-ph].

[114] S. Agostinelli *et al.* (GEANT4), Nucl. Instrum. Meth. A **506**, 250 (2003).

[115] S. Gariazzo, C. Giunti, M. Laveder, and Y. F. Li, JHEP **2017** (6).

[116] L. Alvarez-Ruso *et al.* (NuSTEC), Prog. Part. Nucl. Phys. **100**, 1 (2018), arXiv:1706.03621 [hep-ph].

[117] U. Mosel, Ann. Rev. Nucl. Part. Sci. **66**, 171 (2016), arXiv:1602.00696 [nucl-th].

[118] I. Kourbanis, in *2nd North American Particle Accelerator Conference* (2017).

[119] P. Adamson, in *57th ICFA Advanced Beam Dynamics Workshop on High-Intensity and High-Brightness Hadron Beams* (2016).

[120] A. A. Aguilar-Arevalo *et al.* (MiniBooNE), Phys. Rev. D **81**, 092005 (2010).

[121] P. Adamson *et al.*, Nucl. Instrum. Meth. A **806**, 279 (2016).

[122] M. Acero *et al.* (NOvA), Phys. Rev. D **98**, 032012 (2018).

[123] R. Acciarri *et al.* (SBND), JINST **15** (06), P06033–P06033.

[124] A. A. Machado and E. Segreto, JINST **11** (02), C02004.

[125] A. Machado, E. Segreto, *et al.*, JINST **13** (04), C04026–C04026.

[126] G. Karagiorgi (MicroBooNE), Phys. Procedia **37**, 1319 (2012).

[127] R. Acciarri *et al.* (MicroBooNE), JINST **12** (08), P08003–P08003.

[128] C. Adams *et al.* (MicroBooNE), JINST **13** (07), P07006–P07006.

[129] C. Adams *et al.* (MicroBooNE), JINST **13** (07), P07007.

[130] R. Acciarri *et al.* (MicroBooNE), Eur. Phys. J. C **78**, 82 (2018).

[131] R. Acciarri *et al.* (MicroBooNE), JINST **12** (03), P03011–P03011.

[132] C. Adams *et al.* (MicroBooNE), Phys. Rev. D **99**, 092001 (2019).

[133] X. Qian, C. Zhang, B. Viren, and M. Diwan, JINST **13** (05), P05032–P05032.

[134] C. Adams *et al.* (MicroBooNE), JINST **15** (07), P07010.

[135] P. Abratenko *et al.* (MicroBooNE), JINST **15** (12), P12037.

[136] P. Abratenko *et al.* (MicroBooNE), High-performance Generic Neutrino Detection in a LArTPC near the Earth's Surface with the MicroBooNE Detector (2020), arXiv:2012.07928 [hep-ex].

[137] C. Adams *et al.* (MicroBooNE), JINST **14** (04), P04004–P04004.

[138] P. Abratenko *et al.* (MicroBooNE), Phys. Rev. Lett. **123**, 131801 (2019).

[139] P. Abratenko *et al.* (MicroBooNE), Measurement of the Flux-Averaged Inclusive Charged-Current Electron Neutrino and Antineutrino Cross Section on Argon using the NuMI Beam and the MicroBooNE Detector (2021), arXiv:2101.04228 [hep-ex].

[140] The MicroBooNE Collaboration, Single differential ν_μ charged-current cross section with the MicroBooNE detector using the Cosmic Ray Tagger (2020).

[141] T. Golan, J. T. Sobczyk, and J. Zmuda, Nucl. Phys. B Proc. Suppl. **229-232**, 499 (2012).

[142] P. Abratenko *et al.* (MicroBooNE), Search for an anomalous excess of charged-current quasi-elastic ν_e interactions with the MicroBooNE experiment using Deep-Learning-based reconstruction (2021), arXiv:2110.14080.

[143] P. Abratenko *et al.* (MicroBooNE), Search for an Excess of Electron Neutrino Interactions in MicroBooNE Using Multiple Final State Topologies (2021), arXiv:2110.14054.

[144] M. Antonello *et al.* (ICARUS), JINST **12** (04), P04010, arXiv:1612.07715 [physics.ins-det].

[145] L. Bagby *et al.* (ICARUS), JINST **16** (01), P01037, arXiv:2010.02042 [physics.ins-det].

[146] A. Falcone, *Studies and tests for the new light collection system of the ICARUS T600 detector*, Ph.D. thesis, Padua U. (2015).

[147] A. Falcone *et al.*, Nucl. Instrum. Meth. A **787**, 55 (2015).

[148] M. Babicz, *The light collection system of ICARUS T600 detector for the Short Baseline Neutrino (SBN) experiment at Fermilab*, Master's thesis, AGH-UST, Cracow (2017).

[149] Hamamatsu, *Photomultiplier Tubes and Photonics; Basics and applications; 3rd edition* (Hamamatsu Photonics K.K: Iwata City, Japan, 2007).

[150] M. Bonesini *et al.*, Journal of Vacuum Science & Technology B, Nanotechnology and Microelectronics: Materials, Processing, Measurement, and Phenomena **36**, 01A101 (2018).

[151] Hamamatsu, R5912-mod data sheet (2011).

[152] A. Scarpelli (ICARUS Trigger Working Group), Description of selected runs for detector studies, calibration, and tuning of the reconstruction (2021).

[153] J. Serrano *et al.*, *The White Rabbit Project*, Tech. Rep. (CERN, Geneva, 2009).

[154] C. Green *et al.*, J. Phys. Conf. Ser. **396**, 022020 (2012).

[155] P. Benetti *et al.*, Nucl. Instrum. Meth. A **574**, 83 (2007).

[156] W. R. Inc., Mathematica, Version 12.3.1, champaign, IL, 2021.

[157] G. F. Knoll, *Radiation Detection and Measurement, 3rd ed.*, 3rd ed. (John Wiley and Sons, New York, 2000).

[158] A. Bideau-Mehu *et al.*, Journal of Quantitative Spectroscopy and Radiative Transfer **25**, 395 (1981).

[159] M. Born and E. Wolf, *Principles of optics: electromagnetic theory of propagation, interference and diffraction of light* (Elsevier, 2013).

[160] A. C. Sinnock and B. L. Smith, Phys. Rev. **181**, 1297 (1969).

[161] L. LANDAU and E. LIFSHITZ, in *Electrodynamics of Continuous Media (Second Edition)*, Course of Theoretical Physics, Vol. 8, edited by L. LANDAU and E. LIFSHITZ (Pergamon, Amsterdam, 1984) second edition ed., pp. 394–412.

[162] S. Jain and V. Nanda, Journal of Physics C: Solid State Physics **4**, 3045 (1971).

[163] T. Cervi, M. Babicz, *et al.*, Nucl. Instrum. Meth. A **912**, 209 (2018).

[164] B. Abi *et al.*, The single-phase protodune technical design report (2017), arXiv:1706.07081 [physics.ins-det].

[165] C. Cuesta, Status of protodune dual phase (2019), arXiv:1910.10115 [physics.ins-det].

[166] M. Babicz *et al.*, Study of Light Production With A Fifty Liter Liquid Argon TPC (2021).

[167] F. Arneodo *et al.* (ICARUS-Milano), Phys. Rev. D **74**, 112001 (2006), arXiv:physics/0609205.

[168] C. Cuesta (DUNE), in *International Conference on Technology and Instrumentation in Particle Physics* (2021) arXiv:2106.15334 [physics.ins-det].

[169] R. Pordes and E. Snider, PoS **ICHEP2016**, 182 (2016).

[170] R. Brun and F. Rademakers, Nucl. Instrum. and Meth. A **389**, 81 (1997).

[171] M. G. Catanesi *et al.* (HARP), Eur. Phys. J. C **52**, 29 (2007), arXiv:hep-ex/0702024.

[172] I. Chemakin *et al.* (E910), Phys. Rev. C **77**, 015209 (2008), [Erratum: Phys.Rev.C 77, 049903 (2008)], arXiv:0707.2375 [nucl-ex].

[173] G. Cheng *et al.* (SciBooNE), Phys. Rev. D **84**, 012009 (2011), arXiv:1105.2871 [hep-ex].

[174] C. Mariani, G. Cheng, J. M. Conrad, and M. H. Shaevitz, Phys. Rev. D **84**, 114021 (2011), arXiv:1110.0417 [hep-ex].

[175] D. Beavis *et al.*, *Long Baseline Neutrino Oscillation Experiment at the AGS. Physics design report*, Tech. Rep. (BNL, Upton, NY (United States), 1995).

[176] K. T. McDonald, arXiv:hep-ex/0111033 (2001).

[177] C. Forti *et al.*, Phys. Rev. D **42**, 3668 (1990).

[178] C. Hagmann, D. Lange, and D. Wright, in *2007 IEEE Nuclear Science Symposium Conference Record*, Vol. 2 (IEEE, 2007) pp. 1143–1146.

[179] D. Heck, J. Knapp, J. N. Capdevielle, G. Schatz, and T. Thouw, CORSIKA: A Monte Carlo code to simulate extensive air showers (1998).

[180] M. Bonesini *et al.*, JINST **13** (12), P12020.

[181] A. Manegolli and G. Petrillo (ICARUS Trigger Working Group), ICARUS scintillation photon visibility mapping (2020).

[182] Y. LeCun *et al.*, Neural Computation **1**, 541 (1989).

[183] Y. LeCun *et al.*, Proceedings of the IEEE **86**, 2278 (1998).

[184] A. Aurisano *et al.*, JINST **11** (09), P09001, arXiv:1604.01444 [hep-ex].

[185] B. Abi *et al.* (DUNE), Phys. Rev. D **102**, 092003 (2020), arXiv:2006.15052 [physics.ins-det].

[186] C. Adams *et al.* (MicroBooNE), Phys. Rev. D **99**, 092001 (2019), arXiv:1808.07269 [hep-ex].

[187] S. Ben-David *et al.*, Machine learning **79**, 151 (2010).

[188] I. Redko *et al.*, *Advances in domain adaptation theory* (Elsevier, 2019) p. 187.

[189] Y. Ganin *et al.*, J. Mach. Learn. Res. **17**, 2096–2030 (2016).

[190] G. Perdue *et al.*, Journal of Instrumentation **13** (11), P11020.

[191] I. Goodfellow, Y. Bengio, and A. Courville, *Deep Learning* (MIT Press, 2016) `http://www.deeplearningbook.org`.

[192] deeplearning.ai, Deep Learning Specialization, `https://www.coursera.org/specializations/deep-learning` (2015).

[193] X. Glorot, A. Bordes, and Y. Bengio, in *Proceedings of the Fourteenth International Conference on Artificial Intelligence and Statistics*, Proceedings of Machine Learning Research, Vol. 15, edited by G. Gordon, D. Dunson, and M. Dudík (PMLR, Fort Lauderdale, FL, USA, 2011) pp. 315–323.

[194] X. Glorot and Y. Bengio, in *Proceedings of the Thirteenth International Conference on Artificial Intelligence and Statistics*, Proceedings of Machine Learning Research, Vol. 9, edited by Y. W. Teh and M. Titterington (PMLR, Chia Laguna Resort, Sardinia, Italy, 2010) pp. 249–256.

[195] L. Bottou, F. Curtis, and J. Nocedal, SIAM Review **60**, 223 (2018), https://doi.org/10.1137/16M1080173.

[196] A. Y. Ng, in *Proceedings of the Twenty-First International Conference on Machine Learning*, ICML '04 (Association for Computing Machinery, New York, NY, USA, 2004) p. 78.

[197] S. Ioffe and C. Szegedy, Batch normalization: Accelerating deep network training by reducing internal covariate shift (2015), arXiv:1502.03167 [cs.LG].

[198] N. Srivastava *et al.*, J. Mach. Learn. Res. **15**, 1929–1958 (2014).

[199] L. Prechelt, in *Neural Networks: Tricks of the Trade*, Lecture Notes in Computer Science, Vol. 1524, edited by G. B. Orr and K.-R. Müller (Springer, 1996) pp. 55–69.

[200] B. Graham and L. van der Maaten, Submanifold Sparse Convolutional Networks (2017), arXiv:1706.01307.

[201] M. Abadi *et al.*, in *OSDI*, Vol. 16 (2016) pp. 265–283, arXiv:1605.08695.

[202] C. Choy *et al.*, 4D Spatio-Temporal ConvNets: Minkowski Convolutional Neural Networks (2019), arXiv:1904.08755.

[203] K. He *et al.*, Deep Residual Learning for Image Recognition (2015), arXiv:1512.03385.